DISSERTATION

CLOUD-TOP ENTRAINMENT ANALYZED WITH

A LAGRANGIAN PARCEL TRACKING MODEL IN LARGE-EDDY SIMULATIONS

Submitted by

Takanobu Yamaguchi

Department of Atmospheric Science

In partial fulfillment of the requirements

For the Degree of Doctor of Philosophy

Colorado State University

Fort Collins, Colorado

Fall 2010

COLORADO STATE UNIVERSITY

July 27, 2010

WE HEREBY RECOMMEND THAT THE DISSERTATION PREPARED UNDER OUR SUPERVISION BY TAKANOBU YAMAGUCHI ENTITLED CLOUD-TOP ENTRAINMENT ANALYZED WITH A LAGRANGIAN PARCEL TRACKING MODEL IN LARGE-EDDY SIMULATIONS BE ACCEPTED AS FULFILLING IN PART REQUIREMENTS FOR THE DEGREE OF DOCTOR OF PHILOSOPHY.

<u>Committee on Graduate work</u>

_____

J. Ross Beveridge

_____

A. Scott Denning

_____

Steven K. Krueger

_____

Wayne H. Schubert

_____

Advisor: David A. Randall

_____

Department Head: Richard H. Johnson

ABSTRACT OF DISSERTATION

CLOUD-TOP ENTRAINMENT ANALYZED WITH

A LAGRANGIAN PARCEL TRACKING MODEL IN LARGE-EDDY SIMULATIONS

Despite decades of research, cloud-top entrainment has not been described with firm evidence. This leads to insufficient understanding of the physics of marine stratocumulus clouds. A Lagrangian Parcel Tracking Model (LPTM) was implemented in a large-eddy simulation model for detailed and direct analysis of the entrained air parcel following the parcel trajectory. The scalar advection scheme of the host model was replaced by a monotonic multidimensional odd-order conservative advection scheme. Tests with an idealized scalar field and stratocumulus turbulence suggested that the fifth-order scheme is optimal. Evaluation of the LPTM was performed with stratocumulus simulations. Parcel statistics agreed with Eulerian statistics, and the parcel paths agreed with the theoretical parcel paths. The Lagrangian budget equation for a scalar, however, generally does not hold for a simulated turbulence field, since the fractal nature of turbulence may cause numerical errors.

Two large-eddy simulations were performed with grid spacing of $O(5 \text{ m})$. The power spectra of these runs showed relatively good agreement with the energy cascade slope. A comparison with low-resolution simulations suggested that horizontal refinement is necessary for better representation of entrainment and microphysical processes.

The LPTM with the high-resolution stratocumulus simulation showed that the location of entrainment is in cloud holes, which are drier downdraft regions. Parcels in the inversion layer, subsiding from the free atmosphere, are entrained in to the mixed layer. They are cooled and moistened by radiation, evaporation, and mixing. A mixing fraction analysis shows that the coolings during entrainment due to radiation and evaporation are comparable. The largest contribution to buoyancy reduction is the cooling due to mixing, for our simulation. The analysis also shows that buoyancy reversal occurs for the entrained parcels.

Radiative cooling and cloud-top entrainment instability (CTEI) interact such that the radiative cooling forces larger saturation mixing fractions while CTEI forces smaller values. Additional simulations suggest that radiative cooling produces a negative feedback on the entrainment rate, which is strong enough to control turbulence and hide CTEI. Under such conditions, cloud breakup due to CTEI is unlikely.

Takanobu Yamaguchi
Department of Atmospheric Science
Colorado State University
Fort Collins, CO 80523
Fall 2010

ACKNOWLEDGMENTS

TABLE OF CONTENTS

LIST OF TABLES

LIST OF FIGURES

Chapter 1. Introduction

A pioneering work by Lilly (1968) on marine stratocumulus clouds (MSCs) pointed out the role of cloud-top radiative cooling as a turbulence generator. Negatively buoyant parcels because of radiative cooling result in planetary boundary layer (PBL) turbulence.

MSCs are capped by warm, dry air. MSCs are relatively cool and moist, and their turbulence forms a well homogenized layer above the surface, called the mixed layer. The change between MSC and the air above is sudden, which is frequently described as a "jump." The jump occurs in a thin interfacial boundary layer, often called the inversion layer, or sometimes referred as the entrainment interface layer, EIL.

The inversion layer is the site of cloud-top entrainment, which is a one-way process in which the warm, dry air aloft is captured by turbulence and brought into a PBL. Entrained air is laminar, warm and dry; thus, entrainment tends to suppress turbulence, and evaporate the cloud. For longer lived MSCs frequently observed along the west coast of continents, cloud-top radiative cooling should be balanced against the effect of the entrainment.

In his brief discussion, Lilly presented a hypothesis concerning the possible role of cloud-top evaporative cooling on entrained air. He envisioned cloud breakup as a result of runaway entrainment that can occur if the equivalent potential temperature decreases upward across the cloud top. He suggested that this cloud breakup due to evaporative

cooling would lead to a transition from MSCs to trade wind cumulus clouds. Lilly's hypothesis was further elaborated by Randall (1976, 1980) and Deardorff (1980), who discussed cloud-top entrainment instability (CTEI). A parcel being entrained could acquire negative buoyancy through evaporative cooling. This is now known as buoyancy reversal (Siems et al. 1990). CTEI requires not only buoyancy reversal but also enhancement of entrainment and production of turbulence kinetic energy (TKE). The negative buoyancy produced through buoyancy reversal could promote downward acceleration of a parcel, so that it is entrained faster. This faster entrainment could lead to the generation of TKE through an upward buoyancy flux. If the TKE production is sufficiently strong, then cloud breakup could be the end result of CTEI.

Cloud breakup due to CTEI has never been observed in the field (e.g., Albrecht et al. 1985; Kuo and Schubert 1988). Skepticism is also expressed in studies utilizing numerical simulations (e.g., Siems and Bretherton 1992). On the other hand, studies such as Moeng et al. (1995) and Yamaguchi and Randall (2008, hereafter YR08) argued that CTEI is hidden by the radiative effect. Their large-eddy simulations (LESs) show that CTEI generates weaker turbulence than radiative cooling does. Moeng (2000) did not observe a sudden increase in TKE expected with CTEI. These studies suggest that CTEI is not capable of modifying the field maintained by cloud-top radiative cooling, thus it is active but hidden. A recent LES study by Lock (2009) reached similar conclusions as found in these previous studies.

Judging whether CTEI happens for real MSCs is a very difficult task. Buoyancy reversal is a necessary condition for CTEI, but not a sufficient condition. Evidence for buoyancy reversal does not prove the existence of CTEI. However, detecting buoyancy

reversal for a real MSC is worth trying. Buoyancy reversal can be detected with the method of mixing fraction analysis (e.g., Albrecht et al. 1985; Kuo and Schubert 1988; Shao et al. 1997, hereafter SR97; vanZanten and Duynkerke 2002, hereafter VD02). Mixing fraction analysis partitions the cooling amount due to radiation, evaporation, and turbulent mixing during entrainment. Cloud-top entrainment events have to be used to determine whether buoyancy reversal happens in the course of entrainment.

The entrainment at the top of the MSCs has long been studied; however, direct study of the entrained parcels is rarely conducted. Finding the parcel being entrained is difficult for both the observational data and model data defined in the Eulerian grid. For example, SR97 relied on negative vertical velocity to identify the entrainment events for the LES output. Entrained parcels should have negative velocity, but there is no guarantee that the parcel with negative velocity is being entrained.

Our strategy is using the application of the Lagrangian Parcel Tracking Model (LPTM) to follow each parcel path, identify entrained parcels, and perform statistical analysis for the entrained parcels. LPTM predicts each parcel position using the spatially interpolated velocity from the LES velocity field. The entrained parcels are conditionally sampled based on their vertical position and other properties, which distinctly change from pre- to post- entrainment. This conditional sampling method does not involve subjective assumptions. Thus, a statistical analysis of the entrained parcels should be reliable. With the aid of LPTM, a typical entrained parcel's movement or history can be described in terms of location and physical parameters. The cooling effects of radiation and evaporation during entrainment can be estimated.

The numerical trajectory analysis has been used to investigate the dynamical and physical processes of the atmosphere. For instance, Krueger et al. (1995) used the Lagrangian parcel tracking method to identify convective updrafts and downdrafts in two dimensional boundary layer simulations. Lin and Arakawa (1997) applied the method to the deep convective cloud simulated with their cloud resolving model to identify where the entrained parcel originated. Weil et al. (2004, hereafter W04) developed a Lagrangian dispersion model that worked with LES output, to study particle dispersion of the convective boundary layer. Heus et al. (2008) adapted the W04's model, and showed that mixing between a shallow cumulus cloud and its environment happens mainly in a lateral direction.

We designed and developed our LPTM, and implemented it within our host LES model for online use, so that detailed output is not required. A parcel in a turbulent flow naturally takes a complicated path. It is not a good method to save three dimensional data with a very short time interval only for the accurate trajectory calculation, especially for high resolution simulations requiring large computer time.

Parcels of LPTM travel in the flow realized by its host model, and then scalars of the parcels are diagnosed. The scalar of the host model is also transported with the same flow with the Eulerian method. If the only active process is advection and LPTM perfectly predicts parcel position and diagnoses scalar perfectly, then the accuracy of LPTM is equal to the accuracy of the host model's scalar advection scheme. In the course of the LPTM development, our scalar advection scheme turned out to be unsatisfactory so that the results of LPTM contained large errors resulting from numerical diffusion. For

this reason, we sought a better scalar advection scheme. We also added a monotone property to the new advection scheme.

Simulating entrainment with LES seems to require small grid spacing, $O(1 \text{ m})$. Bretherton et al. (1999) state that entrainment is under-resolved with the 5 m vertical grid spacing. This should be applied to the horizontal grid spacing since the entrainment involves rolls of turbulent eddies. Gerber et al. (2005) used aircraft data to estimate that the mean width of the cloud holes, which is the potential location of entrainment, is 5 m. It is nearly impossible to perform a simulation with 1-m grid spacing at this time. We performed two simulations with a grid spacing $O(2.5\text{-}5 \text{ m})$: one is a simple idealized CTEI case based on YR08, and the other is a realistic nocturnal MSC simulation based on the GCSS (GEWEX Cloud System Study) LES intercomparison case of DYCOMS-II RF01 (Stevens et al. 2005, hereafter S05). This case maintains a steady cloud under CTEI conditions. DYCOMS-II was successfully simulated with a 6.25 m horizontal grid spacing and a 5 m vertical grid spacing for approximately 10 minutes after spin-up (S. Krueger 2007, personal communication). This high-resolution simulation was performed four years ago. At that time it was state-of-the-art.

LPTM was used with the high resolution DYCOMS-II simulation for analysis of cloud-top entrainment. In order to obtain as many entrainment events as possible, about 40 million parcels were placed around the inversion layer and tracked.

Drizzle/sedimentation is suggested to be an important process for MSCs (e.g., Savic-Jovcic and Stevens 2008; Hill et al. 2009). However, we exclude drizzle from our research to maintain the simplicity of our study, and to concentrate on radiative and evaporative cooling. The inclusion of the drizzle effect is being kept for future study.

In the next chapter, a new monotone scalar advection scheme is described and tested. In Chapter 3, a description of LPTM as well as evaluation of LPTM are discussed. The results of the high resolution LESs are presented in Chapter 4. Entrainment is studied with LPTM in Chapter 5. Interactions between radiative cooling and CTEI are hypothesized and tested in Chapter 6. The study closes with a summary and conclusions in Chapter 7.

A study of MSC and PBL tends to use many thermodynamic variables. Lists of the variables used in this study and their definitions are presented in Appendix A.

Chapter 2. Scalar Advection

2.1.   LES model

Our base LES model is SAM (System for Atmospheric Modeling; Khairoutdinov and Randall 2003). SAM has been widely used (e.g., YR08; Moeng et al. 2009; Caldwell and Bretherton 2009; Cheng and Xu 2009), and was part of the GCSS LES intercomparison studies (Moeng et al. 1996; Siebesma et al. 2003; S05; Ackerman et al. 2009).

SAM is a non-hydrostatic model based on the anelastic equations. It predicts the three velocity components, liquid water static energy, total non-precipitating water mixing ratio (vapor+cloud water+cloud ice), total precipitating water mixing ratio (rain +snow+grauple), and subgrid-scale (SGS) TKE. It uses finite differences on a staggered (Arakawa C) grid. It employs a three-phase bulk microphysics parameterization. SAM utilizes MPI with horizontal domain decomposition.

2.2.   Monotone ULTIMATE-MACHO scheme

The scalar advection scheme of SAM is based on MPDATA (Smolarkiewicz and Grabowski 1990) with $IORD = 2$. SAM-MPDATA is a second-order accurate monotone scheme. Our results suggest that the SAM-MPDATA scheme is not optimal for performing detailed studies with LPTM because of its numerical diffusion.

The ideal advection scheme is an odd-order, conservative, monotone and minimal numerical diffusion scheme for three-dimensional turbulent flow. Although there is no

scheme that satisfies these properties perfectly, the ULTIMATE scheme (Leonard 1991) appears to meet these criteria well enough. ULTIMATE is a one-dimensional scheme with arbitrary order of accuracy based on the Lagrange polynomial function. It can be monotone with the universal limiter developed by Leonard (1991). An example of fifth-order ULTIMATE is given in Figure 2.1. The summary and formulas of ULTIMATE are discussed in Appendix B. The multidimensional version of the third-order ULTIMATE is called UTOPIA (Leonard et al. 1993). Leonard et al. (1996) developed a multidimensional advection scheme with direct use of a one-dimensional scheme, such as the NIRVANA scheme (Leonard et al. 1995), which is a Courant-number-free version of ULTIMATE. Their MACHO scheme is attractive for its simple algorithm and conservation. MACHO is not strictly monotone with a one-dimensional universal limiter so that Leonard et al. (1996) called it "essentially monotonic." The ULTIMATE-MACHO scheme, however, sounds promising, if it can be made a monotone scheme for a three-dimensional deformational flow.
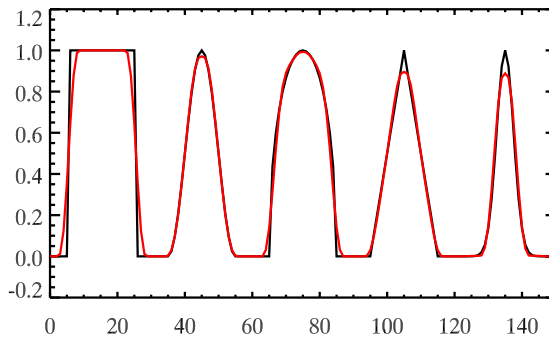
Figure 2.1   Advection test of the fifth-order ULTIMATE. The black line is the initial profile based on Leonard et al. (1995), which is a rectangular box, sine-squared, semi-ellipse, triangle, and Gaussian shapes from left to right. The red line shows the result after one rotation with a constant Courant number of 0.6, which requires 250 steps.

The MACHO scheme is outlined below;

$$1.\ \hat{\phi}_x = f^{1D}\left(\phi^n\right),$$
$$2.\ \phi_{AX} = \phi^n + c_x^{\text{box}}\left(\hat{\phi}_w - \hat{\phi}_e\right),$$
$$3.\ \hat{\phi}_y = f^{1D}\left(\phi_{AX}\right),$$
$$4.\ \phi_{AY} = \phi_{AX} + c_y^{\text{box}}\left(\hat{\phi}_n - \hat{\phi}_s\right),$$
$$5.\ \hat{\phi}_z = f^{1D}\left(\phi_{AY}\right),$$
$$6.\ \phi^{n+1} = \phi^n + c_w\hat{\phi}_w - c_e\hat{\phi}_e + c_n\hat{\phi}_n - c_s\hat{\phi}_s + c_t\hat{\phi}_t - c_b\hat{\phi}_b,$$

(2.1)

where ϕ^n is the grid volume mean scalar variable at time step n; $\hat{\phi}$ is the face value derived with a one-dimensional advection scheme represented as f^{1D}; ϕ_A represents a one-dimensional advective form update with the subscripted direction; c^{box} is the grid box Courant number; c is the Courant number for each face with the subscripted direction; the x, y, and z directions have west (w) and east (e), north (n) and south (s), and top (t) and bottom (b) face values, respectively. The grid box Courant number is set as

$$\begin{cases} c_x^{\text{box}} = c_w & \text{if } c_e > 0 \text{ and } c_w \geq 0 \\ c_x^{\text{box}} = c_e & \text{if } c_e \leq 0 \text{ and } c_w < 0 \\ c_x^{\text{box}} = 0 & \text{otherwise, if } c_w c_e < 0 \end{cases} .$$

(2.2)

The sequential one-dimensional advective form update of MACHO generates the necessary cross terms in terms of the multidimensional Taylor series expansion for stability analysis. The order of direction to compute face values is alternated in the next time step, for example, y, z then x. There are six combinations so that each possibility is selected once every six time steps. This equitable variation of the order of direction minimizes directional bias due to the sequential one-dimensional update.

For monotonicity preservation, we tested a one-dimensional universal limiter applied at steps 1, 3 and 5, a three-dimensional universal limiter developed by Thuburn (1996), and a three-dimensional FCT (flux-corrected transport; Zalesak 1979).

Our test consists of three cases: a rotating split cylinder, a sphere in turbulence, and a MSC of the GCSS DYCOMS-II (S05) case. The rotating split cylinder test is based on Zalesak (1979). For the sphere in turbulence test, the initially sphere-shaped tracer is advected with a background turbulent field developed with GCSS DYCOMS-II (S05).

As Leonard et al. (1996) showed, we obtained the essentially monotonic result with a one-dimensional universal limiter; monotonic for the rotating split cylinder and weakly non-monotonic for the sphere in turbulence.

The result with the three-dimensional universal limiter was unsatisfactory for the rotating split cylinder. It was monotone but exhibited significant numerical diffusion. Thuburn (1996) developed his limiter with UTOPIA, and he introduced two modifications to eliminate directional bias. Inclusion of the Thuburn's modifications did not decrease the numerical diffusion. Instead, the modifications created very weak but noticeable directional bias. Elimination of the directional bias of Thuburn's modification probably overlaps the MACHO's elimination of the directional bias, thus they end up creating a new error.

The application of three-dimensional FCT resulted in a monotone scheme. The numerical diffusion appears to be minimal. For this reason, we decided to use the three-dimensional FCT as a standard limiter for the ULTIMATE-MACHO scheme.

Details of each test and its result with the three-dimensional FCT are discussed below. The SAM-MPDATA, third-, fifth-, and seventh-order ULTIMATE-MACHO schemes were tested. We call them SM-2, UM-3, UM-5, and UM-7, respectively.

2.3. Rotating split cylinder

Our rotating split cylinder problem is based on Zalesak (1979). A cylinder with a slot is rotated with constant angular velocity, i.e., a solid body rotation. The computation was performed on a two-dimensional domain with 100^2 grid boxes. The cylinder was initially centered at (50.5, 50.5) of radius 15 grid sizes with a 5×25 grid-box slot. The scalar is located at the grid center and momentum is located at the grid wall for the C grid. The grid box inside the split cylinder was 2, and outside was 1. A velocity field was prescribed as

$$u = -\Omega(y - y_0), \quad v = \Omega(x - x_0), \quad \text{and } \Omega = \frac{2\pi}{628}, \tag{2.3}$$

where (x_0, y_0) is the axis of rotation (50.5, 50.5), and Ω is angular velocity, which completes one rotation in 628 steps.

The initial shape and the shape after one rotation for four advection schemes are presented in Figure 2.2. Only the 40^2 grid-box region near the cylinder is shown in the figure. Although all four schemes are monotone, SM-2 loses symmetry to the slot while UMs preserve it. A higher order scheme maintains sharp discontinuity better than a lower order scheme.
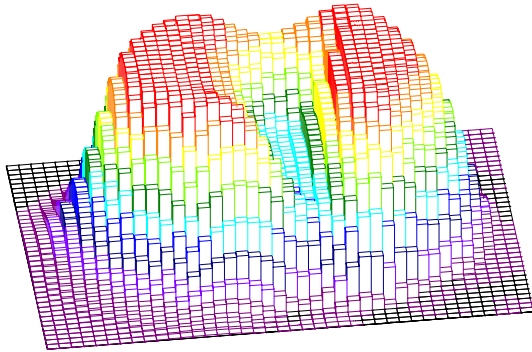
SAM-MPDATA (2nd)   3rd ULTIMATE-MACHO
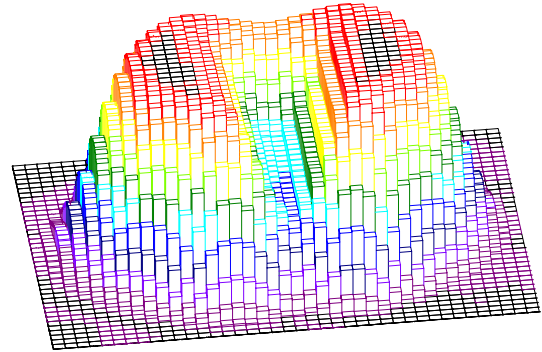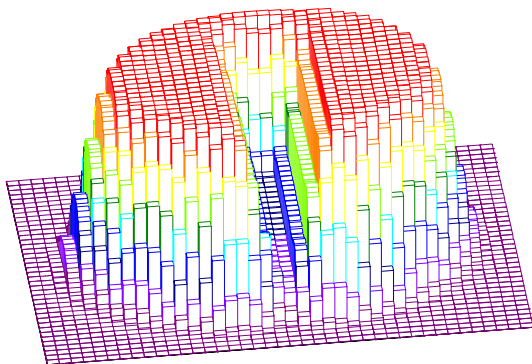
5th ULTIMATE-MACHO   7th ULTIMATE-MACHO

Initial condition

1.0 1.1 1.2 1.3 1.4 1.5 1.6 1.7 1.8 1.9 2.0
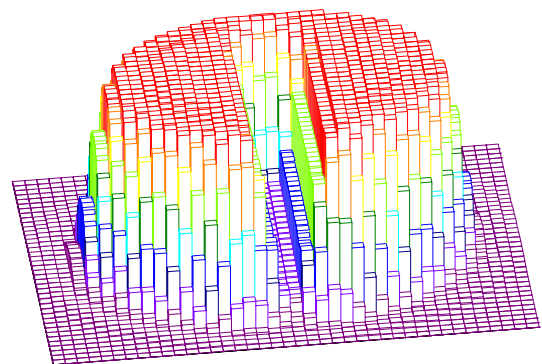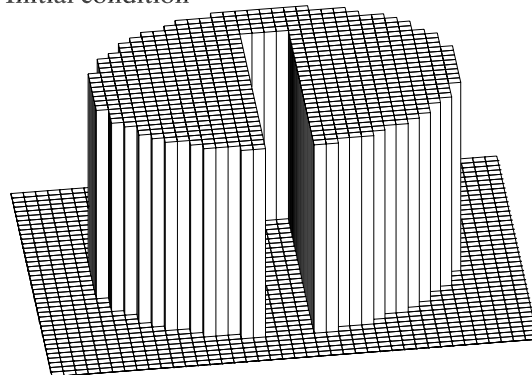
Figure 2.2   Result of the rotating split cylinder test after one rotation for four advection schemes, and the initial condition. Exact 1 and 2 values are colored black.

The time series of the total variance normalized with the initial value is shown in Figure 2.3. Switching SM-2 to UM-3 does not improve the result much. There is, however, a significant improvement between UM-3 and UM-5. The large diffusion for

earlier time steps for all schemes is due to deformation of the edge of the split cylinder. We define the numerical diffusion rate as a difference of normalized total variance over one time step. The mean numerical diffusion rate for the last 100 steps is 10.4×10^{-5} for SM-2, 8.9×10^{-5} for UM-3, 5.2×10^{-5} for UM-5, and 4.6×10^{-5} for UM-7. UM-5 is about two times less diffusive than SM-2, and UM-7 is about 2.3 times less diffusive than SM-2. The difference between UM-5 and UM-7 is small.
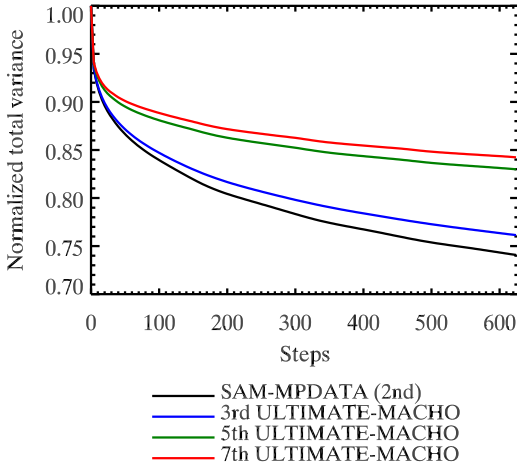
Figure 2.3   Time series of the total variance normalized with the initial total variance.

2.4.   Sphere in turbulence

As background turbulence, we first simulated GCSS DYCOMS-II (S05). SAM was configured by following S05, and ran for two hours, which is long enough to generate PBL turbulence. The horizontal domain width is 3.36 km and the domain depth is 1.6 km. The horizontal grid spacing is 35 m, and the vertical grid spacing is 5 m.

When SAM was restarted, a sphere-shaped tracer was introduced with a center at (1697.5 m, 1697.5 m, 747.5 m) and with a radius of 400 m. Grid values inside the sphere were set to 1, and outside were set to 0. The inversion layer existed at approximately the

850 m level, so that the approximate upper one-third of the sphere was in the free atmosphere, which was not turbulent. The only active process on the tracer was advection, and a new advection scheme was applied only to the tracer advection. That is, the PBL turbulence was the same for all four cases (SM-2, UM-3, UM-5, and UM-7). For this test, we ran an additional 600 time steps, which were equivalently five minutes in length.

The initial shape and the shape after 600 steps for four advection schemes are presented in Figure 2.4. Three isosurfaces of 0.1, 0.5, and 0.9 were drawn. The gap between isosurfaces is tighter for a higher order scheme.

SAM-MPDATA (2nd)
max = 1.0000E+00
min = -1.1262E-08
total variance = 0.721
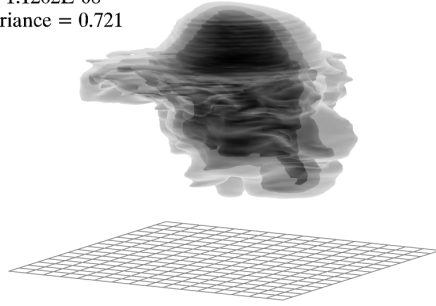
3rd ULTIMATE-MACHO
max = 1.0000E+00
min = -7.1427E-09
total variance = 0.756
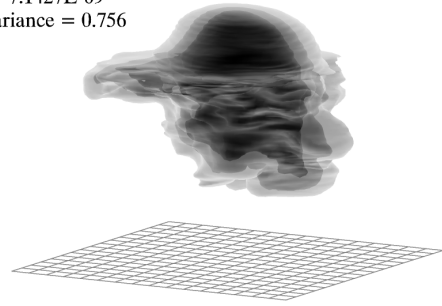
5th ULTIMATE-MACHO
max = 1.0000E+00
min = -1.6752E-09
total variance = 0.803
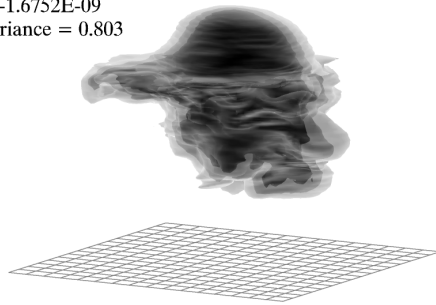
7th ULTIMATE-MACHO
max = 1.0000E+00
min = -9.8581E-10
total variance = 0.816
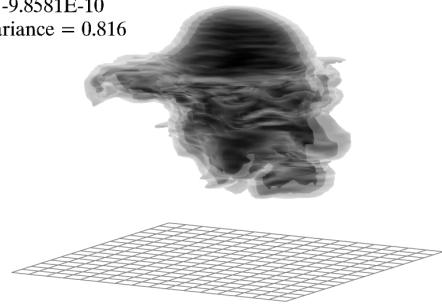
Initial condition
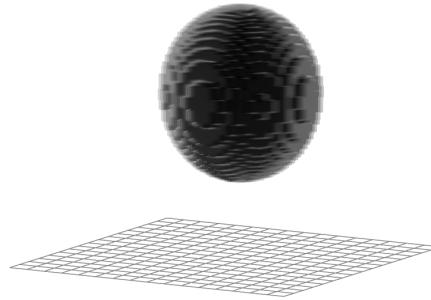
Figure 2.4   Distortion of a sphere in a turbulence test after 600 steps, with four advection schemes. The initial condition is also shown. The isosurface with the lightest gray represents 0.1, mid-dark gray 0.5, and darkest gray 0.9. Total variance is normalized with the initial value.

Based on the normalized total variance shown in Figure 2.5, the mean numerical diffusion rates for the last 100 steps are 2.9×10^{-4} for SM-2, 2.5×10^{-4} for UM-3, 2.2×10^{-4} for UM-5, and 2.1×10^{-4} for UM-7. SM-2 is approximately 1.4 times as diffusive as UM-5 and UM-7.
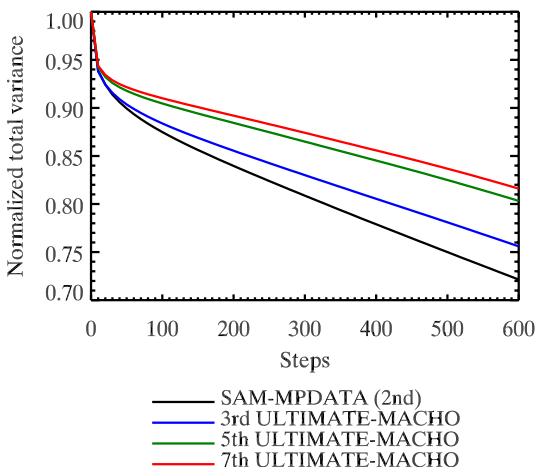
Figure 2.5   Same as Figure 2.3 but for the sphere in turbulence test.

2.5.   Marine stratocumulus boundary layer

GCSS DYCOMS-II was simulated with four different scalar advection schemes. Each simulation was performed for a four-hour duration. Horizontal mean profile data were output every minute without averaging over time.

The horizontal mean vertical profiles of the liquid water potential temperature, total water mixing ratio, cloud water mixing ratio, and cloud fraction are shown in Figure 2.6. These profiles were averaged for the last hour. There is a distinct difference between SM-2 and UMs. UMs maintain a well-mixed profile while SM-2 un-mixes it slightly. This results in the larger maximum cloud water and cloud amount for UMs. The difference between UM-5 and UM-7 is very small. Compared with the observations shown in Figures 3 and 4 of S05, UM-5 and UM-7 are closest: 289 K of liquid water potential temperature and 9 g kg^{-1} of total water mixing ratio in the mixed layer, more than 0.3 g kg^{-1} of maximum cloud water mixing ratio, and around 850 and 625 m for the cloud top and base heights.

16
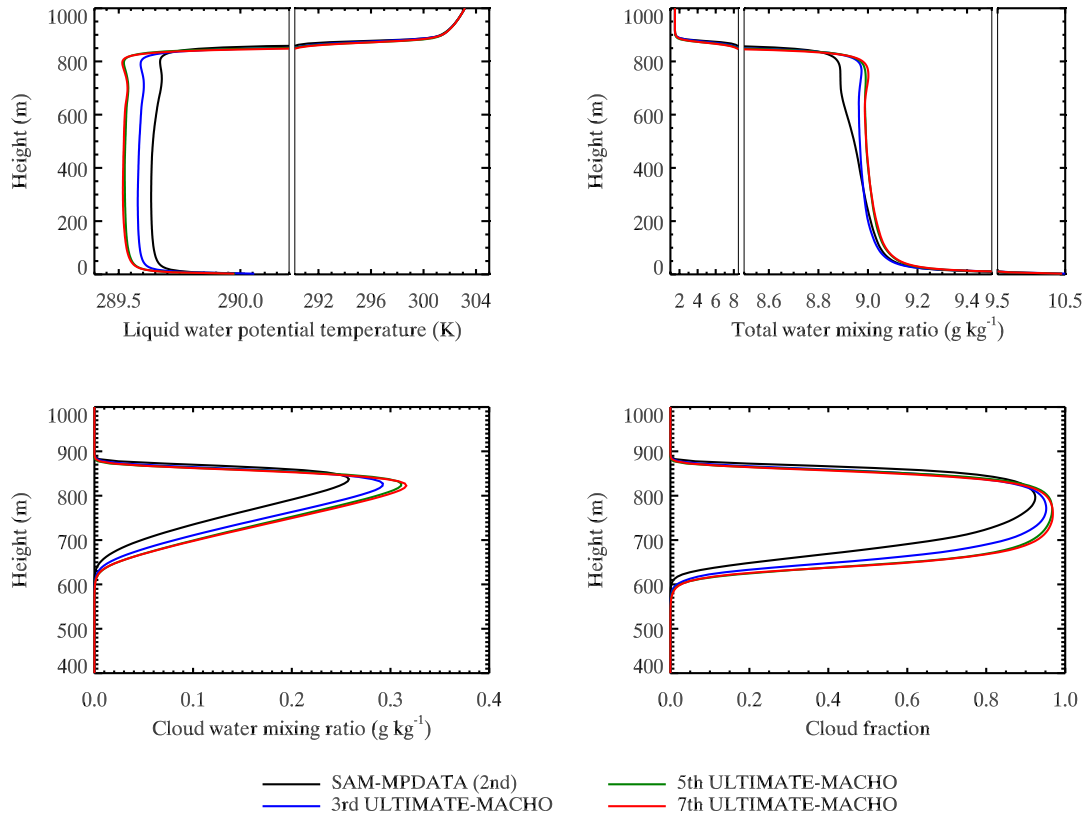
Figure 2.6   One-hour averaged horizontal mean vertical profile of liquid water potential temperature, total water mixing ratio, cloud water mixing ratio, and cloud fraction. The average was taken for the last hour.

The time series of the cloud water path, vertically integrated TKE, and diagnosed entrainment rate are presented in Figure 2.7a. The entrainment rate was diagnosed with the method described in Appendix C, which is an improved version of the method developed by YR08. The 30-minute running mean profiles were used as input to obtain a smooth time-series of the entrainment rate. The entrainment rate tends to be smaller for the higher order scheme. Entrainment brings laminar and dry air into PBL, thus more entrainment means less turbulence and cloud water in the mixed layer. Although the difference of entrainment rate among the advection schemes appears to be small, the influence is large; the TKE and cloud water path are considerably larger for the higher

order scheme. The vertical profiles of the buoyant production of TKE, variance and third moment of vertical velocity in Figure 2.7b also suggest a more energetic mixed layer for the higher-order scheme, due to weaker entrainment.
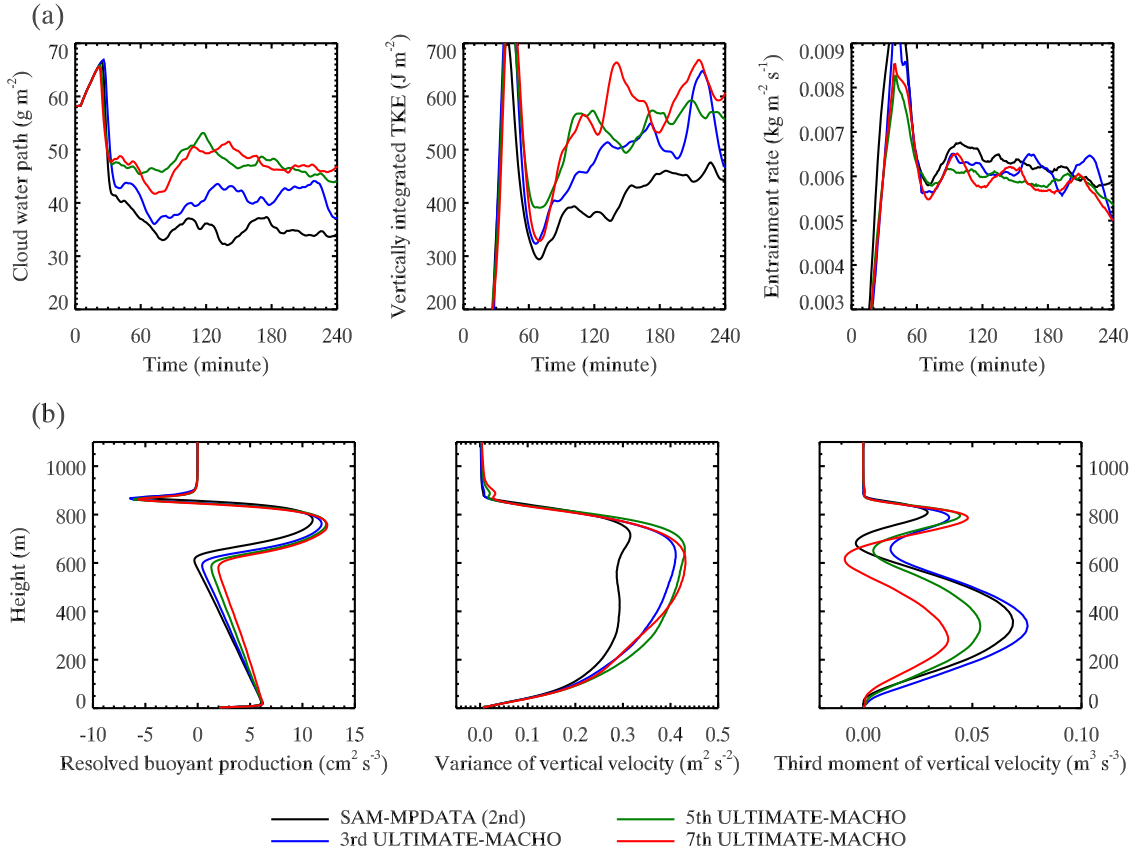
Figure 2.7   (a) Time series of the liquid water path, vertically integrated TKE, and entrainment rate. Entrainment rate was computed with 30-minute running mean profiles. (b) Hourly averaged vertical profiles of resolved scale buoyant production of TKE, the variance of the vertical velocity, and its third moment.

2.6.   Resolution and error from advection

Generally, as the resolution increases, the accuracy of advection also increases. This should be expected for ULTIMATE and ULTIMATE-MACHO. A steady state tracer test was designed and performed for one-dimensional advection.

For steady state, the tracer equation is simply written as

$$u \frac{\partial \phi}{\partial x} = S, \tag{2.4}$$

where S is the source term. We set the initial tracer shape as the four sine curves:

$$\phi = \sin\left(4\frac{2\pi}{X}x\right), \tag{2.5}$$

where X is the domain width and is 2048 m. From (2.4), the source term is given as

$$S = u\frac{8\pi}{X}\cos\left(\frac{8\pi}{X}x\right). \tag{2.6}$$

The initial tracer condition and source term are plotted in Figure 2.8. Five grid spacings, 32, 16, 8, 4, and 2 m, were tested with the constant Courant number of 0.25 with a constant velocity of 2 m s^{-1}. The fifth-order ULTIMATE was used for this test, since the MACHO procedure is not required for one-dimensional advection. All grid spacings were tested with and without FCT. Each case ran for five time steps.
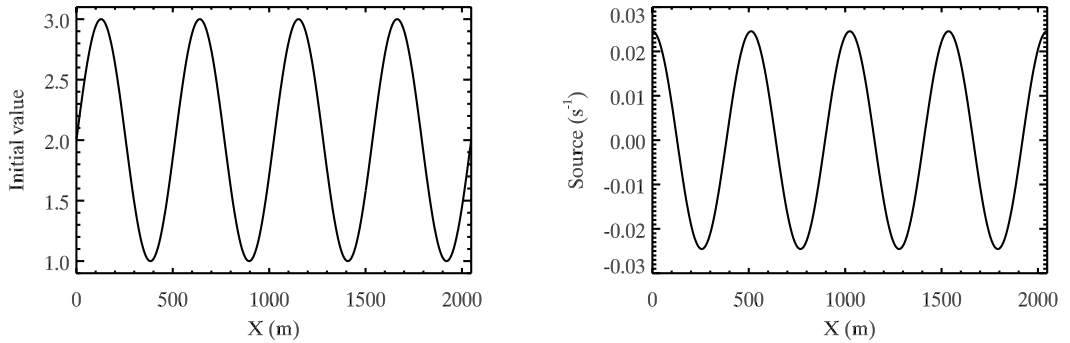
Figure 2.8   Initial tracer shape and source term.

The result for the 32 m grid spacing is presented in Figure 2.9. We define the advection error as the difference of the grid value from analytic value. The grid value

19

after five steps looks accurate (Figure 2.9a); it is, however, not accurate enough in terms of the advection error (Figure 2.9bc). The advection error per second around the extrema is approximately 0.0012, which is only one order of magnitude smaller than the source value. The advection error for the FCT run is distorted but the magnitude is the same order as the no-FCT run.
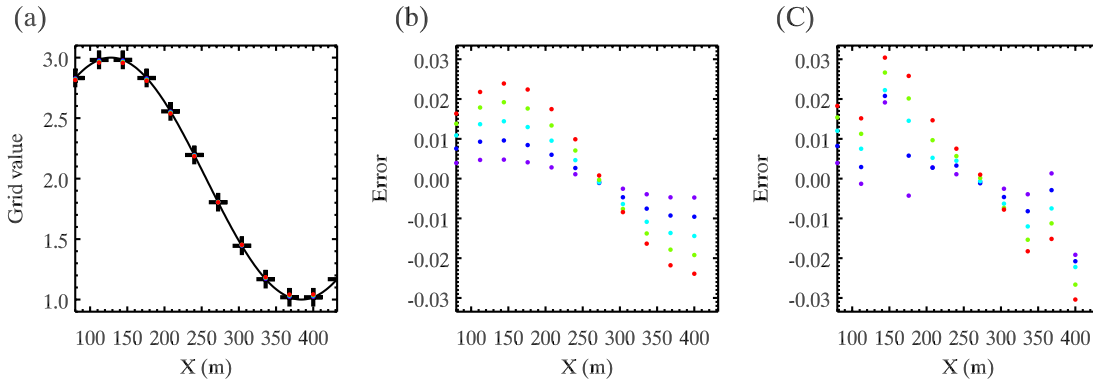
Figure 2.9   The result for the 32 m grid spacing. (a) Grid value of tracer for the initial (+ sign), each time step (purple to red dot) for no FCT run, and analytic solution (solid line) between 80 and 432 m. (b) Advection error for no FCT case. The advection error is defined as the analytical value minus the grid value. Purple is for the first step, and red is for the fifth steps. (c) Advection error for FCT case.

The results for the other grid spacings are presented in Figure 2.10a. As expected, the advection error is smaller for the smaller grid spacing. The FCT limiter forces the extreme value to be monotone, and it ends up causing a slightly larger error. In order to minimize an unwanted limiting procedure, we plan to implement the selective monotonicity preservation method of Blossey and Durran (2008) for future improvement. The domain-mean absolute advection error per second for the first step for all runs is presented in Figure 2.10b. The error decreases linearly as grid spacing becomes smaller in a log-log relationship.

20
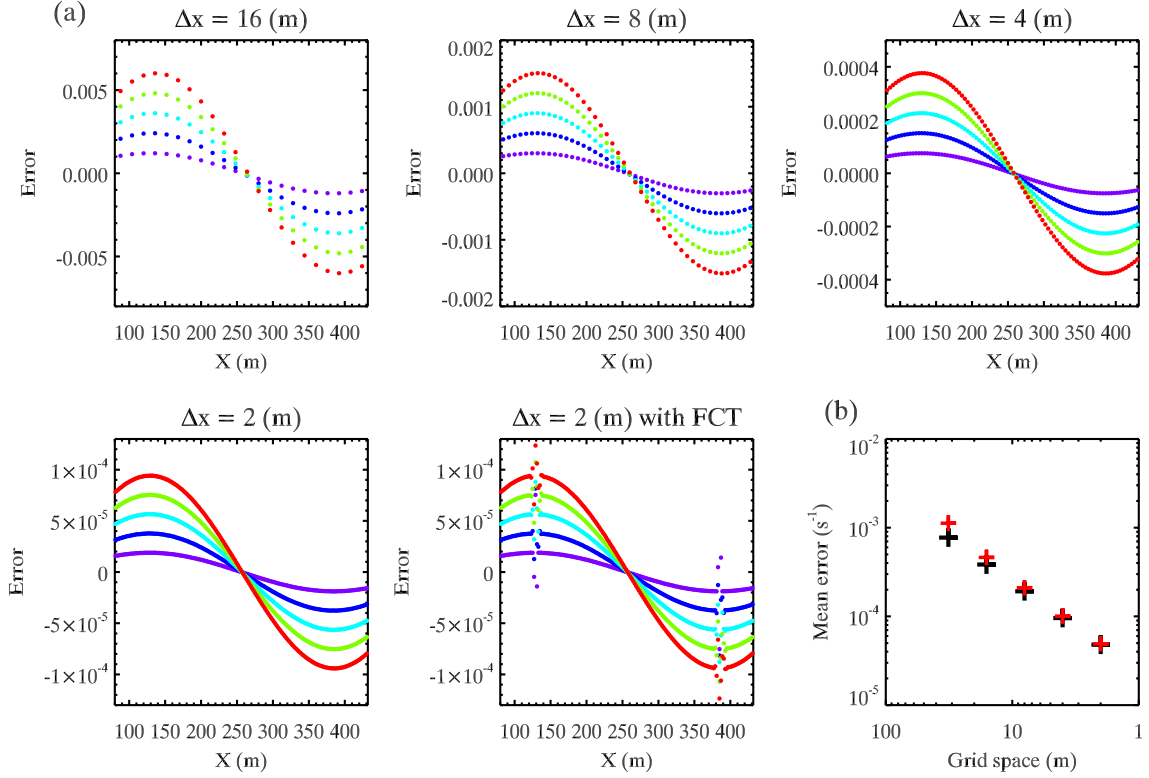
Figure 2.10   (a) Advection error for different grid spacings. (b) Domain-mean absolute advection error for the first step for different grid spacings. Black (red) + sign represents the run without (with) FCT.

2.7.   Numerical cost

ULTIMATE-MACHO is relatively more expensive than SAM-MPDATA, which is MPDATA with *IORD* = 2. Our timing test suggested that UM-3 is 1.8 times, UM-5 is 2.2 times, and UM-7 is 3 times as expensive as SM-2. About 42% of the total cost for the GCSS DYCOMS-II simulation was used by UM-5. The numerical cost of ULTIMATE-MACHO could be made smaller with a more optimized code.

The difference between UM-5 and UM-7 was shown to be small. Therefore, we recommend UM-5 as the optimal scheme among the scalar advection schemes tested.

Chapter 3.   Lagrangian Parcel Tracking Model

3.1.   LPTM description

A trajectory is predicted by integrating the ordinary differential equation of the Lagrangian position;

$$\frac{Dx_i}{Dt} = \left(u_r\right)_i + \left(u_s\right)_i, \tag{3.1}$$

where x is the Lagrangian position, u_r is the resolved scale velocity, u_s is the SGS velocity, and the subscript i represents the tensor notation. The resolved scale velocity is determined from the resolved scale velocity field of the host model. The SGS velocity has to be parameterized since the host model does not have it. W04 developed a parameterization of the SGS velocity based on the Lagrangian stochastic model of Thomson (1987).

The SGS velocity should be used to study "particle" dispersion, while each path should be seen as a "parcel" path without it. The particle represents a point, and the parcel represents air of size equivalent to the grid box (Figure 3.1). The particle trajectory requires the SGS velocity so that the mean velocity of many particles inside a grid box should be the same as a grid value. The parcel trajectory does not necessarily require the SGS velocity since a parcel path represents the path with the grid mean velocity. Scalars of a parcel can be diagnosed with the grid mean values, while additional SGS parameterization is, strictly speaking, required for a particle so that the particle average

22

inside a grid box is equivalent to the grid value. Parcel tracking and particle tracking converge at the small grid size, and the SGS component is no longer required.
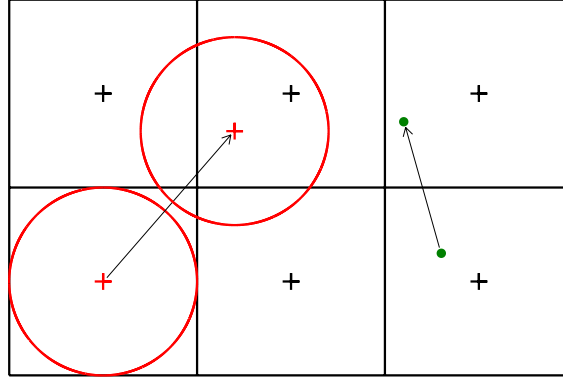
Figure 3.1   Parcel tracking (red circle) or particle tracking (green dot)?

LPTM estimates the resolved-scale parcel displacement by an iterative method based on the Heun scheme (i.e., the second-order Runge-Kutta scheme) with spatial interpolation. The scheme estimates the resolved scale velocity at half time step and at half way as

$$\begin{cases} \left(u_r\right)_i^{t+1/2,n} = \dfrac{1}{2}\left[\left(u_r\right)_i^t + \left(u_r\right)_i^{t+1^*,n}\right] & \text{for } n \geq 1 \\ \left(u_r\right)_i^{t+1/2,0} = \left(u_r\right)_i^t & \text{for } n = 0 \end{cases}, \tag{3.2}$$

where t is the time index, n is the index of iteration, and $\left(u_r\right)_i^{t+1^*,n}$ is the interpolated velocity at the position of

$$x_i^{t+1^*,n} = x_i^t + \left(u_r\right)_i^{t+1/2,n-1} \Delta t, \tag{3.3}$$

where Δt is a current time step. The parcel position is updated as

23

$$x_i^{t+1} = x_i^t + \left(u_r\right)_i^{t+1/2,n} \Delta t, \qquad (3.4)$$

where the second term in r.h.s. is the parcel displacement, which is represented by the integral path with the mean parcel velocity during one time step. If the number of iterations is zero, the scheme is reduced to the Euler scheme (i.e., the first-order forward scheme). The scheme becomes the Heun scheme if the number of iterations is one. The number of iterations can be more than two, which would result in better accuracy, since the parcel's resolved scale velocity is obtained with spatial interpolation. Our experiment suggests that more than four iterations improves the magnitude only slightly, $O(10^{-6}\text{-}10^{-8}$ m). We used three iterations throughout this study.

A fifth-order Lagrange polynomial interpolation is employed as a spatial interpolation method for any variables to be interpolated to a parcel for LPTM. For positivity for scalar variables, a trilinear interpolation (i.e., the second-order Lagrange interpolation) is used if the solution is negative. The details of spatial interpolation are discussed in Appendix D.

LPTM has the capability to simulate particle dispersion as an option. We adapted W04's SGS velocity parameterization. We modified one parameterized parameter, f_s, which represents the fraction of the ensemble-mean SGS turbulence kinetic energy (TKE) to the total ensemble-mean TKE. The role of the fraction is to indicate the relative importance of the SGS turbulence. The details of the modification and implementation are described in Appendix E.

A flowchart of LPTM is given below;

1. Host model: Collect necessary variables
2. LPTM
   1. Diagnose $\left(u_r\right)_i^{t+1/2}$ with the iterative Heun scheme (3.2)
   2. Predict $\left(u_s\right)_i^{t+1}$ with the W04's parameterization $\hspace{2cm}$ (3.5)
   3. Update position by $x_i^{t+1} = x_i^t + \left[\left(u_r\right)_i^{t+1/2} + \left(u_s\right)_i^{t+1}\right]\Delta t$
   4. Diagnose $\left(u_r\right)_i^{t+1}$ for next time step

LPTM is inserted at the end of the time step. During the host model stage, the necessary variables, which are not allocated in the host model, need to be collected in the LPTM grid arrays. Before exiting LPTM, the resolved scale velocity has to be updated. It is used as an initial guess velocity for the next time step. Because additional vertical layers are required for the spatial interpolation, LPTM has a user-specified lowest and highest altitude limit, where the parcel will be relocated to its initial height without changing its horizontal position.

For output, only the prognostic thermodynamic variables of SAM and pressure are spatially interpolated. Other thermodynamic variables such as temperature and cloud water mixing ratio are diagnosed with the spatially interpolated prognostic variables and pressure by the standard microphysics package of SAM described in Khairoutdinov and Randall (2003). Other variables such as SGS TKE and radiative heating rate are spatially interpolated to each parcel's position. Before writing the output file, a parallel merge-sort is used to sort parcels by their tags, i.e., the unique integer number for each parcel.

3.2.   Evaluation with GCSS DYCOMS-II

A three-dimensional SAM-LPTM run of GCSS DYCOMS-II was performed for evaluation. The duration was three hours. After two hours, LPTM placed parcels on all scalar definition points between the 1100 and 350 m level every 15 m distance for 50 layers. A total of 460,800 parcels was released. The SGS velocity was not applied. The output was saved every minute.

For the sufficient number of parcels, the Eulerian (SAM) and Lagrangian (LPTM) mean profiles should be the same. Figure 3.2 shows the Eulerian and Lagrangian mean profiles of the selected variables at the last time step. A 20-m vertical level bin was used to compute the Lagrangian mean. There is a general agreement between SAM and LPTM. The Lagrangian mean tends to be a little underestimated. A possible reason for this is that the number of parcels in each vertical bin is insufficient and/or the bin size is too large. Generally between 5000 and 9000 parcels are collected in each bin below PBL.
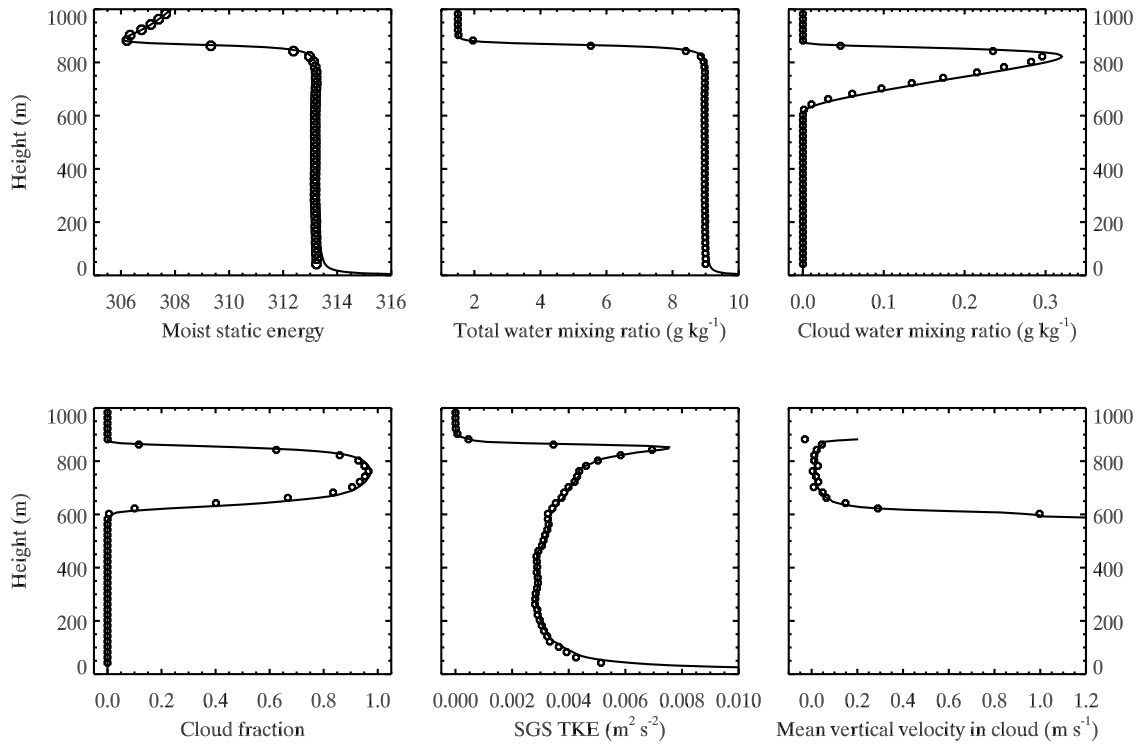
Figure 3.2   Eulerian and Lagrangian mean profiles. The solid line is the Eulerian mean, and the circle is the Lagrangian mean.

An arbitrarily chosen parcel's evolution is presented in Figure 3.3. The parcel is initially located above the inversion layer. The parcel experiences a large amount of cooling and moistening as it passes through the inversion layer. After the parcel penetrates through the jump, liquid condenses inside. Then the parcel moves further downward. The parcel paths shown in Figure 3.3b should be compared to those in Figures 14 and 15 of Schubert et al. (1979), which illustrate the theoretical parcel path of several scalars. The path of moist static energy is circular, with cooler air in the downdraft and warmer air in the updraft due to the entrainment, radiative cooling and surface process. A similar path should be expected for total water mixing ratio since it is also moist-conservative. The dry static energy follows two different paths depending on the surface heating. For the case of surface cooling, a figure-eight path is expected with

the upper part, which is in the cloud layer, is tilted. The figure eight becomes a simple loop for the case of surface warming, so that the path follows circular path with tilting in the cloud layer. The updraft is warmer and the downdraft is cooler in the cloud layer due to latent heat release from condensation, dry air mixing of entrainment and radiative cooling. The downdraft has a higher cloud base than the updraft. Below the cloud base, the downdraft is warmer than the updraft for the surface cooling case, and cooler for the surface warming case. Our parcel follows these theoretical paths quite well; the parcel paths of the moist static energy and total water mixing ratio are mostly circular. The path for the dry static energy is not a figure-eight shape because DYCOMS-II has surface warming. There is a cooling for the moist static energy and drying for the total water mixing ratio at around the 200 m level in the updraft. The parcel stays at the level for 6 minutes. The parcel probably encounters downdraft air just above it, and it mixes with the downdraft air. The parcel's dry static energy does not change, which means that the dry static energy of the downdraft air is as warm as the updraft air but drier. The parcel's total water mixing ratio decreases by approximately 0.07 g kg^{-1}, which is approximately 0.18 K cooling for moist static energy. This cooling agrees with the decrease in the parcel's moist static energy. Among the parcels tracked, some enter upward motion at higher levels, e.g., 400 m. These parcels should mix with updraft air coming from below and they obtain positive vertical velocity.
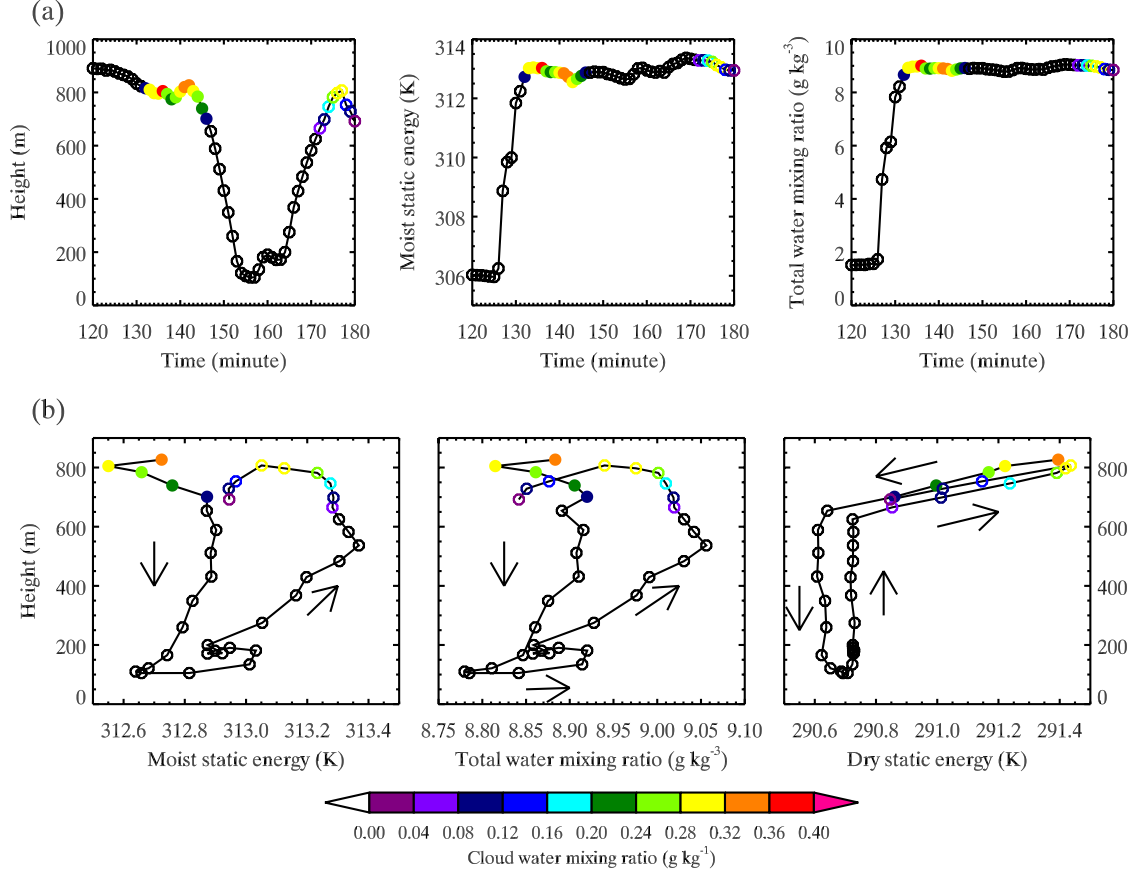
Figure 3.3   (a) Time evolution of height, moist static energy and total water mixing ratio for a parcel. (b) Vertical height evolution for moist static energy, total water mixing ratio and dry static energy. Parcel path is plotted after 142 minutes for clarity. Cloud water mixing ratio is colored, and filled and open circles are used. The arrows indicate the direction of the parcel's movement.

3.3.   Lagrangian budget and grid spacing

Our application of LPTM is to perform quantitative analysis of each Lagrangian parcel tendency term during entrainment. For example, the parcel's Lagrangian budget equation for the liquid water static energy for DYCOMS-II can be written as

$$\frac{Ds_l}{Dt} = \left(\frac{Ds_l}{Dt}\right)_{DIF} + \left(\frac{Ds_l}{Dt}\right)_{RAD} + \left(\frac{Ds_l}{Dt}\right)_{LSF}, \tag{3.6}$$

where the subscript DIF denotes SGS turbulent diffusion rate, RAD for longwave radiative heating rate, and LSF for large-scale forcing rate. In order to perform the budget

analysis, the Lagrangian budget equation for each parcel should be satisfied reasonably well.

For the steady state tracer advection test discussed in Section 2.6, LPTM balances the Lagrangian budget equation with a very small error, $O(10^{-8}$ s$^{-1})$, for all examined grid spacings.

Grid spacing should be appropriately set to gain the desired accuracy of the LPTM. The passive nature of LPTM to SAM appears here. The LPTM of the steady state tracer advection test with 32 m grid spacing is presented in Figure 3.4. Each parcel was initially located on each grid point (the purple dots in the figure). Each parcel arrives at the next grid point after four time steps (the red dots in the figure). Parcel error is defined as the difference between the parcel value and the analytical value. The parcel error tracks the advection error for both no-FCT and FCT cases. If the error threshold is set at 0.001 s^{-1}, then, from Figure 2.10, the grid spacing should be smaller than 4 m. Quite a high resolution is required, even in this simple case.
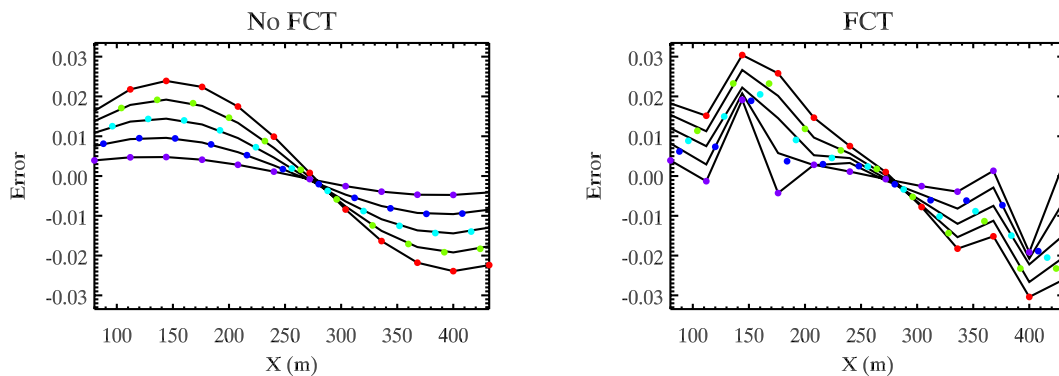
Figure 3.4   Parcel error (colored dot) and advection error (solid line) for the steady state tracer advection test for 64 m grid spacing without and with FCT.

A two-dimensional high resolution simulation of GCSS DYCOMS-II was performed to test the parcel budget for the liquid water static energy and total water mixing ratio. The horizontal grid spacing is 2 m and the vertical grid spacing is 1 m. The resolution is 2560×1600. Due to the small horizontal grid spacing, the geostrophic wind was assigned as a domain transport velocity to maximize the time step. Turbulence was generated for the first two hours. In terms of the last 30-minute time-mean horizontal-mean profiles of the first and second moments, the simulation converged, so that it agree well with a run with 5 m horizontal grid spacing and 2.5 m vertical grid spacing (not shown). At two hours, LPTM distributed parcels between 900 and 150 m, for every 2.5 m of vertical distance. A total of 768,000 parcels was released.

The two-dimensional histogram of the absolute parcel tendency error over one time step with respect to the parcel height is presented in Figure 3.5. The tendency error is defined as

$$\varepsilon_{s_l} \equiv \frac{Ds_l}{Dt} - \left[\left(\frac{Ds_l}{Dt} \right)_{\text{DIF}} + \left(\frac{Ds_l}{Dt} \right)_{\text{RAD}} + \left(\frac{Ds_l}{Dt} \right)_{\text{LSF}} \right], \tag{3.7}$$

where the tendency is computed as

$$\frac{Ds_l}{Dt} = \frac{s_l^{n+1} - s_l^n}{\Delta t}. \tag{3.8}$$

Generally, the error for both variables are $O(10^{-4}$ unit s$^{-1})$, which translates to $O(1$ unit hour$^{-1})$. The error of 1 unit hour^{-1} is large since, for instance, the peak value of the domain mean radiative cooling rate is around 4 K hour^{-1}. The parcel tendency error is large for the inversion layer, where the sharp gradient exists.
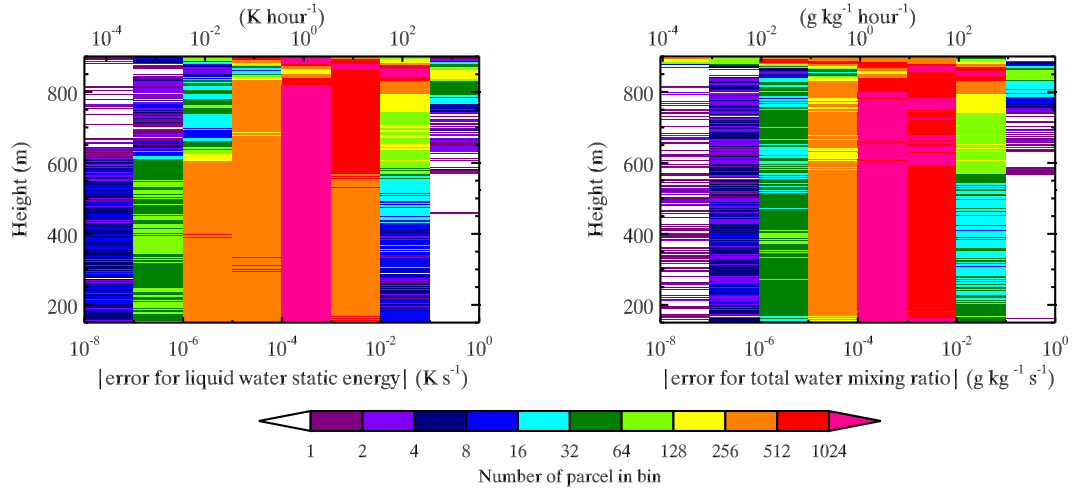
Figure 3.5   Two dimensional histogram of the parcel tendency error for liquid water static energy and total water mixing ratio. The absolute value of the error is binned in each log-scaled bin. The bin size of height is 2.5 m.

The possible reason for the large error is the fractal nature of turbulence, insufficient representation of the Lagrange interpolation for turbulence field, and numerical diffusion of the model. Complicated structure successively appears when scale is made one order smaller. It means that locally turbulent feature always exists for scale larger than molecular viscosity, which makes field smooth. Lagrange interpolation may not well represent the local turbulence field if it is noisy. SAM may contain non-negligible numerical diffusion.

Although this discrepancy of the Lagrangian budget equation prevents us from accurate quantitative analysis, we could still provide analysis qualitatively and quantitatively depending on the objectives.

3.4.   Numerical cost

The numerical cost of LPTM depends mainly on the number of parcels. The increased cost relative to the host model roughly depends on the resolution. With the same configuration of LPTM, the relative cost becomes smaller with higher resolution.

For example, the partition of the wall-clock time is 42% for the host model and 58% for LPTM for the three-dimensional GCSS DYCOMS-II simulation discussed in this chapter. If the grid size is made half for all directions, which makes time step half, the relative cost for LPTM shrinks to 15% for the same LPTM configuration.

Chapter 4.   High Resolution Simulations

4.1.   Buoyancy reversal simulation

YR08 performed a series of idealized LESs with different cloud-top conditions from stable to strongly unstable for CTEI. Their simulation setup was extremely simple; the only possible process to promote turbulence was CTEI through buoyancy reversal due to evaporative cooling at the cloud top. The cloud amount did not change for the stable cases, and cloud dissipation took place for the unstable cases. The cloud dissipated faster with more strongly unstable cloud-top conditions indicated by the Randall-Deardorff criterion. The overall turbulence production through CTEI was very weak compared with a realistic MSC simulation. With the additional simulations with radiative cooling, YR08 concluded that CTEI is active but hidden by radiative cooling, and it appears as cloud breakup only if CTEI overwhelms radiative cooling.

One of the drawbacks of YR08 is the use of 50 m horizontal grid spacing with saturation adjustment, or the so-called all-or-nothing scheme for evaporation and condensation. The all-or-nothing scheme treats the entire grid box as either completely dry or saturated based on the relative humidity. A 100% saturated grid box could immediately lose its cloud water for one time step, which is $O(0.1\text{-}1$ s$)$ for LES. Grabowski (2007) argues that the saturation adjustment is not adequate if the grid spacing is larger than 10 m.

One case of YR08, BR-0.5-73 (hereafter BR-73), was run with a 5 m isotropic grid. The all-or-nothing scheme with the 5 m isotropic grid is more physically correct than the scheme with the 50 m horizontal grid. The domain size is $3.2 \times 3.2 \times 1.25$ km. The duration was three hours, which was long enough for CTEI to evaporate most of the cloud water. The same simulation was also carried out with the 10 m horizontal grid. We call the 5 m isotropic grid run, 10 m horizontal grid run, and 50 m horizontal grid run BR-73-5m, BR-73-10m, and BR-73-50m, respectively.

For analysis, the evaporation and condensation rates were diagnosed on the model grid. The evaporation and condensation rates were not available for SAM since it predicts the total water mixing ratio and its microphysics parameterization partitions to water vapor and cloud condensate. The phase change cannot be seen from the total water mixing ratio. The equation for the total water and water vapor mixing ratio for the BR case is written as

$$
\begin{cases}
\dfrac{\partial r}{\partial t} + \mathbf{u} \cdot \nabla r = S_r \\[2mm]
\dfrac{\partial q}{\partial t} + \mathbf{u} \cdot \nabla q = S_q + \left(\dfrac{\partial q}{\partial t}\right)_{\text{EVP}} - \left(\dfrac{\partial q}{\partial t}\right)_{\text{CND}}
\end{cases}, \qquad (4.1)
$$

where S is the total source and sink except phase change, EVP represents evaporation, and CND represents condensation. The evaporation and condensation rates are the differences between the water vapor amount before and after microphysics parameterization divided by time step:

$$
\begin{cases}
\left(\dfrac{\partial q}{\partial t} \right)_{\text{EVP}} = \dfrac{q_{\text{MIC}} - q_{\text{PRG}}}{\Delta t} & \text{if } q_{\text{MIC}} - q_{\text{PRG}} > 0 \\[2em]
\left(\dfrac{\partial q}{\partial t} \right)_{\text{CND}} = -\dfrac{q_{\text{MIC}} - q_{\text{PRG}}}{\Delta t} & \text{if } q_{\text{MIC}} - q_{\text{PRG}} < 0
\end{cases}
\tag{4.2}
$$

where MIC represents "after microphysics," and PRG represents "before microphysics." q_{PRG} is a temporary array to contain water vapor, and is used to predict water vapor for one time step. q_{PRG} goes through advection, SGS diffusion, and other forcing processes like the total water mixing ratio. q_{PRG} is initialized with q_{MIC} after the evaporation and condensation rates are diagnosed with (4.2) for each grid.

The snapshot pictures of albedo and cross-sectional cloud water at 30, 60, 90 and 120 minutes are presented in Figure 4.1. The albedo was computed with a simple formula used in Savic-Jovcic and Stevens (2008) for their visualization. The cloud layer becomes thinner, and larger cloud holes appear as time passes. The small closed cell-like structure appears. A vertically circular pattern with downdrafts in dry air and updrafts in cloud air was observed by animating the plots.
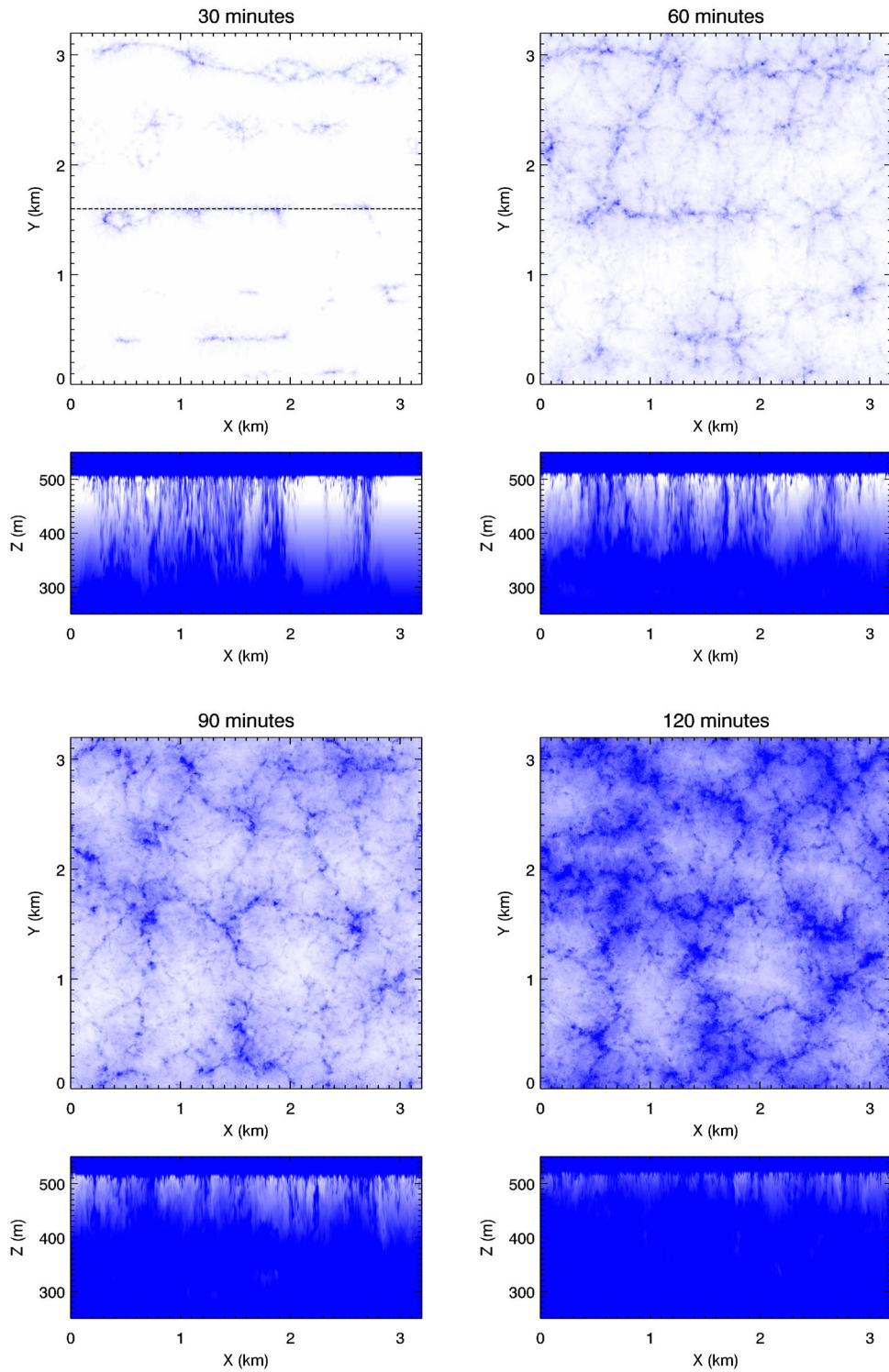
Figure 4.1   Snapshots of the albedo estimated with cloud water and a cross-sectional view of cloud water at the dashed line in the albedo plot for 30 minutes. Color scheme is scaled for visual clarity, so that white for albedo does not represent albedo of 1. Cloud water more than 0.4 g kg^{-1} is colored white.

The time evolution of the selected variables up to two hours of BR-73-10m is shown in Figure 4.2. BR-73-5m was performed before the evaporation and condensation rates were available as an output, so BR-73-10m is presented here. Comparison with BR-73-5m shows no significant difference. The moist static energy and total water mixing ratio become less mixed for the cloud layer due to entrainment-mixing from the initially mixed profile. The virtual dry static energy becomes cooler in the upper cloud layer during simulation. The net evaporation rate is always positive in the inversion layer so that the evaporation exceeds the condensation. When strong evaporation happens, strong condensation also occurs. The maximum negative buoyancy flux exists in the inversion layer and the maximum TKE is located at the same height. Three large evaporation events are observed in the evaporation rate before 90 minutes, and the maximum negative buoyancy flux appears 5 to 10 minutes after the maximum evaporation in those events. This is true for TKE for the second and third events.
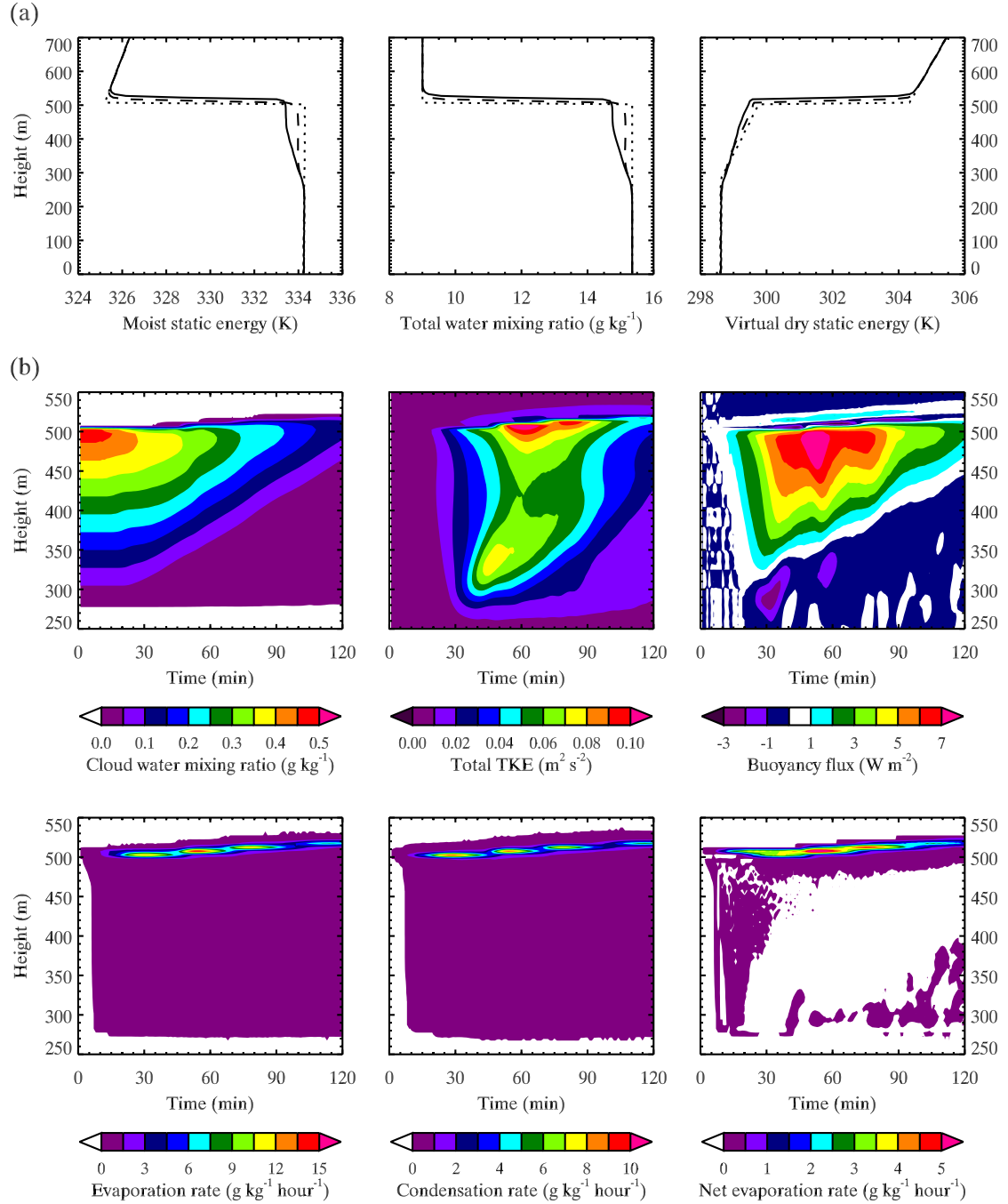
Figure 4.2   Time evolution of selected variables for BR-73-10m. For (a), the dotted line is at one minute, the dashed line is at one hour, and the solid line is at two hours.

The normalized liquid water path presented in Figure 4.3 shows that BR-73-5m and BR-73-10m dissipate their cloud water in almost the same way and faster than BR-73-50m. There is a very good agreement between BR-73-5m and BR-73-10m for the

entrainment rate and TKE. The disagreement in the entrainment rate after 100 minutes is

due to the depletion of the available cloud water for buoyancy reversal, which results in

very weak turbulence. For the same value of the normalized liquid water path for the first

90 minutes, the entrainment rate and TKE of BR-73-5m are generally larger than those of

BR-73-50m. The results suggest that CTEI is stronger for finer resolution, and

convergence is observed for BR-73-5m and BR-73-10m.
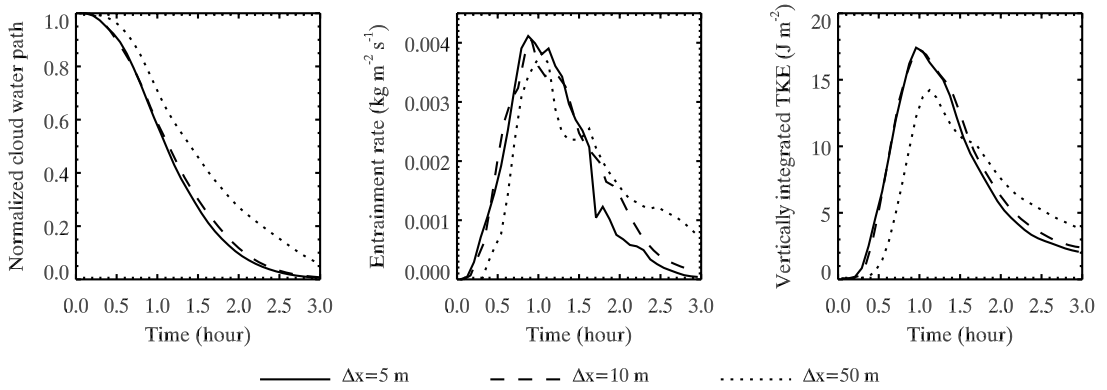
Figure 4.3   Time evolution of the normalized liquid water path, entrainment rate, and vertically integrated total TKE (i.e., resolved scale TKE plus SGS TKE) for the 5 (solid), 10 (dashed) and 50 (dotted) m horizontal grid size cases.

These simulations reproduce the theoretical mixing line as an evidence of CTEI

through buoyancy reversal. The mixing line is the line of the mixing fraction, χ, on the

one axis and buoyancy on the other axis (e.g., Albrecht et al. 1985; Kuo and Schubert

1988; SR97; VD02). The mixing fraction is defined for scalar ϕ as

$$\phi_{\mathrm{mix}} = \overline{\phi}_{B+}\chi + \overline{\phi}_{B}\left(1 - \chi\right), \tag{4.3}$$

where the subscript mix represents the resulting mixture of parcel's scalar of the scalars at

the level of the inversion layer top (level $B+$) and the level of the mixed layer top (level

40

B). The overbar denotes the horizontal mean. The resulting mixture of parcel consists of a fraction χ of air at the inversion layer top and the remaining fraction from the mixed layer top so that

$$
\begin{cases}
\phi_{\text{mix}} = \overline{\phi}_{B+} & \text{for } \chi = 1 \\
\phi_{\text{mix}} = \overline{\phi}_{B} & \text{for } \chi = 0
\end{cases}. \tag{4.4}
$$

If the scalar is moist conservative, one can compute the mixing fraction with (4.3).

The schematic diagram of the mixing line is presented in Figure 4.4. Theoretically, for the CTEI case, the mixing line has a kink at the maximum negative buoyancy where the mixing fraction becomes the saturation mixing fraction, χ^*. The saturation mixing fraction is a mixing fraction at exact saturation. For the mixing fraction larger than the saturation mixing fraction, the air is unsaturated after mixing and evaporation. The air in the orange area obtains negative buoyancy due to evaporative cooling. This negative buoyancy is evidence of buoyancy reversal, and it is also evidence of CTEI for the BR simulations since evaporative cooling is the only process for turbulence production. In other words, for the BR cases, buoyancy reversal is a necessary and sufficient condition for CTEI. Nevertheless, CTEI produces only weak turbulence.
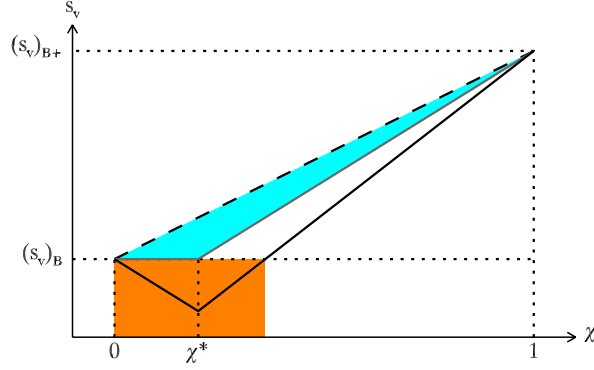
Figure 4.4 Schematic diagram of the mixing line. The dashed line represents the mixing only, the gray line is the mixing line for the CTEI boundary, and the black line is the mixing line for a CTEI case. The light blue area is stable for CTEI, and the orange area is unstable for CTEI.

SR97 showed that the saturation mixing fraction can be written as

$$\chi^* = \frac{\left[1 - (1 + \delta)\varepsilon\right]L\bar{l}_B}{\left[1 - (1 + \delta)\varepsilon\right]L\bar{l}_B + (\Delta s_v)_{crit}}, \tag{4.5}$$

where $\varepsilon = \dfrac{c_p\bar{T}}{L}$, and that the minimum possible value of the virtual dry static energy at

the saturation mixing fraction is written as

$$(s_v)_{min} = (\bar{s}_v)_B + \left[\Delta s_v - (\Delta s_v)_{crit}\right]\chi^*, \tag{4.6}$$

where $\Delta(\ ) = \overline{(\ )}_{B+} - \overline{(\ )}_B$ is the jump across the inversion layer. Randall (1976, 1980)

showed that

$$(\Delta s_v)_{crit} = \left[\frac{1 - (1 + \delta)\varepsilon}{1 + \gamma}\right]L\left[(\bar{q}^*)_{B+} - \bar{q}_{B+}\right], \tag{4.7}$$

42

where $\gamma = \dfrac{L}{c_p}\left(\dfrac{\partial \bar{q}^*}{\partial \bar{T}}\right)_p$. The parameter $\left(\Delta s_v\right)_{\text{crit}}$ is a measure of the dryness of the air

above the inversion and is always positive or zero. The terms in the bracket of the second

term on the r.h.s. of (4.6) form the Randall-Deardorff CTEI stability parameter;

$$\Delta_{\text{RD}} = \Delta s_v - \left(\Delta s_v\right)_{\text{crit}}, \tag{4.8}$$

and negative Δ_{RD} indicates CTEI.

For BR-73 simulations, total water mixing ratio, r, is a most suitable moist

conservative variable since the simulation configuration did not allow precipitation. The

mixing fraction is computed by

$$\chi = \dfrac{r_{\text{data}} - \bar{r}_B}{r_{B+} - \bar{r}_B}, \tag{4.9}$$

where the subscript data represents value at each grid box. The values at levels B and $B+$

were diagnosed with the method described in Appendix C.

Figure 4.5 shows the time series of the saturation mixing fraction and the level B

and $B+$ values for the total water and virtual dry static energy. The saturation mixing

fraction becomes small as cloud liquid water becomes small at the mixed layer top. The

production of buoyancy reversal should be slowed down with the small saturation mixing

fraction. After 90 minutes, the time evolutions shown in Figure 4.3 suggest the slower

CTEI. The inversion top values are steady, while the mixed layer top values decrease

about 1 g kg^{-1} for the total water mixing ratio and about 0.5 K for the virtual dry static

energy due to entrainment.
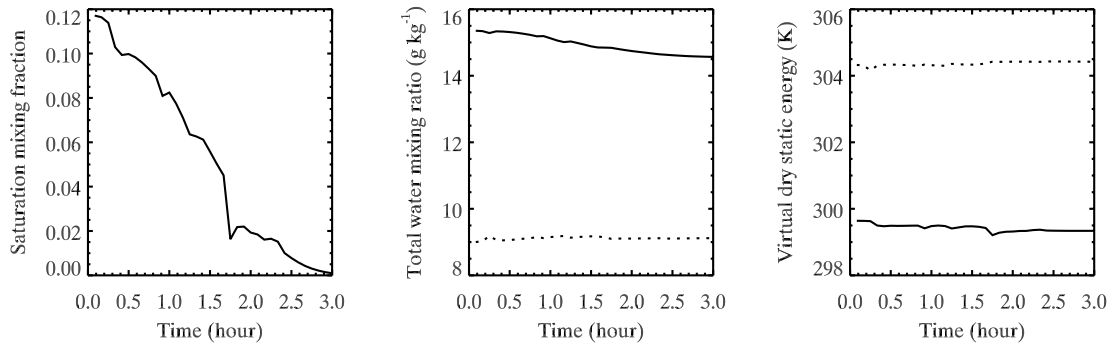
Figure 4.5   Time series of the saturation mixing fraction and the inversion top and mixed layer top total water, and virtual dry static energy. The solid line is level *B* and the dotted line is level *B+*.

The probability density function (PDF) of the mixing fraction, and the mixing line diagram with the joint PDF of the mixing fraction and virtual dry static energy for BR-73-5m at one hour are shown in Figure 4.6. The initial inversion layer height, i.e., 507.5 m, was used for the vertical level of r_{data}. The height was below the cloud top at one hour. The result at 10 seconds is also shown. The PDF moves toward the left with an increasing range of the mixing fraction as time passes. The joint PDF moves left and downward forming the straight mixing line as time passes. During the movement, the joint PDF becomes elongated, then the kink appears where the saturation mixing fraction is expected. No notable difference is found among the simulations.
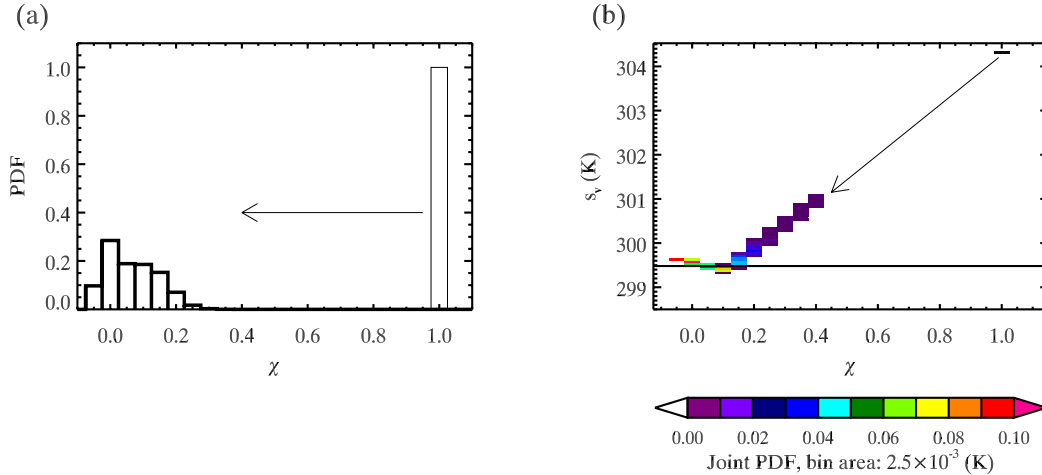
Figure 4.6   (a) PDF of the mixing fraction for BR-73-5m at one hour. The histogram with a thin line located on the right side is at 10 seconds. (b) Joint PDF of the mixing fraction and virtual dry static energy. The black joint PDF located at the upper right is at 10 seconds. The horizontal solid line is the diagnosed value at level *B*. Data at 507.5 m vertical level, which is the initial inversion top height, was used to create these PDFs.

Power spectra are useful to see if turbulence is well represented in both resolved and subgrid scales. Generally, the power spectrum is expected to decrease with increasing wavenumber as $\kappa^{-5/3}$ beyond the energy-containing range, i.e., inertial subrange. It is well-known that the power spectrum drops faster than $\kappa^{-5/3}$ for insufficient grid spacing. Bryan et al. (2003) found that the rapid drop occurs in a distance less than six grid points wide, and argued that this rapid drop is caused by the numerical diffusion of the model, so that the information at scales smaller than six grid sizes does not represent a physical solution for the model. Bryan et al. (2003) also found that the magnitude of the power spectra increases with increasing resolution.

The power spectra of the vertical velocity from 430 to 530 m vertical level for every 10 m are presented in Figure 4.7. Each power spectrum was computed with two-dimensional FFT over the horizontal plane, and then averaging along one-direction-wavenumber space. The power spectra below 490 m decline for the small wavelength,

and they are a little shallower than $\kappa^{-5/3}$ at 10 m wave length. The power spectra above 500 m do not show a decline. This indicates that either the inertial subrange is smaller than 10 m throughout layers, or there may be no turbulence most of the time, only waves like in a stable boundary layer. The turbulence in the inversion is not well represented in and above the inversion layer (above 500 m), however the vertical velocity is very small. On the other hand, turbulence in the mixed layer is fairly well represented.
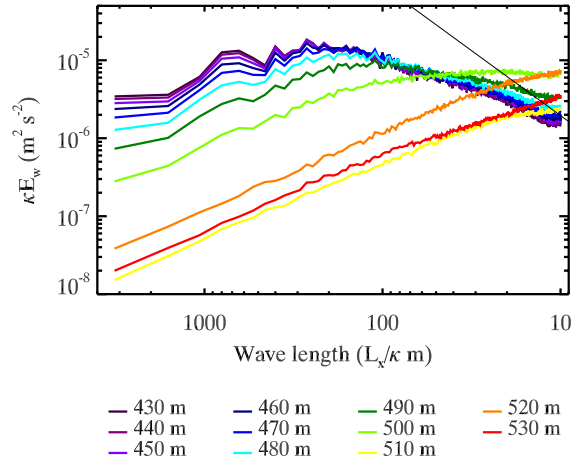
Figure 4.7   Power spectra of the vertical velocity E_w multiplied by wave number, $\kappa \equiv L_x / \lambda$ at one hour. L_x is the domain width, which is 3.2 km. λ is wavelength. The thin line represents a reference energy cascade line with $\kappa^{-5/3}$.

4.2.   DYCOMS-II RF01 simulation

We modified the model configuration of the GCSS DYCOMS-II (S05, hereafter GCSS) as follows. GCSS uses the prescribed surface flux and parameterized longwave radiation. Our FP (full physics) configuration computes the surface fluxes based on Monin-Obukhov similarity (Monin and Obukhov 1954), and the longwave radiative flux with the RRTM (Rapid Radiative Transfer Model, Mlawer et al. 1997) code. DYCOMS-II is a nocturnal MSC so that there is no solar radiation. The FP configuration also assigns

46

the geostrophic wind as a domain transport velocity in order to use a larger time step for a high resolution case. The duration is four hours. The summary of the simulation configurations is listed in Table 4.1. The vertical grid spacing is stretched above 1.6 km for the FP cases since RRTM requires the domain top around 30 km. We ran three FP cases: FP1 differs from GCSS by surface flux and radiation calculation, FP2 is the same for FP1 but uses finer vertical grid spacing, and FPH is a high resolution simulation with the 5 m horizontal grid spacing and 2.5 m vertical grid spacing.

Table 4.1   The list of the simulation setup for the GCSS and three FP cases.

	Δt (s)	Δx (m)	Δz (m)	domain width (km)	surface flux	longwave radiation	domain transport u and v (m s^{-1})
GCSS	0.5	35	5	3.35	prescribed	parameterized	0, 0
FP1	0.5	35	5	3.35	Monin and Obukhov	RRTM 10 s update	-7, -5.5
FP2	0.25		2.5		Monin and Obukhov	RRTM 5 s update	-7, -5.5
FPH	0.25	5	2.5	3.2	Monin and Obukhov	RRTM 1.25 s update	-7, -5.5

The GCSS longwave parameterization is based on the flux profiles derived from the advanced radiative transfer code. It is designed to mimic the observed longwave radiation flux profile as close as possible. Application of the parameterization enables us to compute radiative flux for each time step, which is expensive for the advanced radiation code. One of our goals is to study the radiative effect during entrainment, so that the accurate calculation of the longwave radiative flux is required. The GCSS longwave parameterization is not appropriate for our purpose since, for instance, it uses the arbitrary defined cloud-top height.

47

RRTM is expensive to call every time step. By calling once every specified number of time steps, however, the cost of RRTM becomes less. As pointed out by Xu and Randall (1995), infrequent update of the radiation produces bias in terms of the correlation of time series. We performed an experiment to figure out the optimal update period. First, FP1 was simulated with updating longwave radiation every time step, i.e., every 0.5 seconds, for two hours to setup turbulence. This turbulence field was used as a common initial condition for the test. The simulations with various update periods were continued for an additional hour. The output was saved every five seconds, thus 720 samples were collected for each run. We tested the update period of 0.5, 5, 10, 20, 30, 40, 50, 60, 90, and 120 seconds.

To perform correlation analysis, we focused on the inversion layer, where entrainment takes place. The inversion layer is defined with the lowest level z_B and highest level z_{B+} among all cases. The correlation was computed for the time series of the horizontal mean inversion-layer profile.

The correlation to the 0.5 second update period for selected variables is plotted in Figure 4.8. All of the correlations are high, which means that the change in radiative effect for different update periods is small for a one-hour simulation for the horizontal mean inversion-layer profile. The correlations generally decrease for an update period smaller than 40 seconds, and the trend is distorted for several variables after 40 seconds, which means that an update period shorter than 30 seconds is safer. The numerical cost of RRTM with the update period of 10 seconds (i.e., 20 time steps) is about 1.1 times the numerical cost of the GCSS parameterization called every time step. The timing test

suggested that about 10% of the total cost was used by RRTM with a 10-second update. The 10-second update period was used for FP1.
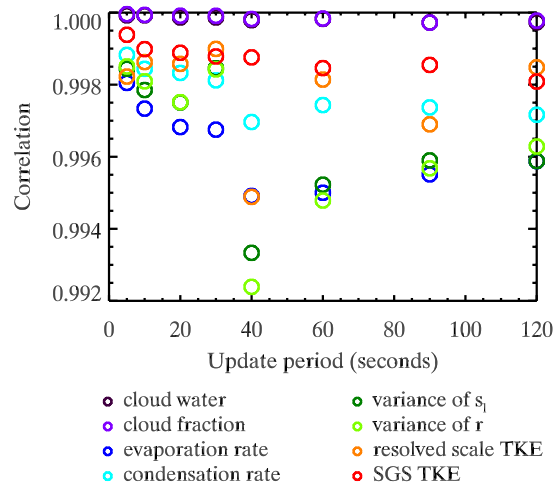
Figure 4.8   Correlation to the update period 0.5 second for selected time series. s_l is liquid water static energy and r is total water mixing ratio.

The 1.25 second update period was used for FPH. This is equivalent to five time steps. The scalar advection modifies a local column radiative flux profile. The horizontal grid size was made seven times smaller, thus the update period should be smaller than 1.42 seconds. RRTM is roughly 4.4 times more expensive than the GCSS parameterization. About 37% of the total cost was used by RRTM. The five second update period was used for FP2.

A simulated cloud picture for FPH viewed from a satellite created with the ray-tracing method is presented in Figure 4.9. There are many cloud holes with very little or no condensate, which would be filled by cloudy air or larger cloud holes if we used coarser resolution. Animation shows that the cloudy air is produced like spring water pouring out from multiple updrafts. Then the cloudy air moves horizontally. These near-

cloud-top horizontally divergent motions push the cloud holes, which merge together or break into smaller holes. The horizontal rolls of vortex-like motion in both clockwise and counter-clockwise directions were observed where the holes are merged together. The cloud holes seem to form streaks, but these streaks are diminished by the horizontal expansion of the cloud top. The simulated clouds seemingly attempt to form closed cells but they are prevented due to the small simulation domain.
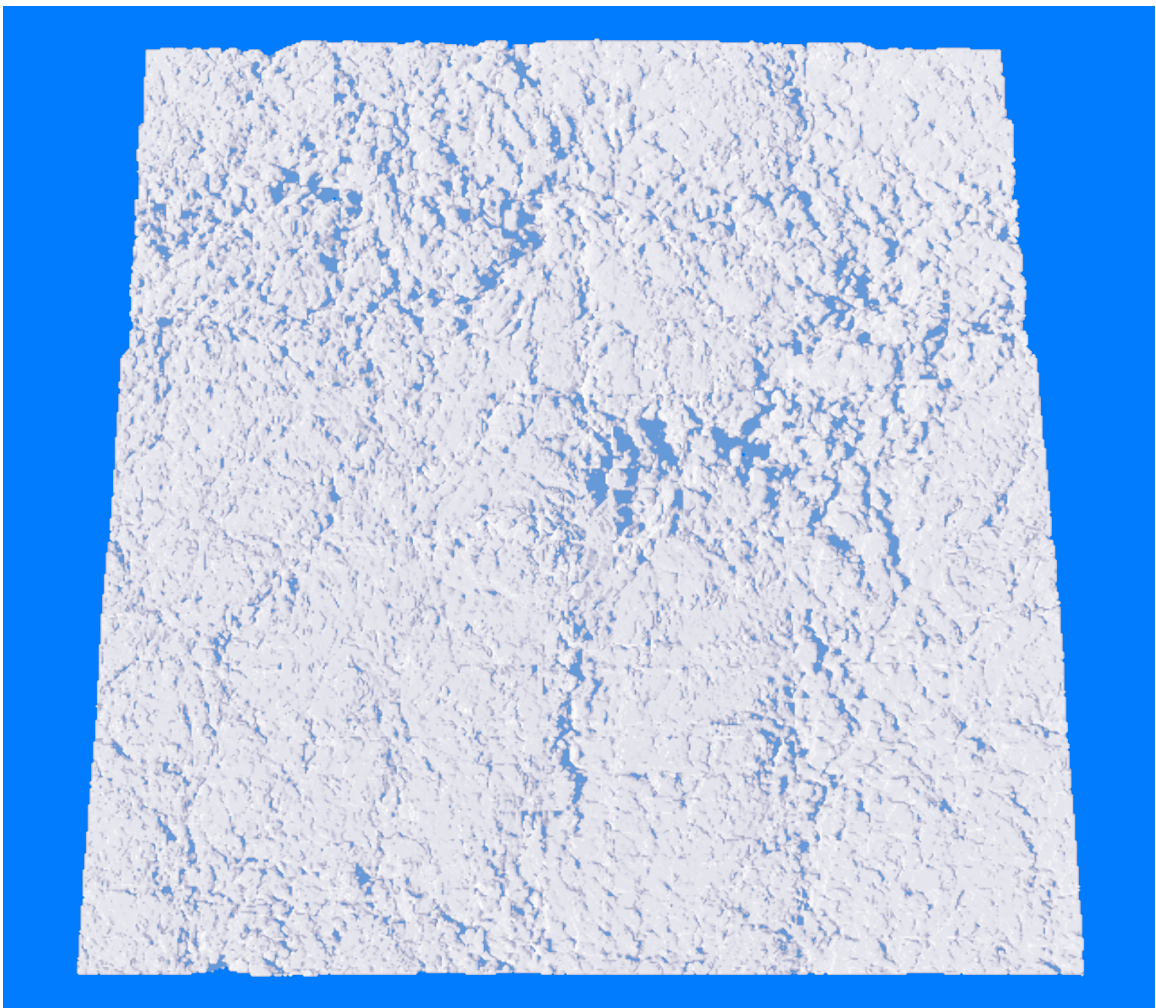
Figure 4.9   Satellite view of simulated clouds for FPH at 225 minutes. The ray-tracing method was used.

A three-dimensional snapshot picture of the cloud water of FPH is presented in Figure 4.10. The animation of the pictures shows that the cloud holes are filled with downdrafts, and stronger downdrafts tend to exist in larger holes. The updraft areas generally have lower cloud base and higher cloud top than the downdraft areas, which is reasonable since the updrafts contain more moisture due to the surface evaporation, and updrafts can overshoot at the cloud top. A closer look at the animation shows that very small cloudy air parcels detach from the cloud top and evaporate immediately. They may be classified as detrained. This detached cloudy air parcel seems to exist frequently around the cloud holes.
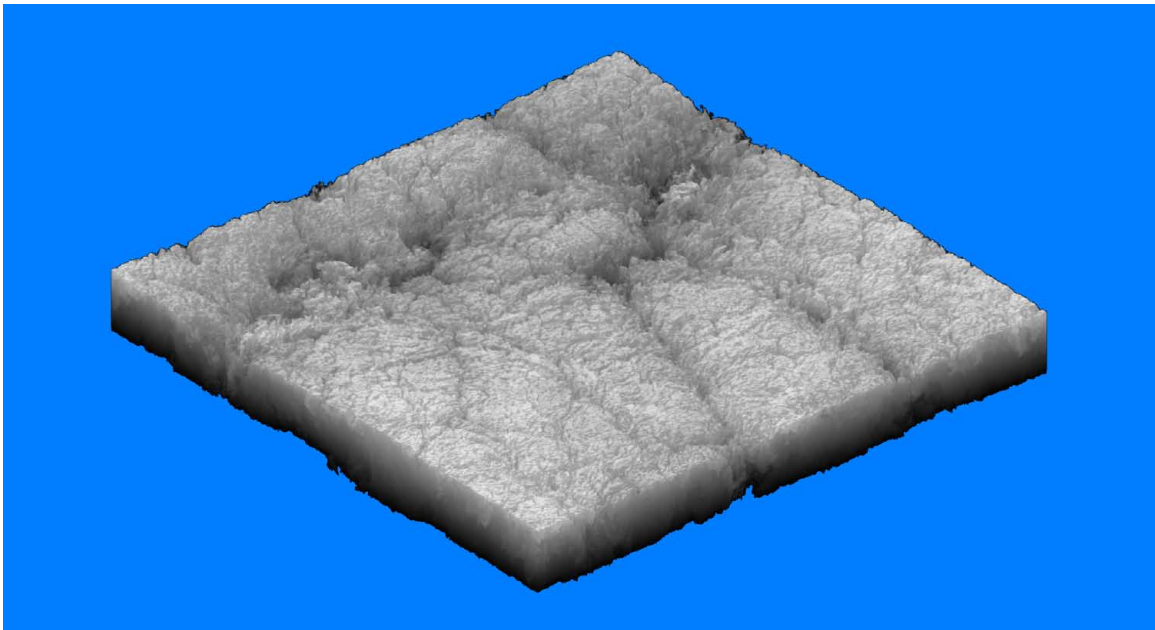
Figure 4.10 Three-dimensional snapshot picture of cloud liquid water for FPH at 225 minutes. Larger cloud water amount is whiter.

The turbulence is well represented for FPH. The power spectra of the vertical velocity shown in Figure 4.11 suggest an good agreement with the energy cascade line in the mixed layer below approximately 830 m. The agreement also holds in the lower half

of the inversion layer between 830 and 860 m. These slopes, less than the wave length of 20 m, i.e., four grid sizes, are slightly stronger than $\kappa^{-5/3}$.
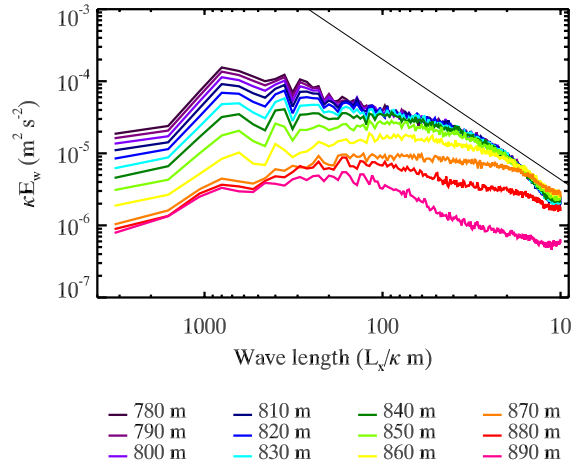
Figure 4.11   Power spectra of the vertical velocity for FPH at four hours. Notations are the same as Figure 4.7.

Changing the configuration from GCSS to FP1 as well as refining the resolution (FP2 and FPH) has a large impact on the simulated fields. Refining the vertical resolution with exactly the same configuration such as GCSS results in a cooler, moister mixed layer with more cloud water and a thicker cloud (S05; M. Khairoutdinov 2010, personal communication). The turbulence becomes stronger and more downdraft oriented: the variance of vertical velocity becomes larger and the profile of the third moment becomes negative throughout the mixed layer.

As shown in Figure 4.12, the FP cases are cooler and moister in the mixed layer than GCSS, so that they have more cloud water and thicker cloud fraction. FP2 is cooler than FP1 but FP2 is less moist than FP1. The FP cases use a different radiation update period depending on the grid spacing, and compute surface flux, so that the configuration

is not exactly the same. Refining the horizontal resolution provides a warmer and moister mixed layer.
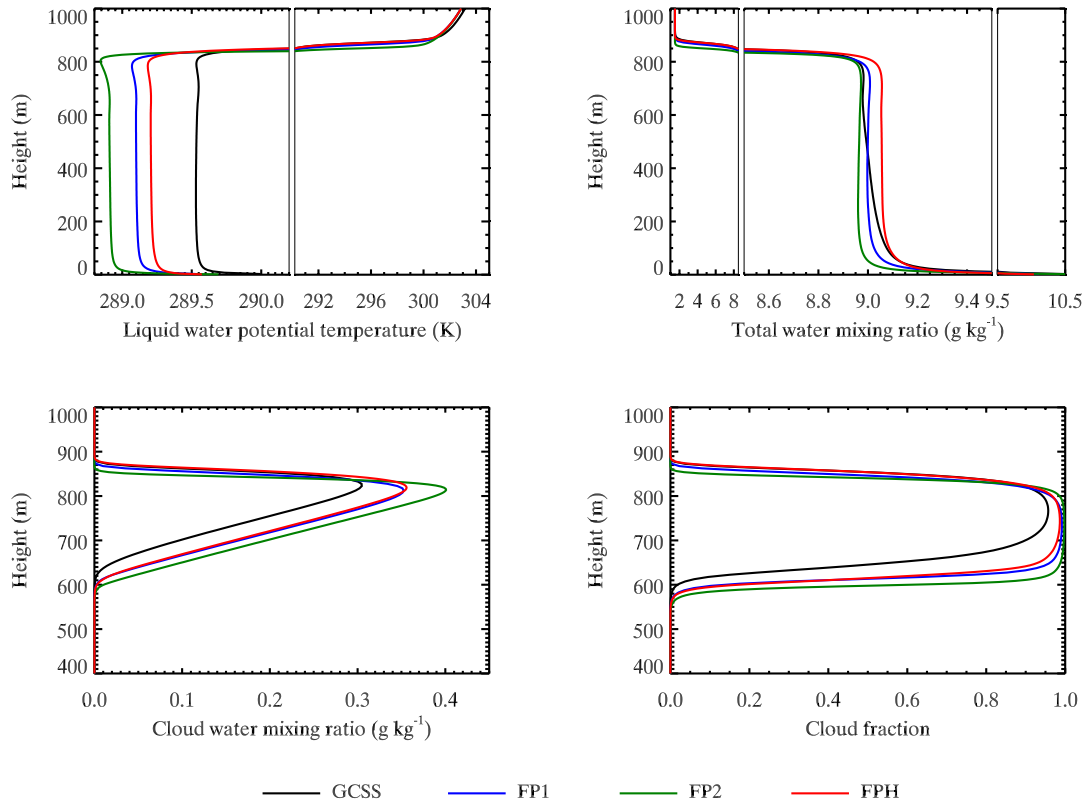
Figure 4.12   One hour averaged horizontal mean vertical profile. The average was taken for the last hour.

Time series of the selected variables are shown in Figure 4.13. The small differences of the model configurations result in large differences. The turbulence of FPH is strongest, and its entrainment rate is also largest, while it maintains a larger cloud water amount. The entrainment rate of FP2 is smallest; about three-quarters of FPH. The main difference between FPH and FP2 is the horizontal grid spacing. The smaller grid spacing is expected to better represent entrainment, and the difference of entrainment rate suggests that the 35 m horizontal grid spacing is too large. The surface flux of FP1 is

somewhat closer to GCSS, while the other two cases are noticeably different. The impact of the resolution to resulting turbulence is large.
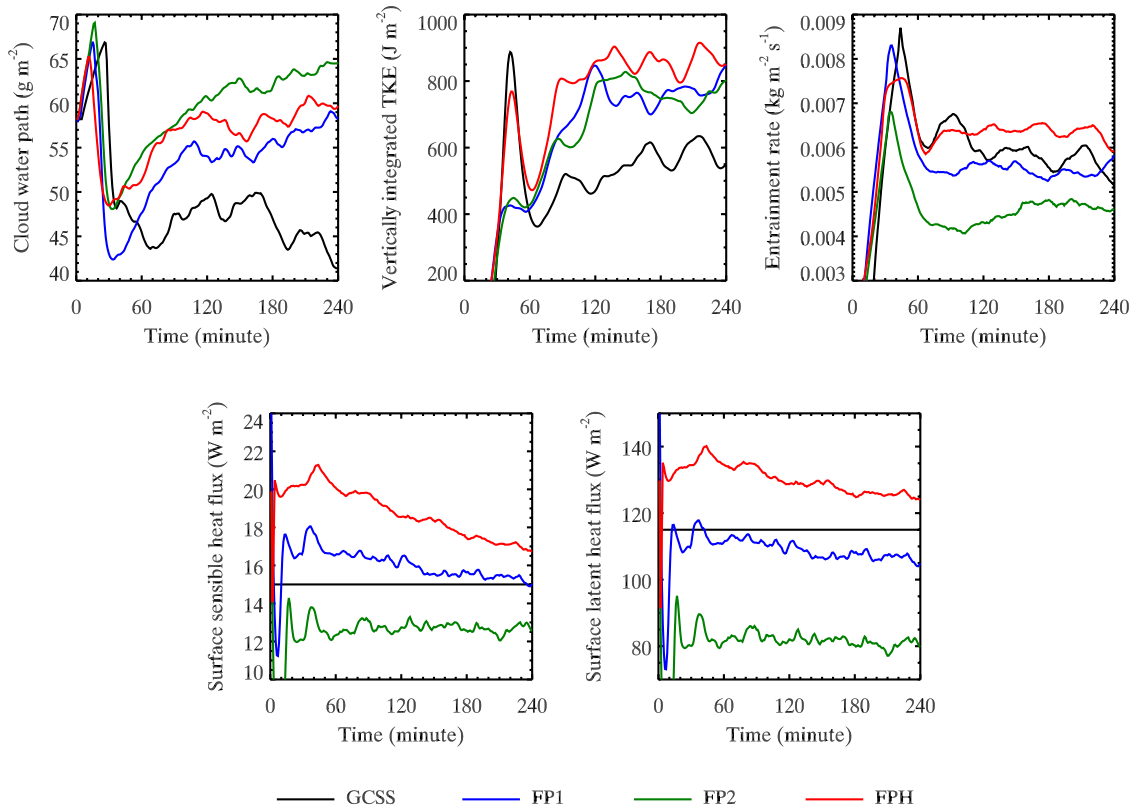
Figure 4.13   Time series of selected variables. Entrainment rate was computed with 30-minute running mean profiles.

The additional vertical profiles are presented in Figure 4.14. The turbulent activity is weaker for GCSS in terms of the buoyant production of TKE and variance of vertical velocity. Although the maximum buoyant production of TKE matches for the FP cases, the sub-cloud layer is different. The third moment of vertical velocity of FPH is well-matched with the estimated value by observation shown in Figure 5 of S05. The radiative heating profile suggests that the GCSS parameterization is insufficient; its maximum cooling rate is about 1 K smaller than RRTM for the same resolution, i.e., GCSS and

FP1. FPH is expected to best represent the condensation-evaporation process with the smallest grid volume. The evaporation rate for other runs significantly differ from FPH, but they have somehow similar magnitude for the net evaporation.
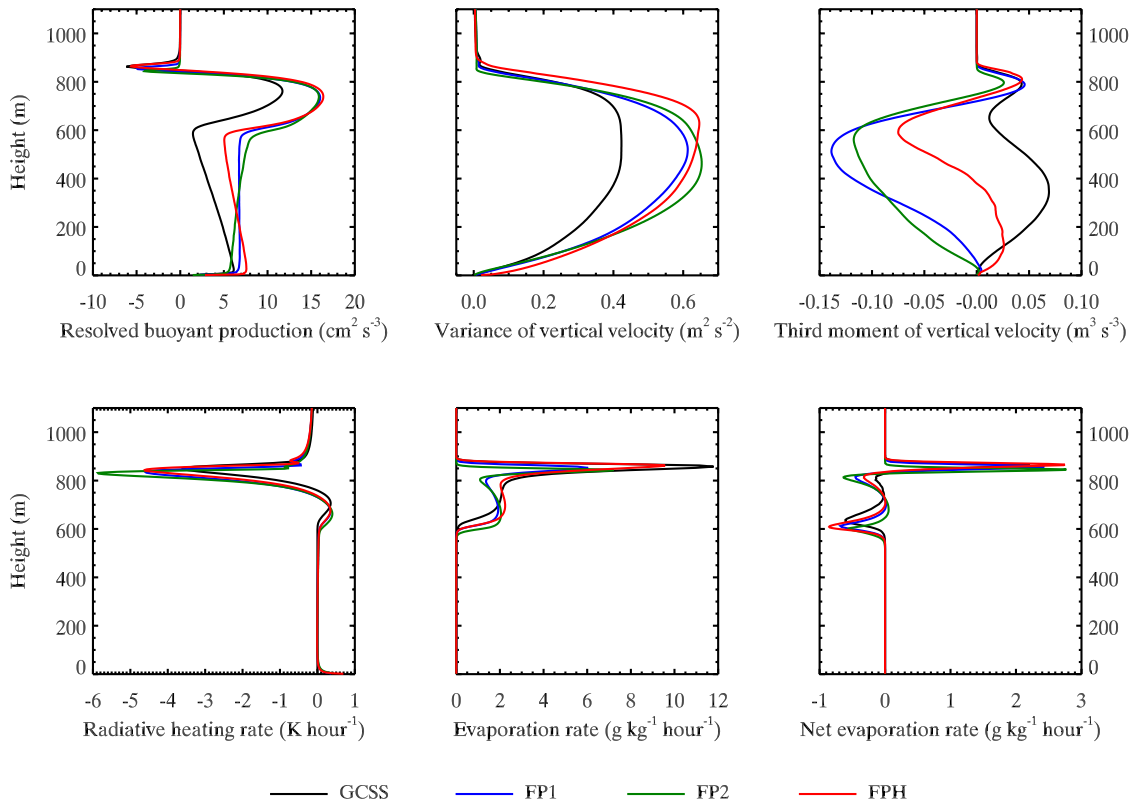
Figure 4.14 One hour averaged vertical profiles.

FPH probably best represents MSC. Other runs show disagreements with FPH for some parameters. Refining the vertical resolution is important, refining horizontal resolution is, however, also as important as vertical resolution, especially for entrainment and phase change. If the result of FPH is converged is a question worth to confirm. We keep this as our future study.

Chapter 5.   Cloud-Top Entrainment

5.1.   SAM-LPTM run

A SAM-LPTM run was performed for the last hour of the FPH simulation. Parcels were placed uniformly at all scalar points in a horizontal direction for 100 layers every 1 m of vertical distance between 851.25 and 951.25 m height. More than 40 million parcels were tracked. The 850 m level is near the middle of the inversion layer when parcels are released.

The additional numerical cost is large with this number of parcels; nearly double the numerical cost was required for the one-hour SAM-LPTM run compared with the one-hour SAM run.

The parcel data were saved every minute. Geographical location, velocity components, temperature, water vapor mixing ratio, and cloud water mixing ratio as well as one-minute-mean radiative tendency were output. One-minute-mean radiative tendency was computed by integrating the radiative heating rate by every time step then dividing by 60 seconds.

Entrained parcels were conditionally sampled using a very simple method. We tested each parcel to see if its initial SGS TKE was less than 10^{-6} m^2 s^{-2}, which means the parcel was in non-turbulent flow. Parcels can be in the inversion layer initially. We will impose an additional condition such that parcels initially have to be above the inversion layer for our mixing fraction analysis. The parcels satisfying the above condition were

judged as entrained if their vertical height once reached 50 m below the horizontal mean mixed layer height, level *B*. The first time the parcel reached below the mixed layer height was assigned as the time of the entrainment for the parcel. Approximately 164,000 parcels were conditionally sampled. The heights of the inversion and mixed layer are diagnosed with the method discussed in Appendix C.

5.2. Where does entrainment happen?

The "geographical" location of entrainment is actually unknown. Here geographical location means the horizontal point with respect to cloud water. Studies of the cloud-top entrainment usually assume that the entrainment takes place in drier areas. Figure 5.1 shows the location of the entrained parcel at the time of the entrainment. Entrained parcels are generally found in drier holes occupied by a downdraft. The concentration of entrained parcels appears to be larger at the larger holes.
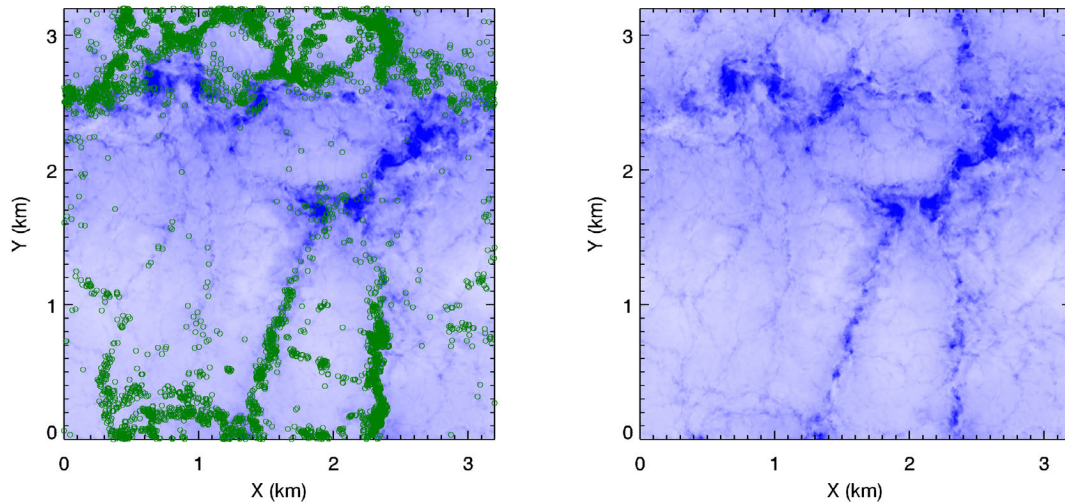
Figure 5.1   The geographical location of entrainment at 45 minutes, which is the same time for Figures 4.9 and 4.10. About 6,500 parcels are conditionally sampled as entrained at 45 minutes, and superimposed with a green circle over the albedo. The right albedo picture is the same as the left for comparison.

The time evolution of the geographical location for all parcels entrained at 45 minutes is shown in Figure 5.2. Interestingly, these parcels are initially clustered in particular places. Up until 43 minutes, the location of these parcels is less directly related to the dry holes. The parcels are quickly aligned after 43 minutes, and entrained. As shown in the figure, many parcels contain cloud water during the last two minutes.
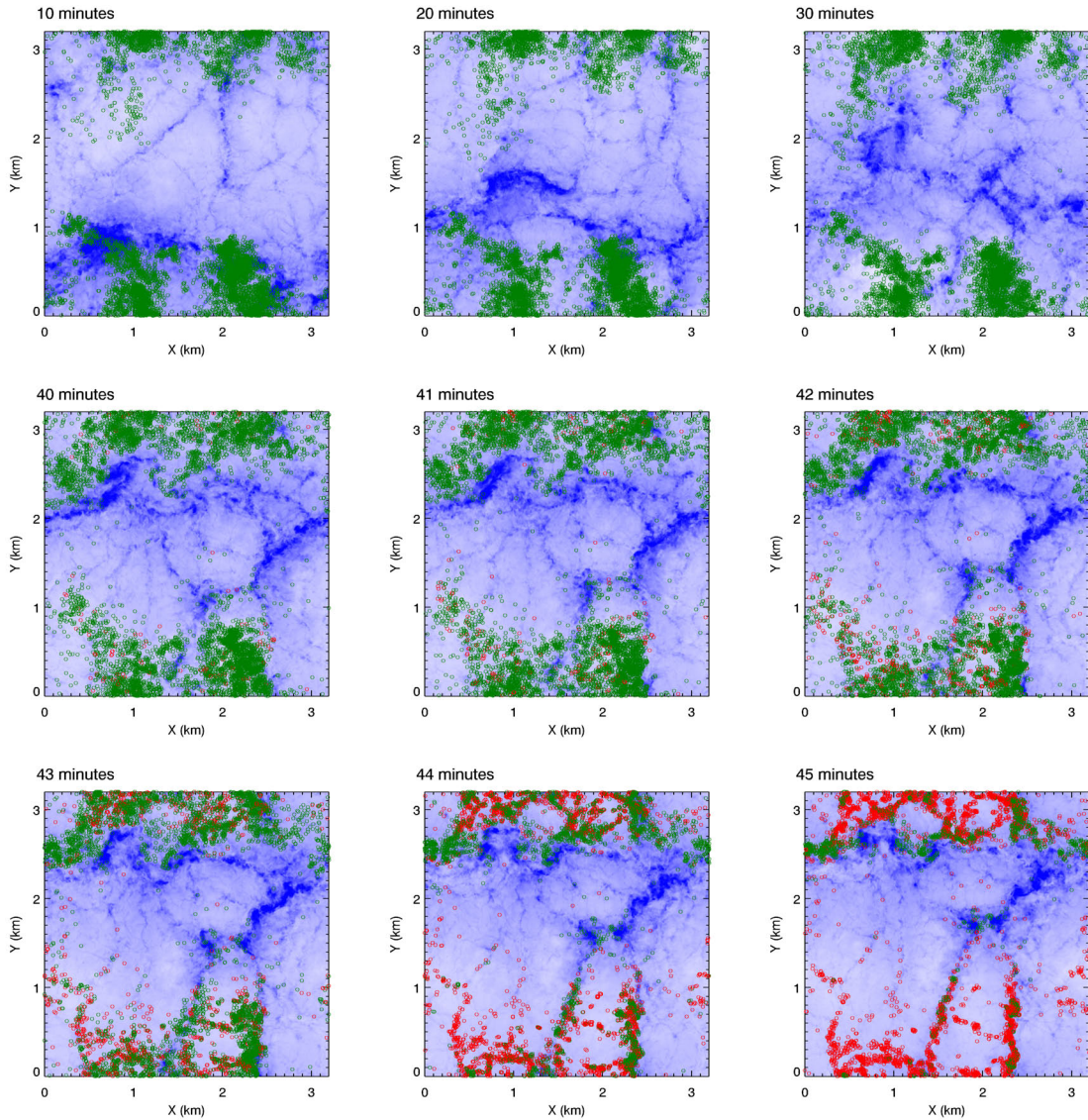
Figure 5.2   Geographical location of the parcels entrained at 45 minutes. Green parcels are dry and red parcels have cloud water.

5.3.   Mixing fraction analysis

An example of the time evolution of the distribution of liquid water static energy and total water for the parcels entrained at 45 minutes are shown in Figures 5.3 and 5.4. For parcels in the figures, there are large differences in the period for entrainment; the longest period is 45 minutes, and the shortest period is approximately three minutes. These parcels are not entrained immediately after they approach the mixed layer top, or

59

the mixed layer value. Rather, they are moving down and hang in the inversion layer. During this period, they are continuously cooled and moistened toward the horizontal mean. When the parcels are entrained, the entrained parcel mean is about 1 K warmer and about 0.5 g kg^{-1} drier than the horizontal mean. The time evolution described here is common so that it was observed with other parcels entrained at different times.
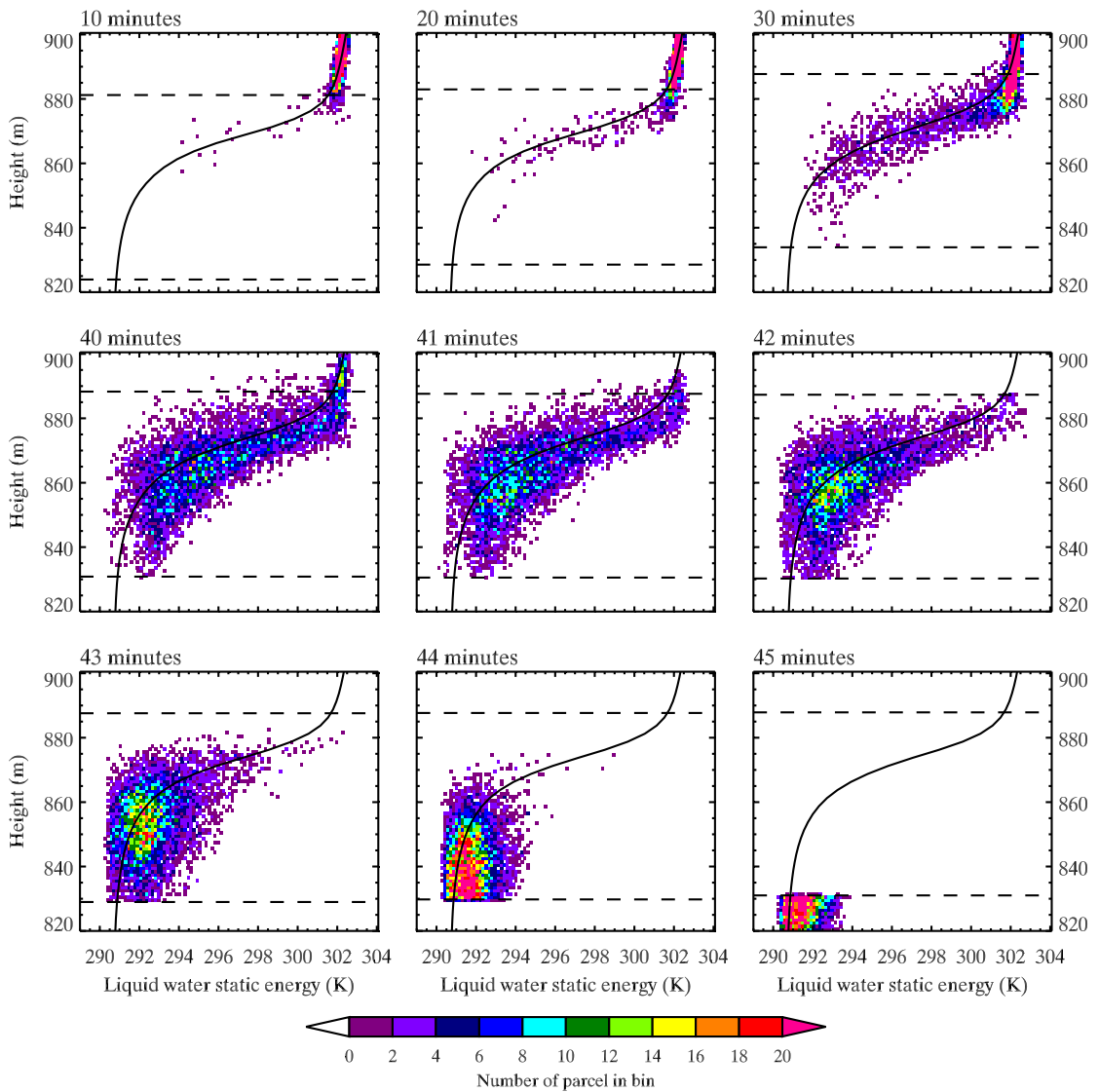
Figure 5.3   Distribution of the liquid water static energy with the height for the conditionally sampled entrained parcels. The solid line is the horizontal mean profile. The dashed lines are the inversion and mixed layer heights.
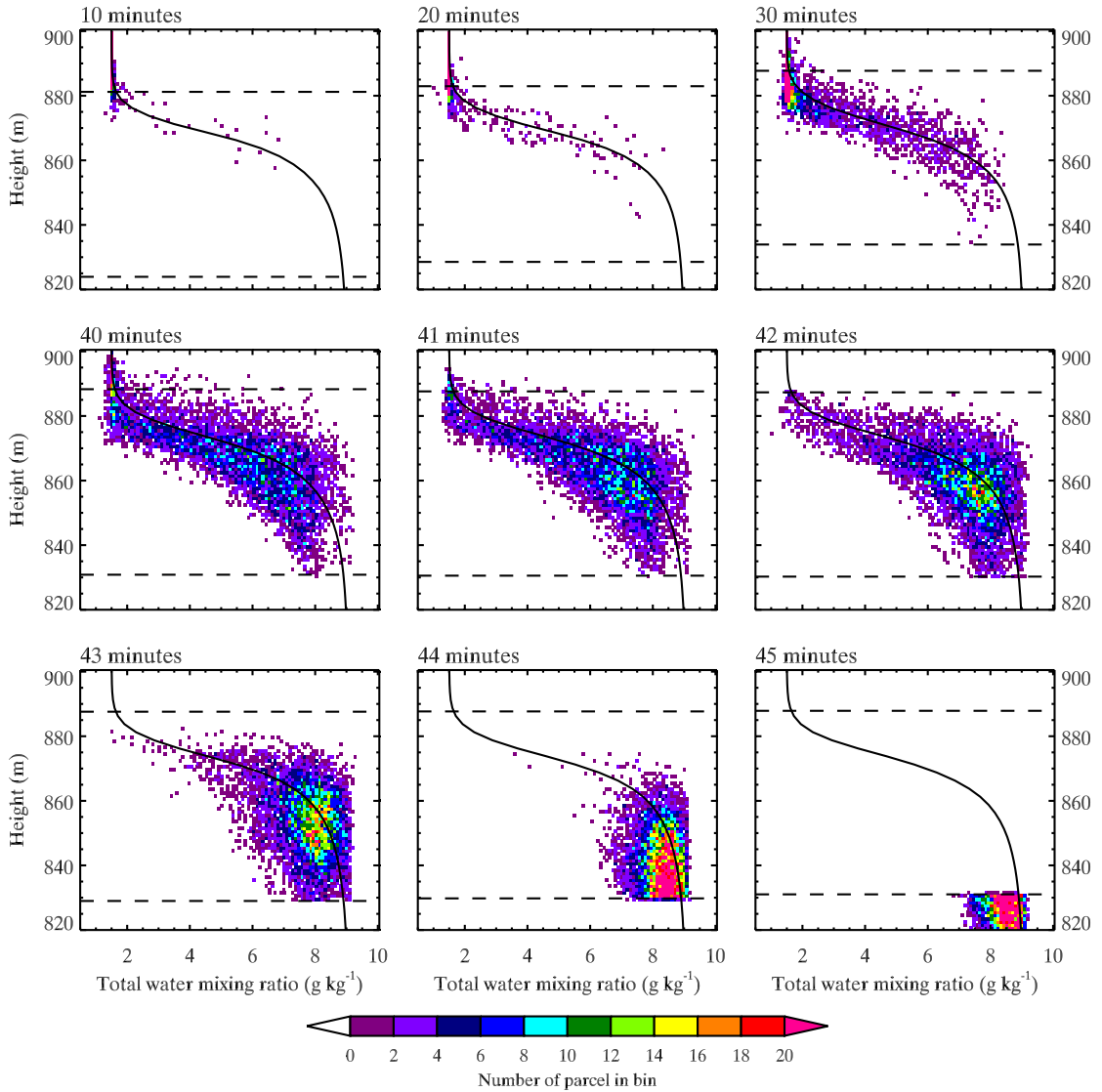
Figure 5.4   These are the same as Figure 5.3, but for total water mixing ratio.

Physical processes acting on the entrained parcels are better understood with the mixing fraction rather than the vertical position, since the distribution is much less noisy. Consider the equation in terms of the mixing fraction for total water mixing ratio, liquid water static energy, and virtual dry static energy for parcels in the case of DYCOMS-II;

$$
\begin{cases}
\delta r = \chi \Delta r \\
\delta s_l = \chi \Delta s_l + \left(\delta s_l\right)_{\mathrm{RAD}} \\
\delta s_v = \chi \Delta s_v + \left(\delta s_v\right)_{\mathrm{NEVP}} + \left(\delta s_v\right)_{\mathrm{RAD}}
\end{cases}
, \qquad (5.1)
$$

where $\delta(\ ) = (\ )_{\mathrm{parcel}} - \overline{(\ )}_B$ is the local fluctuation compared to the mean of the mixed

layer top. The subscript NEVP denotes net evaporation, i.e., evaporation minus

condensation. The first term in the r.h.s. for these equations is the contribution due to the

mixing, and it is linear with the mixing fraction. These equations are constructed only

with the processes at the cloud top so that the influence of the surface flux is assumed to

be negligible.

One way to proceed with the mixing fraction analysis is to use a traditional

approach (e.g., SR97 and VD02). The mixing fraction is first computed from the total

water mixing ratio by

$$
\chi = \frac{\delta r}{\Delta r}. \qquad (5.2)
$$

From the liquid water static energy equation and the mixing fraction, the radiative

cooling is obtained by

$$
\left(\delta s_l\right)_{\mathrm{RAD}} = \delta s_l - \chi \Delta s_l. \qquad (5.3)
$$

With the assumption of $\left(\delta s_v\right)_{\mathrm{RAD}} = \left(\delta s_l\right)_{\mathrm{RAD}}$, the net evaporative cooling is computed as

$$
\left(\delta s_v\right)_{\mathrm{NEVP}} = \delta s_v - \chi \Delta s_v - \left(\delta s_v\right)_{\mathrm{RAD}}. \qquad (5.4)
$$

This traditional approach is simple and straightforward, but strongly depends on the

reference values, i.e., values at levels B and $B+$. For our examination with the LPTM

output, the mixing fraction diagnosed with (5.2) may produce artificial radiative warming for the parcels with warmer liquid water static energy than the level $B+$ value. We will discuss more detail of this problem later. By setting the level $B+$ higher and higher, the radiative cooling becomes stronger and stronger due to a large jump value for a larger mixing fraction. These are schematically illustrated in Figure 5.5. The similar results shown in Figure 5 of VD02, which shows the quasi-linear relationship between the mixing fraction and radiative heating amount with largest cooling at the level $B+$, was reproduced for the LPTM data with higher level $B+$. The net evaporative cooling is also affected and tends to be large for higher level $B+$. The dependency of the reference value is undesirable so that SR97 developed another method by proposing an assumption such that the radiative cooling is independent of the mixing fraction. VD02 argued that the assumption is not justified. Our results presented later, however, suggest that the assumption is somewhat justifiable.
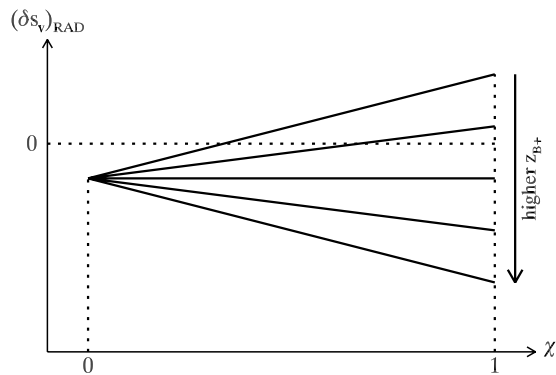
Figure 5.5   Highly simplified schematics for the radiative heating obtained with (5.2) and (5.3) for different level $B+$ with LPTM output.

For the observational data, the reference values could be calibrated by comparing the liquid water amount as well as saturation mixing fraction obtained from both

observation and theoretical diagnosis (S. Krueger 2010, personal communication). The method, however, cannot be applied for LPTM since LPTM theoretically diagnoses cloud water amount with the SAM's microphysics parameterization with the interpolated liquid water static energy, total water mixing ratio, and pressure.

The artificial radiative warming above level $B+$ appears to be the result of the use of the mixing fraction computed from the total water mixing ratio. The problem comes from the zero vertical gradient for the initial profile of total water mixing ratio. With fixed level B, the jump for the total water mixing ratio is the same for any level $B+$ in the free atmosphere, while the jump for the liquid water static energy increases as level $B+$ becomes higher. In the free atmosphere there is no turbulent mixing, so that the parcels' mixing fraction in the free atmosphere are always or very close to 1 if the total water mixing ratio is used to compute the mixing fraction. By substituting $\chi = 1$ in (5.3), one obtains for parcels above level $B+$

$$\left(\delta s_l\right)_{\text{RAD}} = \left(s_l\right)_{\text{parcel}} - \left(\bar{s}_l\right)_{B+} > 0. \tag{5.5}$$

For the traditional approach, The radiative cooling amount is indirectly obtained with (5.3), which is the residual of the subtraction in the r.h.s., that is, the traditional approach tends to impose errors on the radiative cooling amount. For this reason, the mixing fraction computed from the total water mixing ratio does not necessarily work properly for the liquid water static energy.

With LPTM, the mixing fraction can be obtained with the liquid water static energy equation, (5.3). The advantage of LPTM is that it can collect any desired variables

following a parcel path. By time-integrating the radiative heating rate for each parcel during entrainment, the mixing fraction can be diagnosed as

$$\chi^t = \frac{\left(\delta s_l\right)^t - \left(\delta s_l\right)^t_{\text{RAD}}}{\Delta s_l},$$
(5.6)

where t is the time index. As discussed in Chapter 3, LPTM has a limit of its capability for diagnosis with the spatial interpolation. Figure 5.6 shows the relative magnitude to the absolute maximum value for the vertical velocity and radiative heating rate. The radiative heating rate is somewhat smoother than vertical velocity, except the transition boundary from negative to positive, where air suddenly changes from cloudy to clear. Although it is noisier than the liquid water static energy (not shown), the interpolated radiative heating rate is probably well represented. The result encourages us to use (5.6) to compute the mixing fraction.
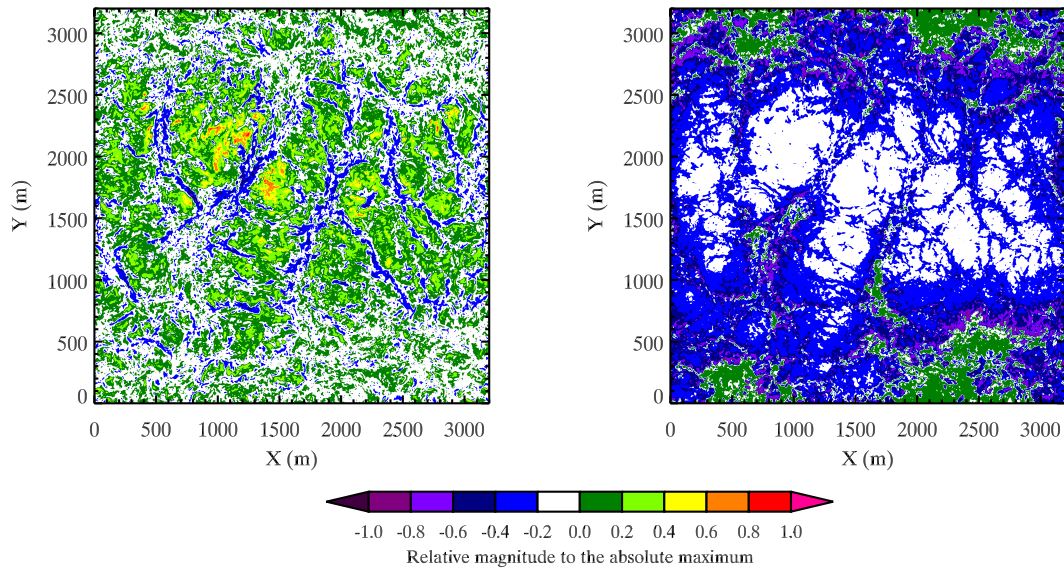
Figure 5.6   Relative magnitude to the absolute maximum value for the vertical velocity (right) and the radiative heating rate (left) at the mixed layer height.

65

In order to time-integrate the radiative heating rate during entrainment, a parcel has to be initially above the inversion. A total of 161,000 parcels were sampled out of all the entrained parcels. For each sampled parcel, when the parcel's vertical position is first below level $B+$, the time of the initiation of entrainment is decided by

$$t_{B+} = \begin{cases} t-1 & \text{if } \left|z^{t-1} - z_{B+}^{t-1}\right| \leq \left|z^t - z_{B+}^t\right| \\ t & \text{if } \left|z^{t-1} - z_{B+}^{t-1}\right| > \left|z^t - z_{B+}^t\right| \end{cases}. \tag{5.7}$$

When the parcel's vertical position is first below level B, the time of the completion of entrainment is decided in the same way:

$$t_B = \begin{cases} t-1 & \text{if } \left|z^{t-1} - z_B^{t-1}\right| \leq \left|z^t - z_B^t\right| \\ t & \text{if } \left|z^{t-1} - z_B^{t-1}\right| > \left|z^t - z_B^t\right| \end{cases}. \tag{5.8}$$

The reference values for each parcel are assigned as

$$\begin{cases} \left(s_l\right)_{B+} = \left(\bar{s}_l\right)_{B+}^{t_{B+}} \\ \left(s_l\right)_B = \left(\bar{s}_l\right)_B^{t_B} \end{cases}. \tag{5.9}$$

The radiative cooling is integrated from t_{B+} up to t_B;

$$\left(\delta s_l\right)_{\text{RAD}}^t = \sum_{i=t_{B+}}^{t} \left[\left(\frac{Ds_l}{Dt}\right)_{\text{RAD}}^i \Delta t\right], \tag{5.10}$$

where $\Delta t = 60$ seconds for our simulation. With (5.6), (5.9), and (5.10), the mixing fraction can be computed, and the net evaporative cooling is computed with (5.4). As SR97, VD02 and other studies, the radiative heating for the virtual dry static energy is assumed to be equal to that of the liquid water static energy.

Our mixing fraction analysis involves the entire history of all entrained parcels. Each parcel can be in any place in the inversion layer at any time so that the background field should be somewhat steady in order to plot the entire parcel data on to one mixing diagram. The important parameter for the mixing diagram is the saturation mixing fraction and corresponding maximum possible negative buoyancy. Figure 5.7 shows that these variables are, to some extent, steady during the simulation. The mean of the saturation mixing fraction is 0.054 and that of the maximum possible negative buoyancy is -0.184 K.
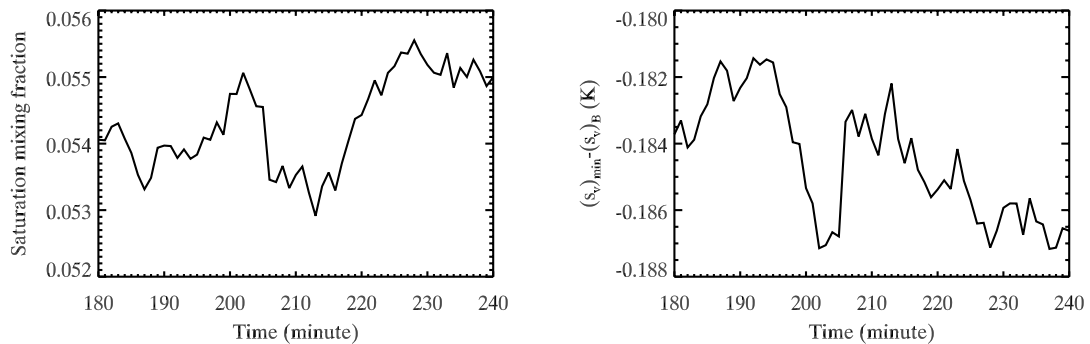
Figure 5.7   The time series of saturation mixing fraction and the maximum possible negative buoyancy during the SAM-LPTM run.

The mixing diagrams for the liquid water static energy, total water mixing ratio, and vertical position when parcels are released are shown in Figure 5.8. There are parcels with mixing fraction less than 1. They may be in the return flow to the boundary layer after overshoot so that they are relatively cool and moist.
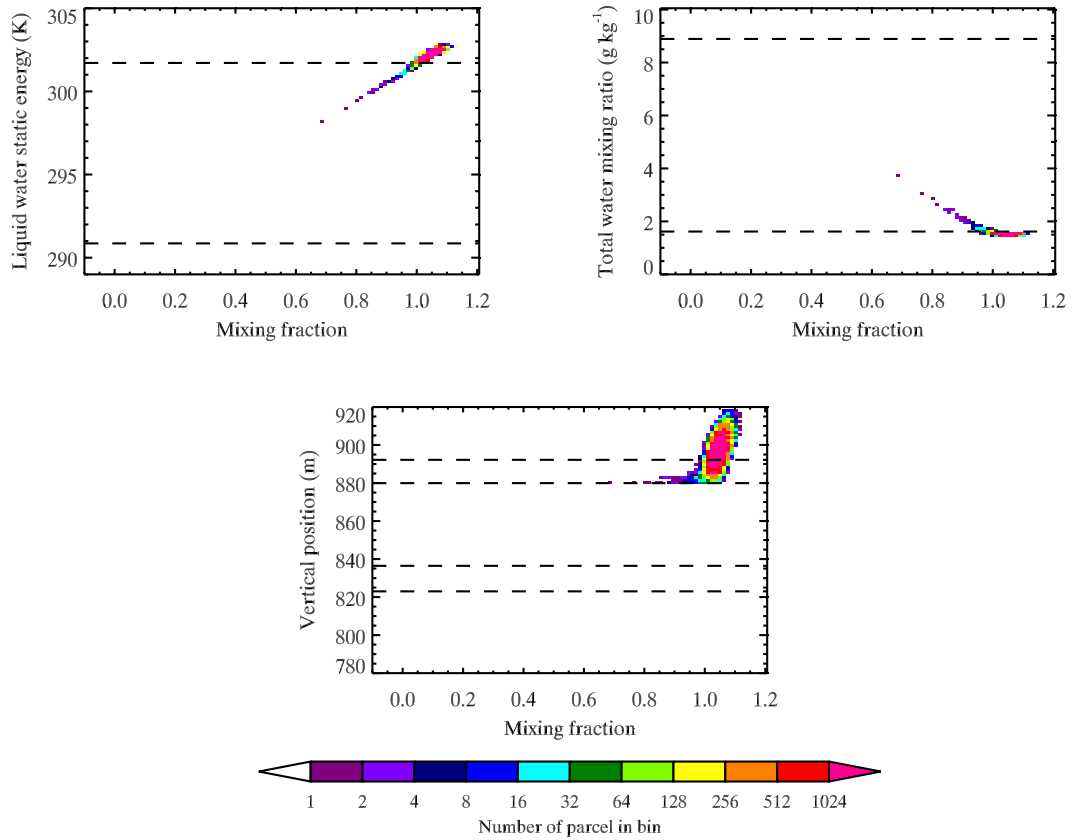
Figure 5.8   The mixing diagram of the liquid water static energy, total water mixing ratio and the parcel's vertical position at the LPTM initial time. Dashed lines are either levels B+ or B. They are hourly means for the liquid water static energy and total water mixing ratio. For the vertical position, the lowest and highest levels B+ (upper two lines) and B (bottom two lines) during the SAM-LPTM run are shown.

The mixing diagram for the virtual dry static energy, cloud water mixing ratio, and partitioned heatings when parcels are released is presented in Figure 5.9. Because the radiative heating was forced to be zero until t_{B+}, this created small evaporative cooling and warming at the initial time. The evaporative heating was adjusted by subtracting the initial evaporative heating so that the initial evaporative heating becomes zero:

$$\left(\delta s_v\right)^t_{\mathrm{NEVP}} = \left(\delta s_v\right)^t - \chi^t \Delta s_v - \left(\delta s_v\right)^t_{\mathrm{RAD}} - \left(\delta s_v\right)^0_{\mathrm{NEVP}}. \qquad (5.11)$$

68
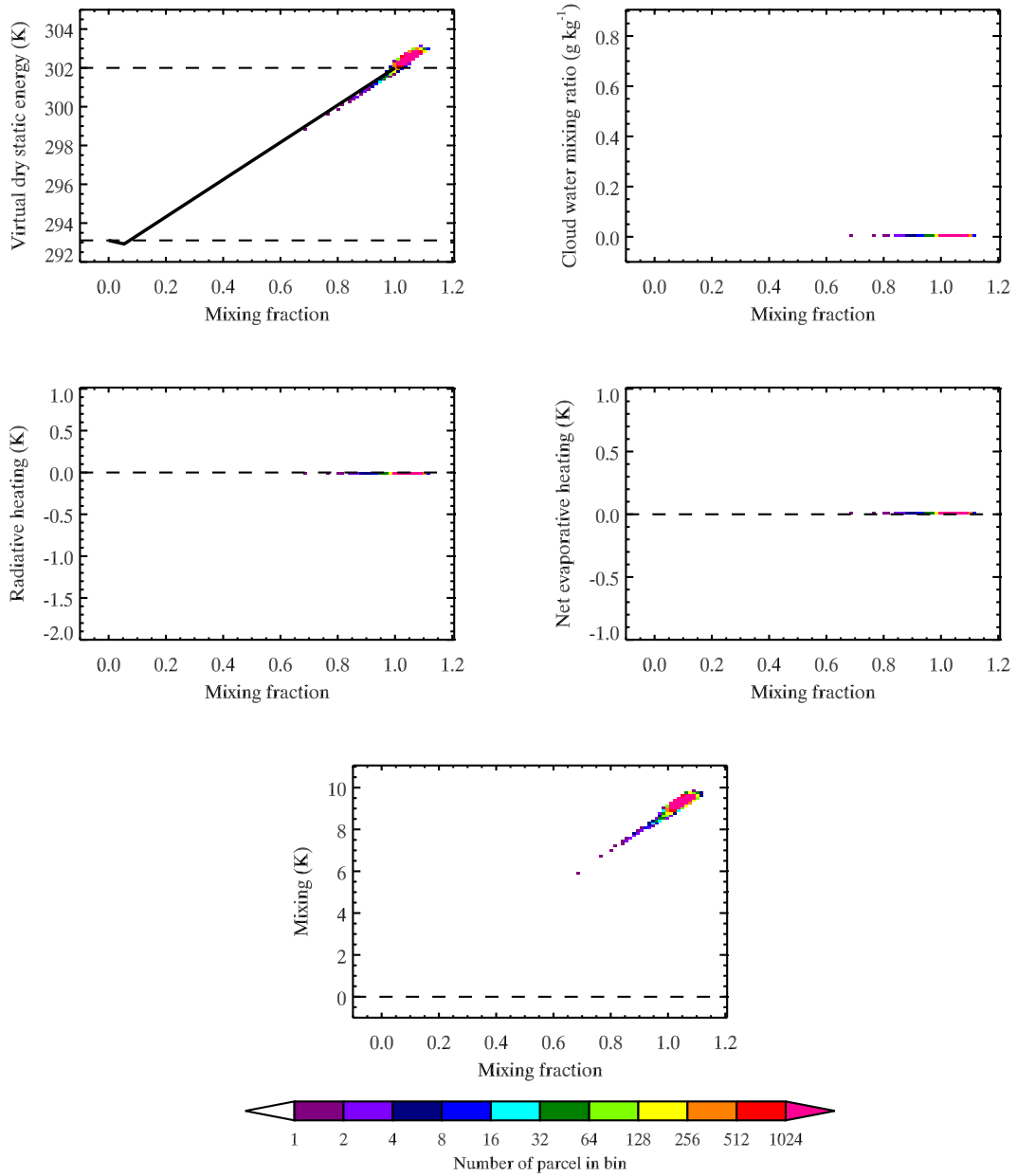
Figure 5.9   A mixing diagram for the virtual dry static energy, cloud water mixing ratio, and heating components due to radiation, net evaporation, and mixing, i.e., $\chi \Delta s_v$, at the initial time. The dashed lines for the virtual dry static energy are hourly means. The solid line for the virtual dry static energy is the theoretically derived mixing line based on the hourly mean horizontal mean data.

The mixing diagrams at t_{B+} are shown in Figures 5.10 and 5.11. When parcels reach level $B+$, some of the parcels have already been cooled and moistened. Both conservative variables are distributed similarly and form straight lines, but with opposite

slopes. The parcels at this time have variety of mixing fractions larger than 0, but they tend to be larger. Height is not a good parameter to study physical change during entrainment. The virtual dry static energy follows the theoretical mixing line. Some of the parcels are evaporatively cooled. These parcels could have interacted with overshot cloudy air. The mixing is linear.
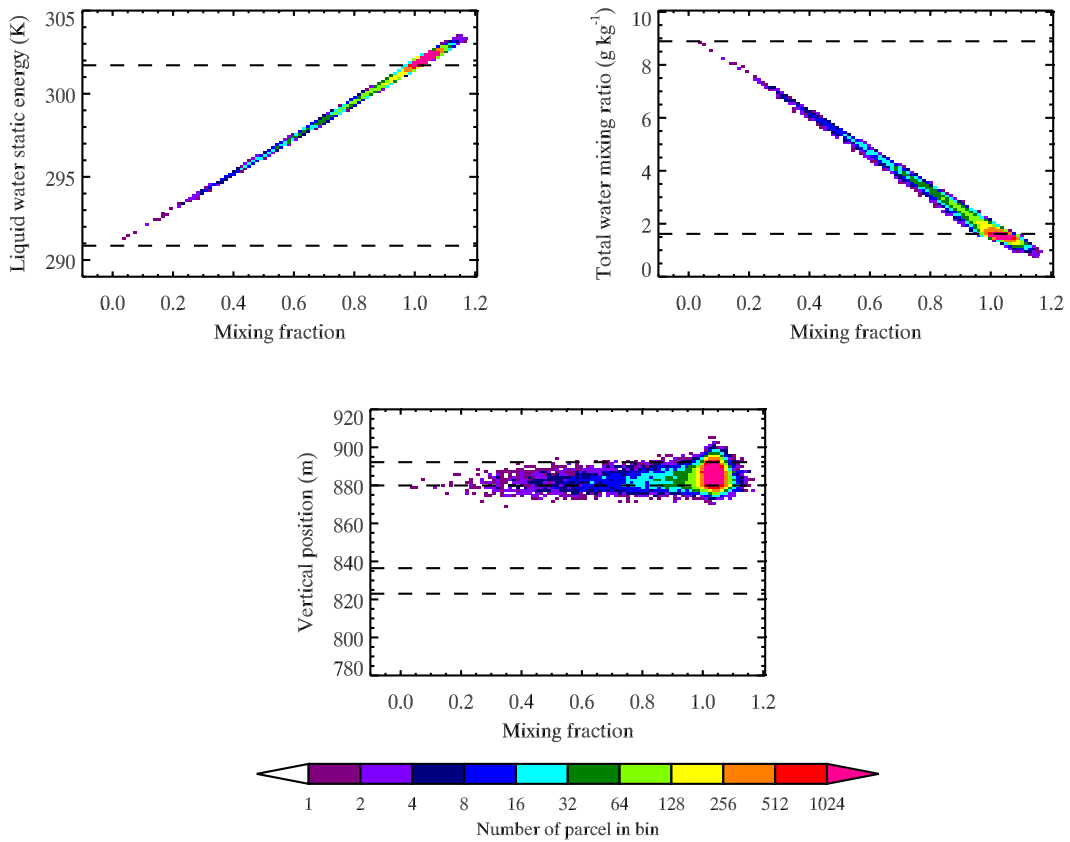
Figure 5.10   These are the same as Figure 5.8, but for the parcels closest to level *B*+.
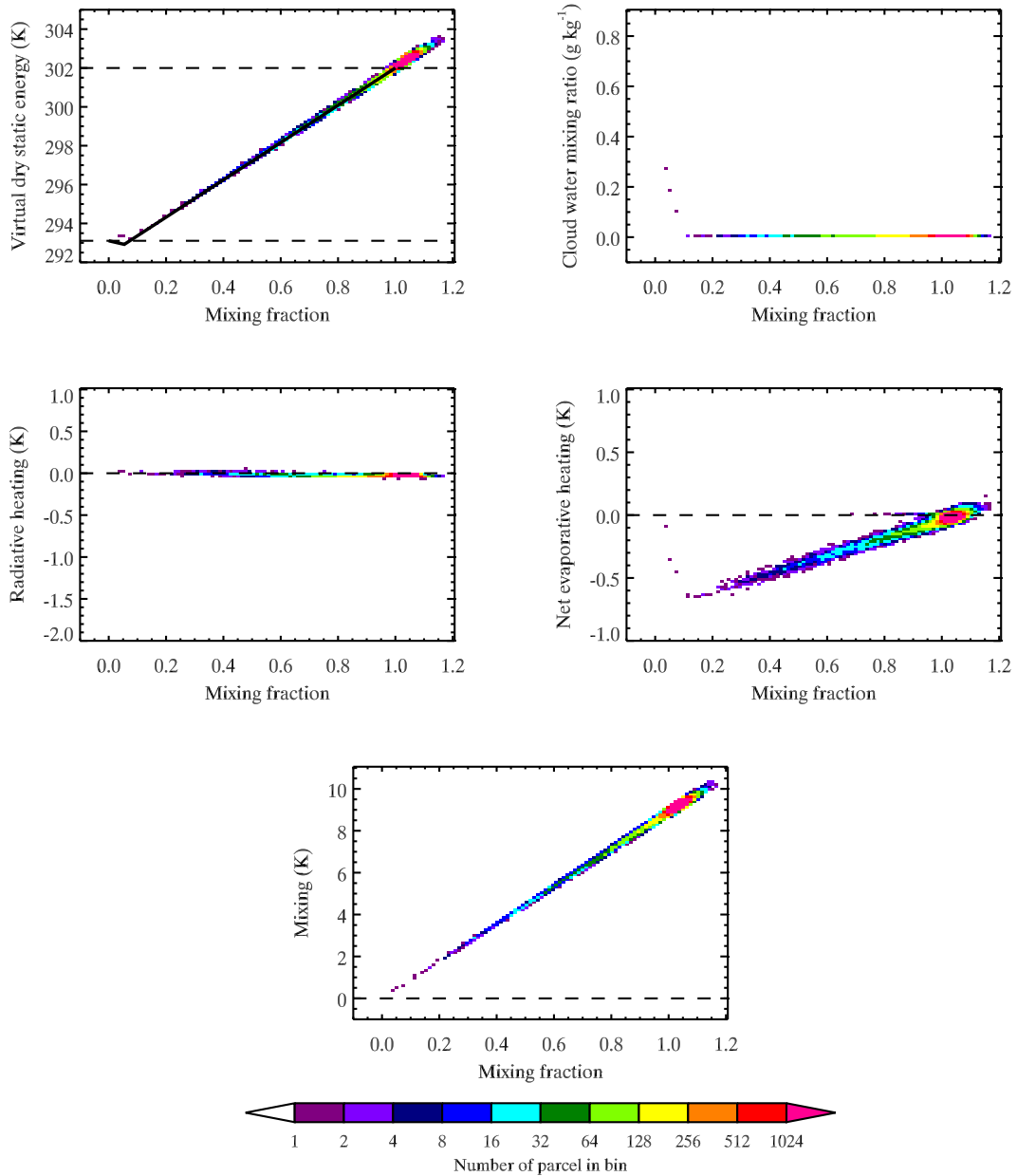
Figure 5.11   These are the same as Figure 5.9, but for the parcels closest to level *B*+.

The mixing diagrams at t_B are shown in Figures 5.12 and 5.13. At this moment of entrainment, mixing fractions are small. The moist conservative variables follow straight lines, which means that the radiative heating does not affect the linear profile. The virtual dry static energy follows the theoretical mixing line, which has a kink at 0.054. Buoyancy reversal occurs for many parcels. Some parcels reach a negative buoyancy at 0.15 mixing

fraction, which is relatively large. Parcels have cloud water less than 0.15 mixing fraction. As VD02 noted, the saturation mixing fraction for individual parcels can be larger than the horizontal mean value.
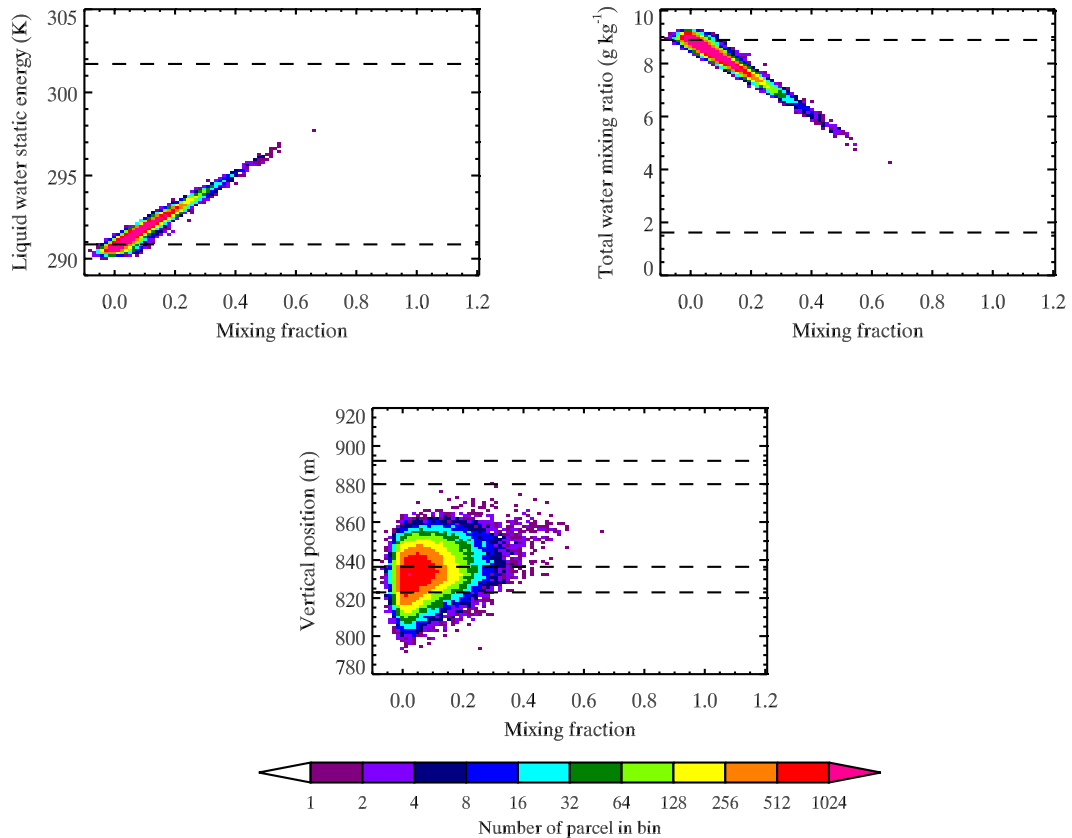
Figure 5.12   These are the same as Figure 5.8, but for the parcels closest to level *B*.

The radiative heating is non-linear with small fluctuation, ±0.5 K, which fits well in the distribution of the liquid water static energy. The radiative warming occurs for some parcels. It is possible for local radiative warming to exist for night-time MSC; for example, these parcels are not as warm as the surrounding air, or they are under cloudy air.
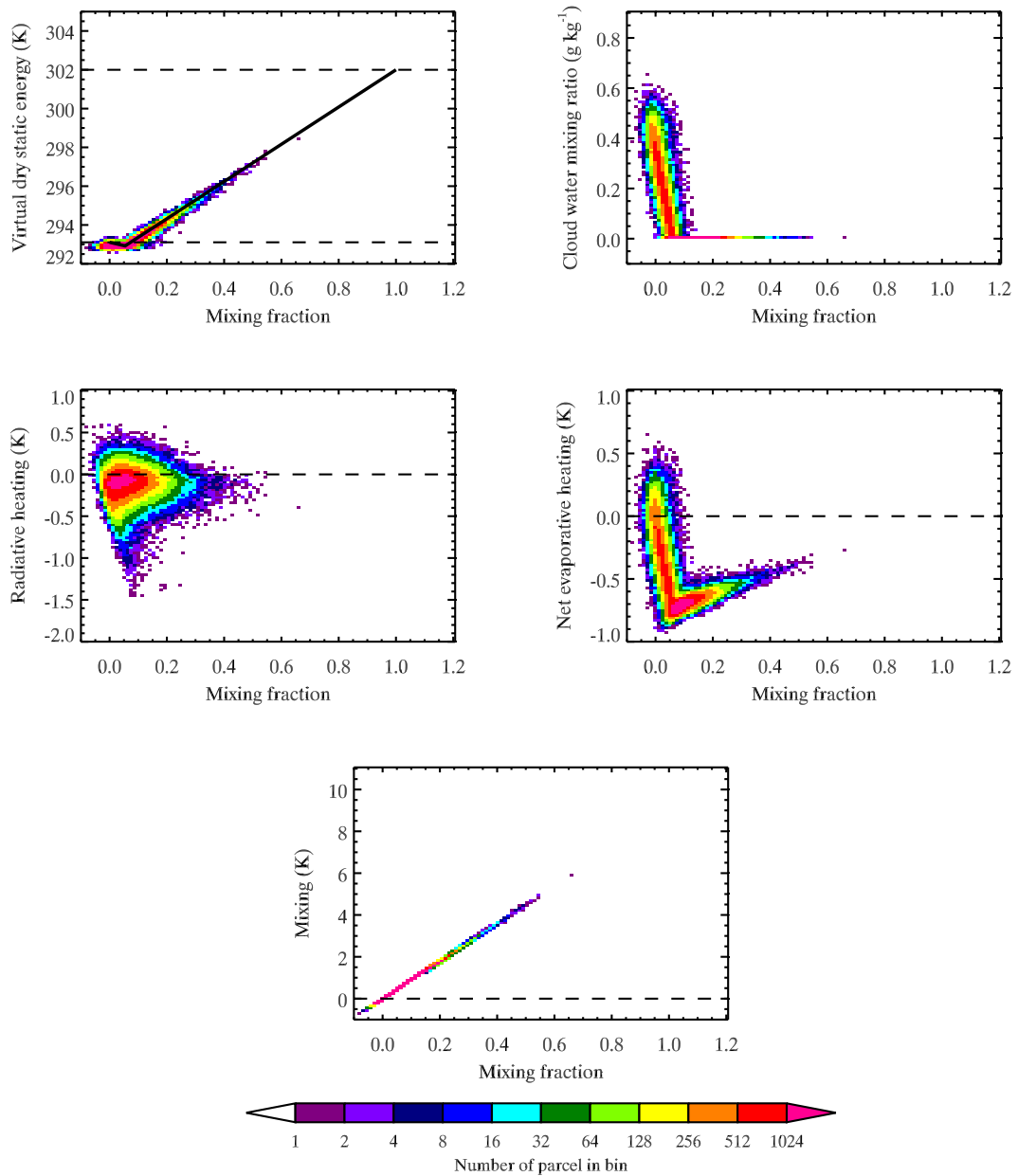
Figure 5.13　These are the same as Figure 5.9, but for the parcels closest to level *B*.

The net evaporative heating forms an expected shape. The evaporative cooling amount at the saturation mixing fraction is approximately 0.8 K, which is close to the estimated cooling amount of 0.83 K. SR97 shows that the net evaporative cooling can be estimated with

73

$$\left(\delta s_v\right)_{\mathrm{NEVP}}\left(\chi\right) = L\left[l\left(\chi\right) - \left(1 - \chi\right)\overline{l}_B\right].$$ (5.12)

Since the actual and the estimated maximum evaporative coolings are comparable, it suggests that our diagnostic method for the mixing fraction works well. The contribution of evaporative cooling is, at least, as large as that of radiative cooling for this case. This conclusion disagrees with previous studies (e.g., SR97 and VD02), which suggest that the contribution of radiation is greater than evaporation.

The mixing, $\chi\Delta s_v$, is linear with the mixing fraction. The positive mixing is, by definition, the amount of cooling required from the specific mixing fraction to the level B value by mixing. It is the largest contribution for the buoyancy reduction. This conclusion also disagrees with the previous studies. It is possible that numerical diffusion largely contributes to this large mixing. It is well known that numerical models generally suffer from dealing with a large and sharp gradient like the inversion layer.

It should be noted here that these disagreements come from the different diagnostic method for the mixing fraction. The results agreeing with the previous studies were reproduced with the traditional approach.

The small radiative cooling comes from the geographical locations of the entrained parcel path. Figure 5.14 shows the radiative heating rate at the level of the maximum cooling rate in terms of the horizontal mean, and corresponding cloud-top albedo at four hours. The radiative heating is very weak, ± 1 K hour^{-1}, in the cloud holes, where the parcels are entrained. The mean radiative cooling rate in the upper half of the inversion layer is less than 1 K hour^{-1} (Figure 4.14), that is, the entrained parcels are not exposed to a strong radiative cooling on the course of entrainment.
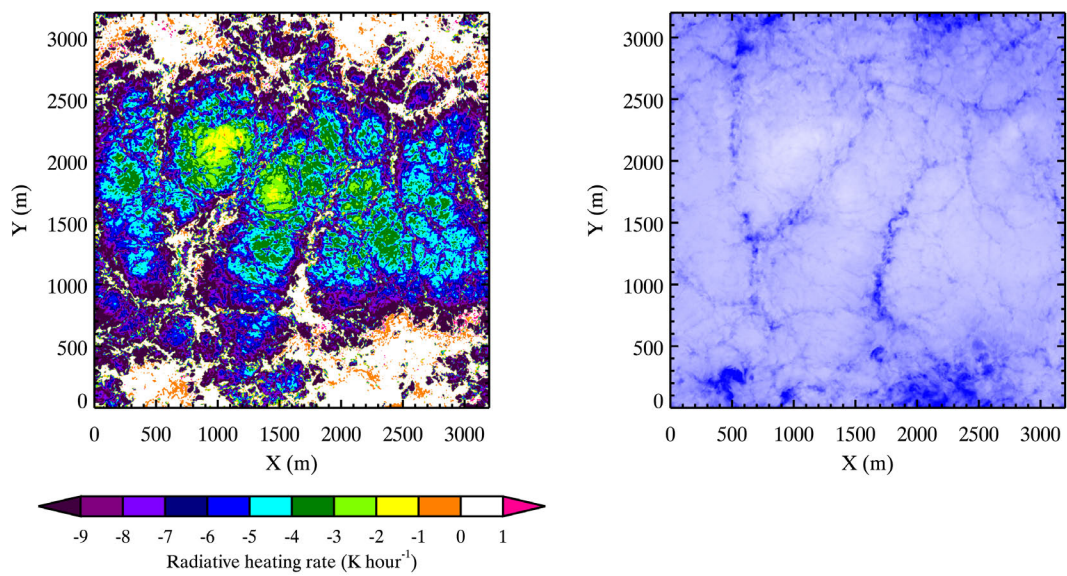
Figure 5.14 Radiative heating rate and corresponding cloud-top albedo at four hours. The height of the radiative heating rate is 846.25 m, which is the level of the maximum cooling rate in terms of the horizontal average and it is about -4.8 K hour^{-1}. This level is just above level *B*.

Chapter 6.   Interactions between radiative cooling and CTEI

6.1.   Hypothesis

Entrainment takes place at different places from where cloudy air is generated; the former is the downdraft and the latter is the updraft. The updraft tends to be cooler and moister than the downdraft (e.g., Figure 3.3b). The horizontal diverging motion near the cloud top transfers the cool and moist air toward the entrainment area.

We hypothesized that, as a bulk of the inversion layer, an interaction between CTEI and radiative cooling exists such that the radiative cooling always forces the saturation mixing fraction toward larger values while CTEI forces it toward smaller values if CTEI occurs but is hidden. For a steady-state MSC under CTEI conditions, these two processes find common ground so that the radiative cooling allows CTEI to work by supplying cloudy air. CTEI is active but hidden under the balance.

As shown previously, the time series of the saturation mixing fraction of BR-73-5m (Figure 4.5) decreases with time, whereas that of DYCOMS-II FPH is steady around 0.054 (Figure 5.7). The virtual dry static energy at both inversion and mixed layer tops are nearly steady for both cases. For BR-73-5m, CTEI consumes cloud water so that the saturation mixing fraction shifts toward smaller values.

In order for the saturation mixing fraction to be steady with the steady jump in terms of the horizontal mean, the cool and moist cloudy air has to be supplied continuously where buoyancy reversal takes place. If the supply is too weak, then CTEI

would be able to expand the cloud holes and thin the cloud layer as seen in BR-73-5m. YR08 suggest that the radiative cooling is the strongest cloud builder to produce and maintain the cool, humid air. Then, the radiative cooling actually maintains the steady saturation mixing fraction as schematically illustrated in Figure 6.1. This is an interesting view point since the radiative cooling preserves the maximum productivity of buoyancy reversal.
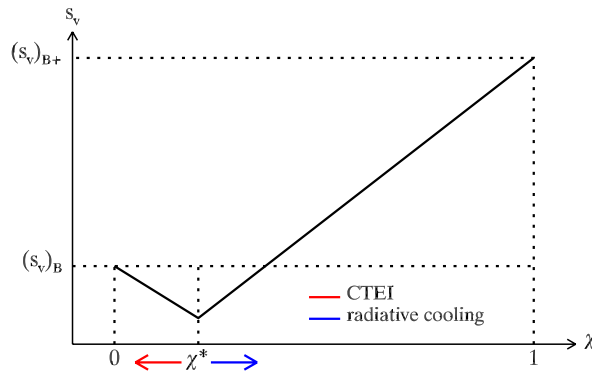
Figure 6.1   Schematic diagram of the hypothesized interactions between CTEI and radiative cooling for the saturation mixing fraction. The black line is the mixing line. The red and blue arrows are tendencies forced by each process. CTEI forces the kink toward the smaller saturation mixing fraction and weaker negative buoyancy, and radiative cooling tries to keep the position of the kink. As a result, the average inversion value is steady.

6.2.   Simulations

Four additional simulations based on DYCOMS-II FP1 were performed to test the hypothesis. Four modifications to disturb the steady saturation mixing fraction were introduced. There are at least two ways to modify either evaporative or radiative cooling. One way is increasing or decreasing the physical constant of the latent heat of condensation. Increasing the constant is expected to strengthen CTEI, and vice versa. Another way is modification of the radiative heating rate. Stronger radiative cooling

dominates, and leads to a faster circulation and more cloud water. These modifications are artificial, so the interpretation has to be done with care.

All four simulations ran for a four-hour duration and used the FP1 configuration, except during the third hour. During the third hour, LCND+ increased the latent heat of condensation by 20%, while LCND- decreased it by 20%, and RAD- decreased the radiative heating rate by 10% while RAD+ increased it by 10%. These modifications were only applied for the third hour.

As shown in Figure 6.2, each case forced CTEI to be either weaker (CTEI-) or stronger (CTEI+) as measured by the Randall-Deardorff criterion, which is shown in Figure 6.7. LCND+ and RAD- represent the red arrow in Figure 6.1, and LCND- and RAD+ represent the blue arrow. These changes turned out to be moderate enough so that model ran stably, but large enough so that the result differs noticeably from FP1. For the following discussions, CTEI+ denotes the two runs of LCND+ and RAD-, and CTEI- denotes the remaining two runs, i.e., LCND- and RAD+.
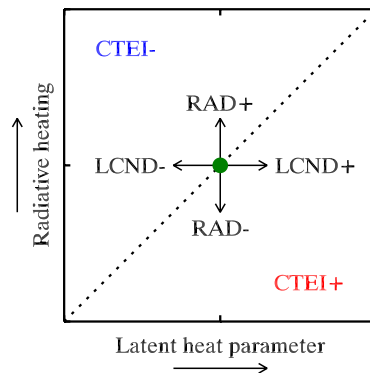
Figure 6.2   The direction of the perturbation for the four simulations. The green dot represents FP1.

6.3.   Results

The time series of the cloud water mixing ratio for each case as well as FP1 is shown in Figure 6.3. The CTEI+ runs reduce the cloud water amount, and the CTEI- runs increase it compared with FP1. Those changes are abrupt. Modification of the radiative heating indirectly changes the cloud water amount through temperature changes while modification of the latent heat constant directly changes it in the model microphysics. This should be the reason why the LCND cases have very sharp changes at 120 and 180 minutes.
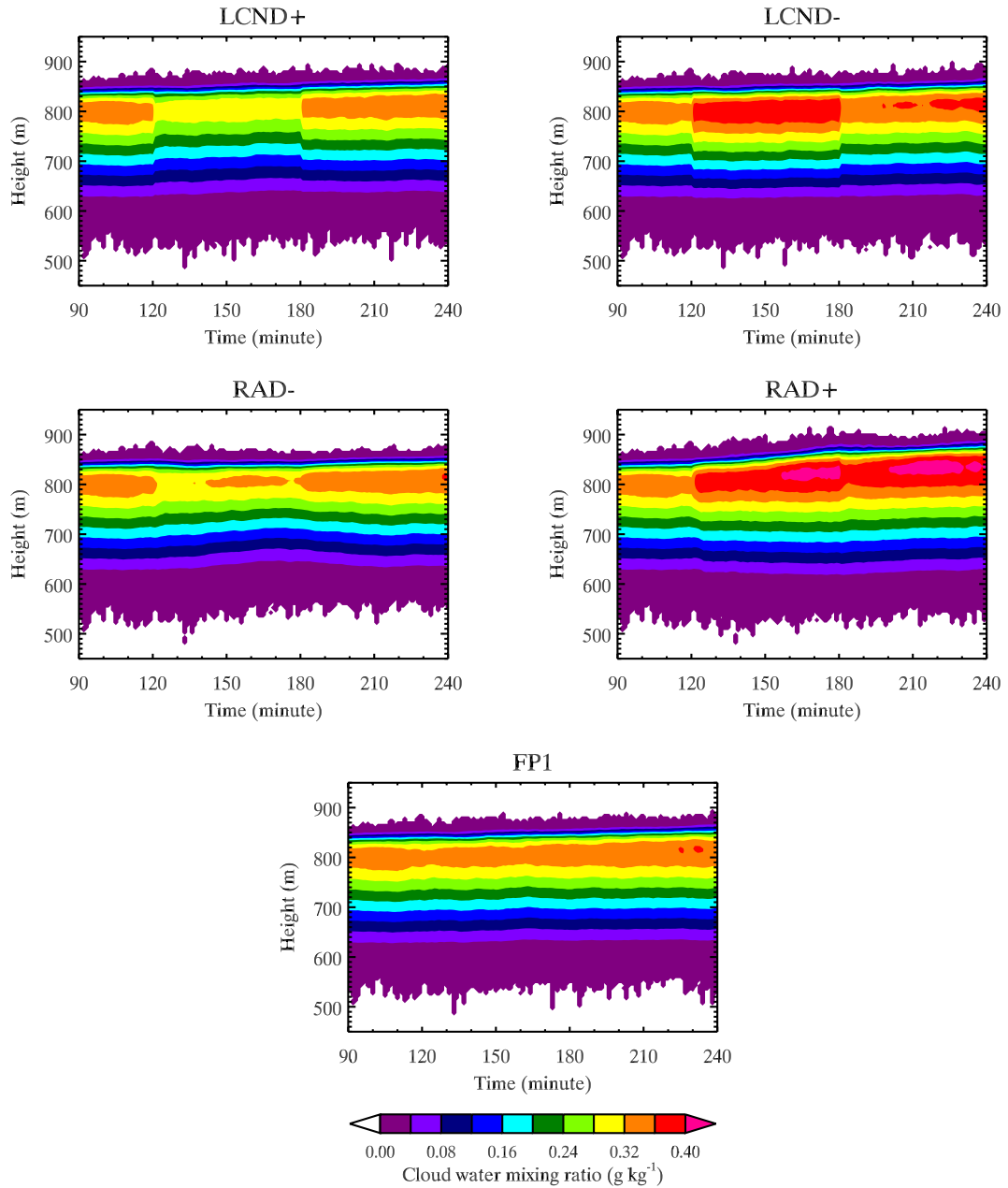
Figure 6.3   Time series of the cloud water mixing ratio.

The cloud amount decreases for the CTEI+ cases and increases for the CTEI-cases. The time series of the cloud fraction subtracted of FP1 is shown in Figure 6.4a. The CTEI+ runs raise the cloud base. As seen in BR-73 simulations, cloud thinning due to CTEI takes place from the cloud base. LCND+ increases the small amount at the cloud top, while RAD- reduces the cloud at the cloud top. The CTEI- runs increase the cloud

amount at the cloud base, especially RAD+. LCND- reduces it at the cloud top, while

RAD+ significantly increases it at the cloud top. Compared with FP1 (Figure 6.4b), the

cloud base is relatively higher for CTEI+ and lower for CTEI-, and the cloud top is

similar for LCND+, lower for LCND- and RAD- and higher for RAD+. The entrainment

rate shown later agrees with these.
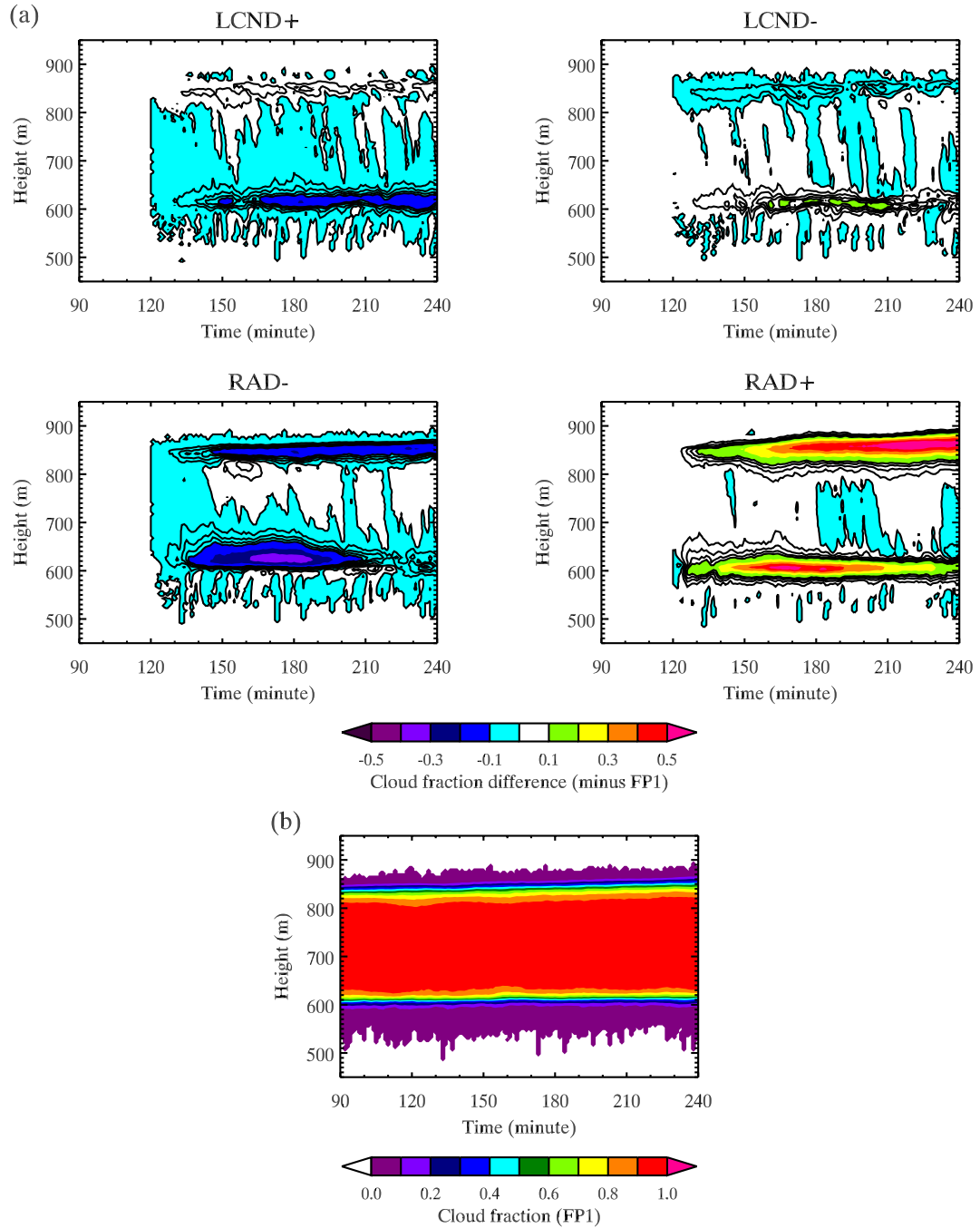
Figure 6.4   (a) The time series of the cloud fraction difference, which is the subtraction of the cloud fraction of FP1. The contour lines are between -0.1 and 0.1 every 0.025 for visual aid. (b) Time series of the cloud fraction of FP1 for reference.

The time series of the maximum radiative cooling rate, which locates around the cloud top, is shown in Figure 6.5. The radiative cooling becomes weaker for CTEI+ and stronger for CTEI-. Radiative cooling is indirectly modified for the LCND cases through

change of cloud water amount, while the RAD cases are directly forced by the configuration during the third hour.
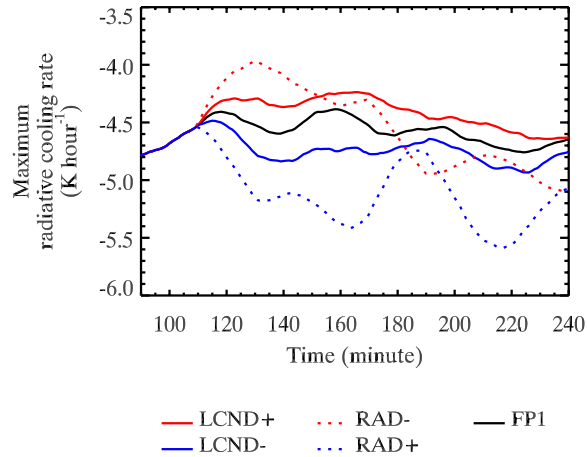
Figure 6.5   Time series of the maximum radiative cooling rate. A 20-minute running mean was used for smoothing.

The net evaporation rate shows significant impact for the RAD runs (Figure 6.6). During the third hour, the net evaporation around the cloud top for RAD- becomes thicker, while RAD+ has large net condensation just below the evaporation at the cloud top. The small amount of net evaporation in the mid-cloud layer, i.e., the 700 m level, becomes more frequent and thicker for CTEI-, while CTEI+ eliminates this evaporation.
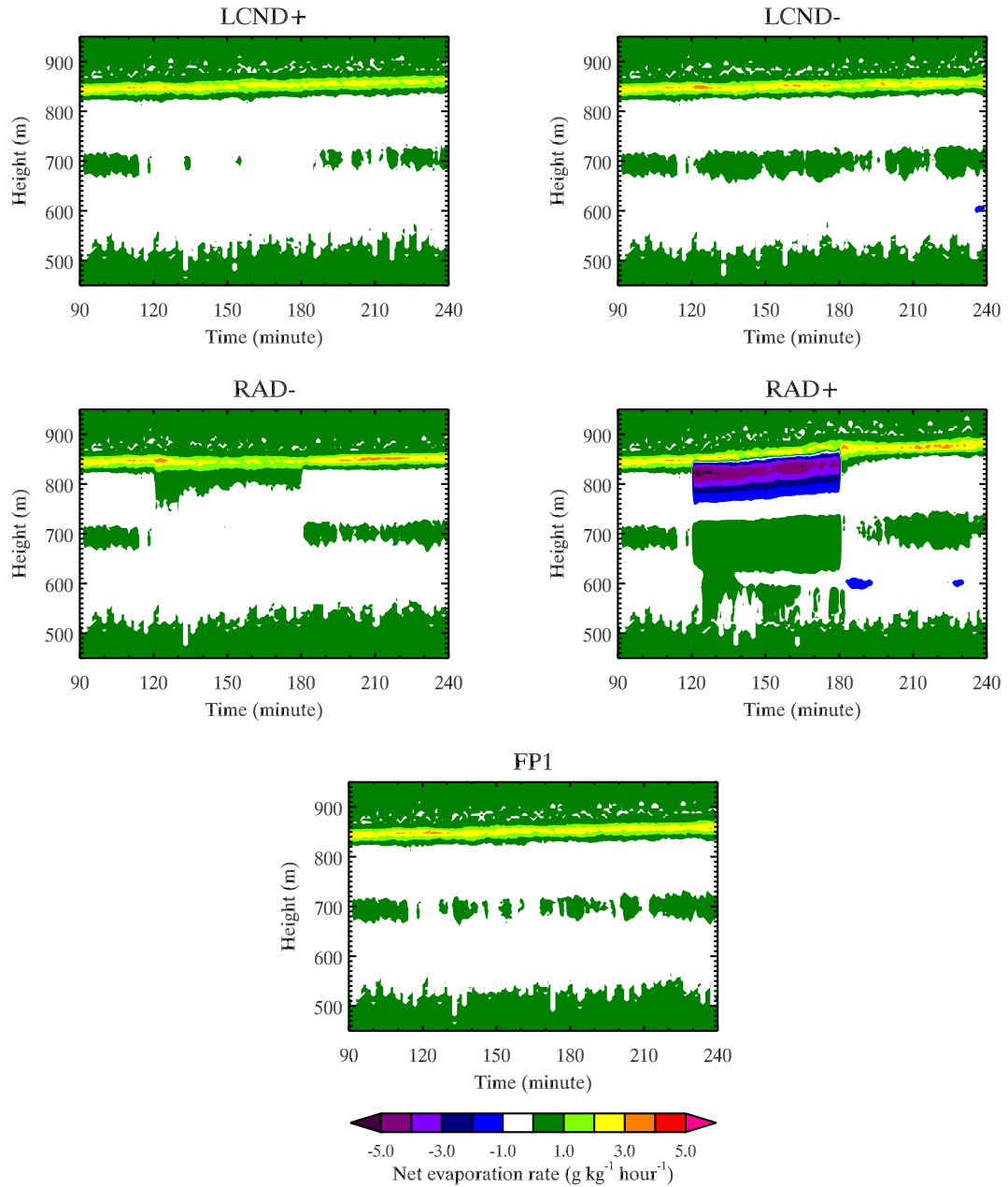
Figure 6.6   Time series of the net evaporation rate.

The time series of the saturation mixing fraction and other variables are shown in Figure 6.7. The modification shifts the saturation mixing fraction to either smaller or larger as the anticipated direction by the proposed interaction. The change for RAD- looks dramatic but the magnitude of the increase is only 0.01. Maximum negative buoyancy and the CTEI criterion parameter have a large change for the LCND runs due

to the modification of the latent heat parameter. The stability parameter does not change a great deal for the RAD runs, and the maximum negative buoyancy is larger for RAD+ than RAD- due to its large saturation mixing fraction. Refer to the definition of the maximum negative buoyancy and stability parameter at equations (4.6) and (4.7). The cloud water path quickly adjusts to a new state during the third hour, and backs to near FP1 except RAD+, which may find another state in the fourth hour. The cloud water path is in a declining trend for CTEI+ while CTEI- is in the increasing. These trends are especially clear for the RAD cases. Changes of the turbulence strength are large for the RAD cases. The RAD- run weakens the turbulence while the RAD+ run strengthens it. As the author discussed concerning the cloud fraction difference in Figure 6.4, the entrainment rate increases for LCND+ and RAD+, and decreases for LCND- and RAD-.
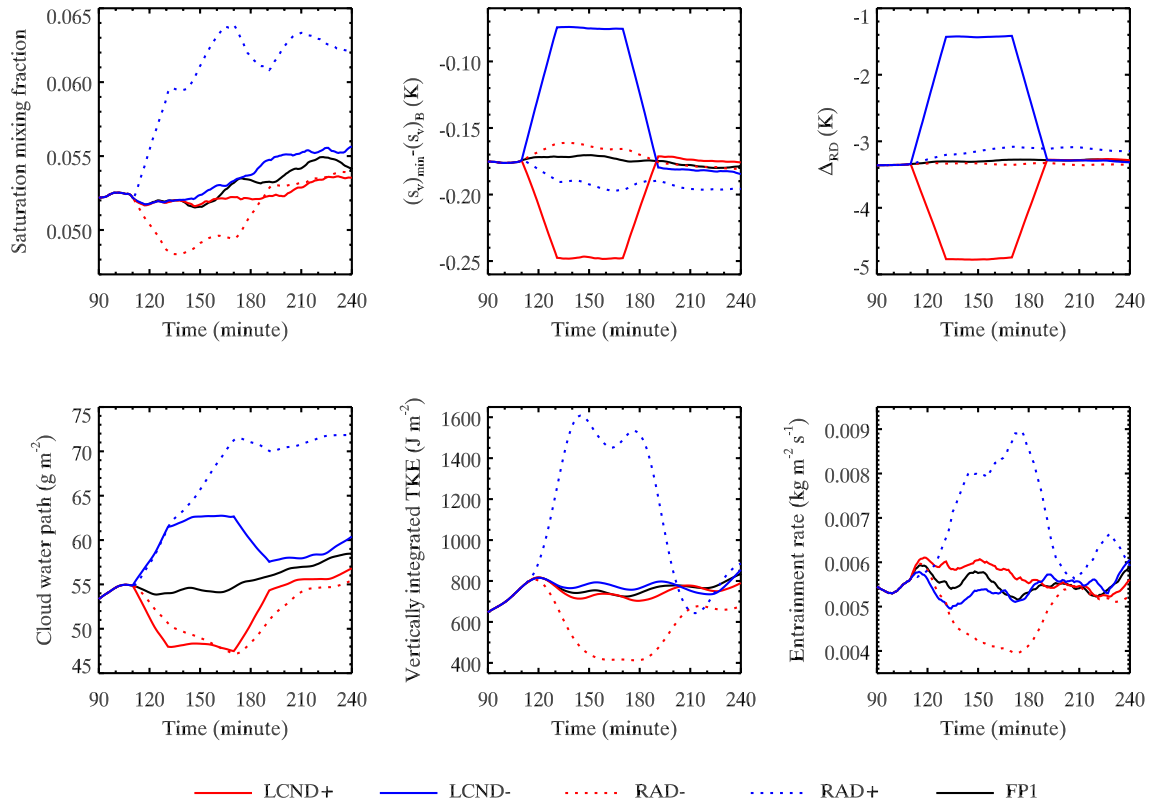
Figure 6.7   Time series for one-dimensional parameters. All parameters are smoothed with a 20-minute running mean. The modified value of the latent heat constant was used for the LCND runs.

All four runs return to their bulk TKE and entrainment rate close to FP1 in the fourth hour. The large change of the bulk TKE and entrainment rate in the third hour due to the modification for radiative heating was unexpected. The response in the fourth hour may be the negative radiative cooling feedback suggested by Moeng et al. (1995). At fourth hour, the stronger turbulence of RAD+ should be slowed down so that parcels can be exposed to longer cooling, while for the weaker turbulence of RAD-, parcels are exposed to longer cooling so that the turbulence becomes faster. If we assume that CTEI is hidden, then the proposed interaction for the steady saturation mixing fraction occurs in such a way that the steady saturation mixing fraction is the point where the radiative cooling lets CTEI work. Whichever CTEI is hidden, or whatever CTEI does, turbulence

is quickly adjusted appropriately through negative radiative cooling feedback for longer cloud life. Under such a condition, a runaway cloud-breakup scenario will not be observed for MSCs.

Chapter 7.   Summary and Conclusions

We developed a LPTM to gain further understanding of the physics of cloud-top entrainment. Preceding the LPTM development, the scalar advection scheme of the host model was revisited since the accuracy of the parcel's scalar value partly depends on the scalar advection scheme. The ULTIMATE-MACHO scheme became monotonic with the three-dimensional FCT. The fifth-order ULTIMATE-MACHO showed significantly superior results compared to the lower-order schemes. The results for fifth- and seventh-order ULTIMATE-MACHO schemes were comparable, and the improvement was minor with respect to the additional numerical cost. The impact of the fifth-order ULTIMATE-MACHO to a simulated turbulence fields was studied with GCSS DYCOMS-II runs. The fifth-order scheme better maintained mixed layer profiles and a thicker cloud layer than the original second order scheme. The entrainment rates were smaller for higher order schemes.

LPTM was evaluated from various perspectives with three- and two-dimensional GCSS DYCOMS-II simulations. As expected, the Lagrangian mean profile was closely overlapped with the Eulerian mean profile. The individual parcel path follows the theoretical path. The Lagrangian budget equation generally was not established for turbulence with desired accuracy. We hypothesized that in order to establish the budget, the grid spacing has to be equivalent to the scale of molecular viscosity, so that the field is smooth and no longer fractal. This would be "direct numerical simulation" (DNS).

Two high-resolution LESs were performed with the grid spacing of O(5 m): one for buoyancy reversal, and the other for realistic MSC. The power spectra for these simulations were well matched with the energy cascade slope. The buoyancy reversal simulation converged for grid spacing smaller than 10 m in the horizontal and 5 m in the vertical. The mixing line showed active buoyancy reversal and CTEI. The DYCOMS-II simulation used the RRTM code for radiative flux calculations. A 10-second update periods was required for 35 m horizontal grid spacing to minimize the bias for the correlation of the parameters in the inversion. For 5 m horizontal grid spacing, the result suggested a 1.25-second update. Comparison with the low-resolution runs suggested that the resolution has to be refined in the horizontal as well as the vertical to better represent entrainment and microphysical processes.

A SAM-LPTM simulation for the high resolution DYCOMS-II was analyzed with the geographical location and mixing fraction diagram. Cloud-top entrainment is favored to take place around the cloud holes, where the air is relatively dry and downdraft. By following the cloud-top horizontal diverging motion, the parcel moves horizontally toward the entrainment region. Meanwhile, the radiative, evaporative and mixing processes cool and moisten the parcel. The mixing fraction analysis showed that the largest contribution for the buoyancy reduction is the cooling due to the turbulent mixing, and the radiative and evaporative cooling are equally strong. These results disagree with the previous studies such as SR97 and VD02. These disagreements come from the different diagnostic method for the mixing fraction since the result similar to the previous studies was replicated with LPTM. We encountered an artificial radiative warming around $\chi = 1$ with the traditional approach. This problem was circumvented by the direct

use of the time integrated radiative cooling rate for each parcel, which is only obtained with the Lagrangian tracking method. The mixing fraction analysis also showed that buoyancy reversal occurs on parcels. The parcel's parameters such as virtual dry static energy, evaporative heating, and mixing, tend to overlap the corresponding theoretically derived mixing line.

The interactions between the radiative cooling and CTEI in terms of the saturation mixing fraction was proposed such that radiative cooling forces the saturation mixing fraction toward larger values, and CTEI forces it in the opposite direction if CTEI is hidden. Numerical tests showed the existence of the interaction if one assumes hidden CTEI. More importantly, the results suggest rapid turbulence adjustment through the negative radiative cooling feedback. This negative feedback is so strong that CTEI does not affect turbulence and cloud life. Under such conditions, cloud breakup due to CTEI is impossible.

What is unknown is whether CTEI takes place for the entrained parcels. A method to detect CTEI has to be developed. As YR08 suggested, the entrainment due to CTEI is spontaneous. Thus, if CTEI is proved to occur for MSCs, it has to be included in cloud-top entrainment parameterization.

The importance of the shear instability was not evaluated in this research. A case with strong shear at the PBL top is required. The importance of the drizzle was not studied in this research, either.

LPTM could be applied to study the detrained cloudy air. These parcels may contribute to the conditioning of the entrainment since some of the entrained parcels obtain a small mixing fraction in the upper inversion layer. LPTM also can be used as an

observation flight simulator so that the analysis developed for observational data is applied and tested.

The present study limited the simulation domain size for small grid spacing. The effect of CTEI on the mesoscale organization has not been studied with LES, yet.

The convergence for the simulated fields of DYCOMS-II FPH should be examined. Lastly, the selective flux limiter approach should be studied to improve ULTIMATE-MACHO.

Appendix A.　　List of Variables

Tables A1 and A2 list basic variables and physical constants, which are used to define thermodynamic variables listed in Table A3.

Potential temperature, dry static energy and water vapor mixing ratio are dry conservative variables. Liquid water potential temperature, moist static energy, liquid water static energy, and total water mixing ratio are moist conservative variables. Virtual dry static energy is often used as a measure of buoyancy. Virtual potential temperature is used instead of virtual dry static energy for some studies.

Table A1　　List of basic variables.

name	symbol	unit	note
height	z	m	
pressure	p	hPa	
temperature	T	K	
water vapor mixing ratio	q		Unit is frequently converted to g kg^{-1} by multiplying by 10^3.
cloud water mixing ratio	l	kg kg^{-1}	
saturation mixing ratio	$q*$		

Table A2　　List of constants.

name	symbol	unit
gas constant for dry air	R_d	
gas constant for water vapor	R_v	J K^{-1} kg^{-1}
specific heat of dry air at constant pressure	c_p	
latent heat of condensation	L	J kg^{-1}
gravitational acceleration	g	m s^{-2}

Table A3   List of thermodynamic variables.

name	definition	unit	note
virtual temperature	$T_v = T(1 + \delta q - l)$	K	$\delta = (R_v - R_d)/R_d$
potential temperature	$\theta = T\left(\dfrac{p_0}{p}\right)^\kappa$		p_0 is reference pressure. $\kappa = R_d/c_p$
liquid water potential temperature	$\theta_l = \theta - \dfrac{L}{c_p}l$		
virtual potential temperature	$\theta_v = \theta(1 + \delta q - l)$		
dry static energy	$s = c_p T + gz$	J kg^{-1}	Unit is frequently converted to K by dividing by c_p.
moist static energy	$h = s + Lq$		
liquid water static energy	$s_l = s - Ll$		
virtual dry static energy	$s_v = c_p T_v + gz$		
total water mixing ratio	$r = q + l$	kg kg^{-1}	Unit is frequently converted to g kg^{-1} by multiplying by 10^3.

Appendix B.   ULTIMATE Scheme

In this appendix, we derive the ULTIMATE formula for non-uniform grids up to fifth order, and compared it to its uniform-grid formula with a simple one-dimensional advection test.

The ULTIMATE scheme is constructed in the following manner. Assume that the grid is uniform and the velocity is constant. For a grid box, x_i, the updated value of the scalar, ϕ_i, is the upstream value at $x_i - u\Delta t$, that is,

$$\phi_i^{n+1} = \phi^n\left(x_i - u\Delta t\right). \tag{B1}$$

Formulate the upstream value with Lagrange interpolation, then equate it as

$$\phi^n\left(x_i - u\Delta t\right) = \phi_i^n + c\left(\hat{\phi}_i - \hat{\phi}_{i+1}\right), \tag{B2}$$

where $\hat{\phi}_i$ is the left-side face value of the grid box, and $c = \dfrac{u\Delta t}{\Delta x}$ is the Courant number.

Further manipulation produces the following formulas up to the seventh order:

$$
\begin{cases}
\hat{\phi}_i^{1st} = \frac{1}{2}\left(\phi_i + \phi_{i-1}\right) - \text{sgn}\left(c\right)\left(\phi_i - \phi_{i-1}\right), \\[2mm]
\hat{\phi}_i^{2nd} = \frac{1}{2}\left(\phi_i + \phi_{i-1}\right) - \frac{c}{2}\left(\phi_i - \phi_{i-1}\right), \\[2mm]
\hat{\phi}_i^{3rd} = \hat{\phi}_i^{2nd} + \frac{c^2-1}{12}\left[\left(\phi_{i+1} - \phi_i - \phi_{i-1} + \phi_{i-2}\right) - \text{sgn}\left(c\right)\left(\phi_{i+1} - 3\phi_i + 3\phi_{i-1} - \phi_{i-2}\right)\right], \\[2mm]
\hat{\phi}_i^{4th} = \hat{\phi}_i^{2nd} + \frac{c^2-1}{12}\left[\left(\phi_{i+1} - \phi_i - \phi_{i-1} + \phi_{i-2}\right) - \frac{c}{2}\left(\phi_{i+1} - 3\phi_i + 3\phi_{i-1} - \phi_{i-2}\right)\right], \\[2mm]
\hat{\phi}_i^{5th} = \hat{\phi}_i^{4th} + \frac{1}{240}\left(c^2-1\right)\left(c^2-4\right)\left[\left(\phi_{i+2} - 3\phi_{i+1} + 2\phi_i + 2\phi_{i-1} - 3\phi_{i-2} + \phi_{i-3}\right)\right. \\[1mm]
\qquad \left. - \text{sgn}\left(c\right)\left(\phi_{i+2} - 5\phi_{i+1} + 10\phi_i - 10\phi_{i-1} + 5\phi_{i-2} - \phi_{i-3}\right)\right], \\[2mm]
\hat{\phi}_i^{6th} = \hat{\phi}_i^{4th} + \frac{1}{240}\left(c^2-1\right)\left(c^2-4\right)\left[\left(\phi_{i+2} - 3\phi_{i+1} + 2\phi_i + 2\phi_{i-1} - 3\phi_{i-2} + \phi_{i-3}\right)\right. \\[1mm]
\qquad \left. - \frac{c}{3}\left(\phi_{i+2} - 5\phi_{i+1} + 10\phi_i - 10\phi_{i-1} + 5\phi_{i-2} - \phi_{i-3}\right)\right], \text{ and} \\[2mm]
\hat{\phi}_i^{7th} = \hat{\phi}_i^{6th} + \frac{1}{10080}\left(c^2-1\right)\left(c^2-4\right)\left(c^2-9\right) \\[1mm]
\qquad \left[\left(\phi_{i+3} - 5\phi_{i+2} + 9\phi_{i+1} - 5\phi_i - 5\phi_{i-1} + 9\phi_{i-2} - 5\phi_{i-3} + \phi_{i-3}\right)\right. \\[1mm]
\qquad \left. - \text{sgn}\left(c\right)\left(\phi_{i+3} - 7\phi_{i+2} + 21\phi_{i+1} - 35\phi_i + 35\phi_{i-1} - 21\phi_{i-2} + 7\phi_{i-3} - 1\phi_{i-3}\right)\right].
\end{cases}
\tag{B3}
$$

Leonard (1991) derived a general n-th order formula. The above formula is assumed to be valid for varying velocity.

To construct the formula for a non-uniform grid, denote Δx_i as the space between left and right faces of ϕ_i, and $\Delta \hat{x}_i$ as the space between ϕ_{i-1} and ϕ_i. Velocity is constant as assumed for a uniform grid, then the Courant number can be written as $c_i = \dfrac{u\Delta t}{\Delta x_i}$. For this Courant number, the flux form update equation is written as

$$
\phi_i^{n+1} = \phi_i^n + c_i\hat{\phi}_i - \left(\frac{\Delta x_{i+1}}{\Delta x_i}\right)c_{i+1}\hat{\phi}_{i+1}.
\tag{B4}
$$

Substitute $C = \dfrac{u\Delta t}{\Delta X}$ into c in (B3) except $\mathrm{sgn}(c)$, which should be changed to

$\mathrm{sgn}(c_i)$. Manipulate the resulting equation, and find an appropriate space, ΔX, so that the

resulting formula converges to the formula in (B3) for a uniform grid. The first-order

formula is the same as the uniform grid formula:

$$\hat{\phi}_i^{1\mathrm{st}} = \frac{1}{2}\left(\phi_i + \phi_{i-1}\right) - \mathrm{sgn}(c_i)\left(\phi_i - \phi_{i-1}\right). \tag{B5}$$

The second-order formula is found straightforwardly as

$$\hat{\phi}_i^{2\mathrm{nd}} = \frac{1}{2}\left(\phi_i + \phi_{i-1}\right) - \frac{c_i}{2}\left(\frac{\Delta x_i}{\Delta \hat{x}_i}\right)\left(\phi_i - \phi_{i-1}\right). \tag{B6}$$

The third-order formula can be written as

$$\hat{\phi}_i^{3\mathrm{rd}} = \hat{\phi}_i^{2\mathrm{nd}} + \frac{1}{2}\left[\left(\hat{\Phi}_i^{3\mathrm{rd}+} + \hat{\Phi}_i^{3\mathrm{rd}-}\right) - \mathrm{sgn}(c_i)\left(\hat{\Phi}_i^{3\mathrm{rd}+} - \hat{\Phi}_i^{3\mathrm{rd}-}\right)\right], \tag{B7}$$

where

$$\begin{cases} \hat{\Phi}_i^{3\mathrm{rd}+} = \dfrac{C^2 - 1}{6}\left(\phi_i - 2\phi_{i-1} + \phi_{i-2}\right) \\[4mm] \hat{\Phi}_i^{3\mathrm{rd}-} = \dfrac{C^2 - 1}{6}\left(\phi_{i+1} - 2\phi_i + \phi_{i-1}\right) \end{cases}. \tag{B8}$$

Manipulate the $\hat{\Phi}_i^{3\mathrm{rd}+}$ equation as

96

$$\hat{\Phi}_i^{3rd+} = \frac{C^2-1}{6}\left(\phi_i - 2\phi_{i-1} + \phi_{i-2}\right)$$

$$= \frac{1}{6}\left[\left(\frac{u\Delta t}{\Delta X}\right)^2 - 1\right]\left[\left(\phi_i - \phi_{i-1}\right) - \left(\phi_{i-1} - \phi_{i-2}\right)\right]$$

$$= \frac{1}{6}\left[\left(u\Delta t\right)^2 - \Delta X^2\right]\left(\frac{1}{\Delta X^2}\right)\left[\left(\phi_i - \phi_{i-1}\right) - \left(\phi_{i-1} - \phi_{i-2}\right)\right]$$

$$= \frac{1}{6}\left[\left(u\Delta t\right)^2 - \Delta X^2\right]\left[\frac{1}{\Delta x_{i-1}}\left(\frac{\phi_i - \phi_{i-1}}{\Delta \hat{x}_i} - \frac{\phi_{i-1} - \phi_{i-2}}{\Delta \hat{x}_{i-1}}\right)\right]$$

$$= \frac{1}{6}\left[\left(u\Delta t\right)^2 - \Delta X^2\right]\left\{\frac{1}{\Delta \hat{x}_i \Delta \hat{x}_{i-1}}\left[\frac{\Delta \hat{x}_{i-1}}{\Delta x_{i-1}}\left(\phi_i - \phi_{i-1}\right) - \frac{\Delta \hat{x}_i}{\Delta x_{i-1}}\left(\phi_{i-1} - \phi_{i-2}\right)\right]\right\}$$

$$= \frac{1}{6}\left[\frac{\left(u\Delta t\right)^2}{\Delta \hat{x}_i \Delta \hat{x}_{i-1}} - 1\right]\left[\frac{\Delta \hat{x}_{i-1}}{\Delta x_{i-1}}\left(\phi_i - \phi_{i-1}\right) - \frac{\Delta \hat{x}_i}{\Delta x_{i-1}}\left(\phi_{i-1} - \phi_{i-2}\right)\right]$$

$$\therefore \hat{\Phi}_i^{3rd+} = \frac{1}{6}\left(c_i^2 \frac{\Delta x_i^2}{\Delta \hat{x}_i \Delta \hat{x}_{i-1}} - 1\right)\left[\frac{\Delta \hat{x}_{i-1}}{\Delta x_{i-1}}\left(\phi_i - \phi_{i-1}\right) - \frac{\Delta \hat{x}_i}{\Delta x_{i-1}}\left(\phi_{i-1} - \phi_{i-2}\right)\right]. \tag{B9}$$

The same manipulation for the $\hat{\Phi}_i^{3rd-}$ equation is reduced to

$$\hat{\Phi}_i^{3rd-} = \frac{1}{6}\left(c_i^2 \frac{\Delta x_i^2}{\Delta \hat{x}_{i+1} \Delta \hat{x}_i} - 1\right)\left[\frac{\Delta \hat{x}_i}{\Delta x_i}\left(\phi_{i+1} - \phi_i\right) - \frac{\Delta \hat{x}_{i+1}}{\Delta x_i}\left(\phi_i - \phi_{i-1}\right)\right]. \tag{B10}$$

The fourth-order formula can be written as

$$\hat{\phi}_i^{4th} = \hat{\phi}_i^{2nd} + \hat{\Phi}_i^{3rd} + \hat{\Phi}_i^{4th}, \tag{B11}$$

where

$$\begin{cases} \hat{\Phi}_i^{3rd} = \dfrac{C^2-1}{12}\left(\phi_{i+1} - \phi_i - \phi_{i-1} + \phi_{i-2}\right) \\[2mm] \hat{\Phi}_i^{4th} = -\dfrac{\left(C^2-1\right)C}{24}\left(\phi_{i+1} - 3\phi_i + 3\phi_{i-1} - \phi_{i-2}\right) \end{cases}. \tag{B12}$$

Manipulation yields

$$
\begin{cases}
\hat{\Phi}_i^{3\mathrm{rd}} = \dfrac{1}{6}\left(c_i^2\,\dfrac{\Delta x_i^2}{\Delta\hat{x}_{i+1}\Delta\hat{x}_{i-1}} - 1\right)\left[\dfrac{\Delta\hat{x}_{i-1}}{\Delta x_i + \Delta x_{i-1}}\left(\phi_{i+1} - \phi_i\right) - \dfrac{\Delta\hat{x}_{i+1}}{\Delta x_i + \Delta x_{i-1}}\left(\phi_{i-1} - \phi_{i-2}\right)\right] \\[3mm]
\hat{\Phi}_i^{4\mathrm{th}} = -\dfrac{1}{24}\left(c_i^2\,\dfrac{\Delta x_i^2}{\Delta\hat{x}_{i+1}\Delta\hat{x}_{i-1}} - 1\right)c_i\,\dfrac{\Delta x_i}{\Delta\hat{x}_i}\left[\dfrac{\Delta\hat{x}_{i-1}}{\Delta x_i}\left(\phi_{i+1} - \phi_i\right)\right. \\[3mm]
\qquad\qquad \left. -\dfrac{\Delta\hat{x}_{i+1}\Delta\hat{x}_{i-1}\left(\Delta x_{i-1} + \Delta x_i\right)}{\Delta\hat{x}_i\Delta x_i\Delta x_{i-1}}\left(\phi_i - \phi_{i-1}\right) + \dfrac{\Delta\hat{x}_{i+1}}{\Delta x_{i-1}}\left(\phi_{i-1} - \phi_{i-2}\right)\right]
\end{cases}
\quad . \quad \text{(B13)}
$$

After manipulation, the fifth-order formula can be written as

$$
\hat{\phi}_i^{5\mathrm{th}} = \hat{\phi}_i^{4\mathrm{th}} + \frac{1}{2}\left[\left(\hat{\Phi}_i^{5\mathrm{th}+} + \hat{\Phi}_i^{5\mathrm{th}-}\right) - \mathrm{sgn}(c)\left(\hat{\Phi}_i^{5\mathrm{th}+} - \hat{\Phi}_i^{5\mathrm{th}-}\right)\right],
\qquad \text{(B14)}
$$

where

$$
\begin{cases}
\hat{\Phi}_i^{5\mathrm{th}+} = \dfrac{1}{120}\left(c_i^2\,\dfrac{\Delta x_i^2}{\Delta\hat{x}_i\Delta\hat{x}_{i-1}} - 1\right)\left(c^2\,\dfrac{\Delta x_i^2}{\Delta\hat{x}_{i+1}\Delta\hat{x}_{i-2}} - 4\right) \\[3mm]
\left[\dfrac{\Delta\hat{x}_{i-1}\Delta\hat{x}_{i-2}}{\Delta x_i\Delta x_{i-1}}\left(\phi_{i+1} - \phi_i\right) - \dfrac{\Delta\hat{x}_{i+1}\Delta\hat{x}_{i-2}\left(\Delta\hat{x}_{i-1}\Delta x_{i-1} + \Delta\hat{x}_{i-1}\Delta x_i + \Delta\hat{x}_i\Delta x_i\right)}{\Delta\hat{x}_i\Delta x_i\Delta x_{i-1}\Delta x_{i-1}}\left(\phi_i - \phi_{i-1}\right)\right. \\[3mm]
\left. +\dfrac{\Delta\hat{x}_{i+1}\Delta\hat{x}_{i-2}\left(\Delta\hat{x}_{i-1}\Delta x_{i-2} + \Delta\hat{x}_i\Delta x_{i-2} + \Delta\hat{x}_i\Delta x_{i-1}\right)}{\Delta\hat{x}_{i-1}\Delta x_{i-1}\Delta x_{i-1}\Delta x_{i-2}}\left(\phi_{i-1} - \phi_{i-2}\right) \right. \\[3mm]
\left. -\dfrac{\Delta\hat{x}_{i+1}\Delta\hat{x}_i}{\Delta x_{i-1}\Delta x_{i-2}}\left(\phi_{i-2} - \phi_{i-3}\right)\right] \\[3mm]
\hat{\Phi}_i^{5\mathrm{th}-} = \dfrac{1}{120}\left(c_i^2\,\dfrac{\Delta x_i^2}{\Delta\hat{x}_{i+1}\Delta\hat{x}_i} - 1\right)\left(c_i\,\dfrac{\Delta x_i^2}{\Delta\hat{x}_{i+2}\Delta\hat{x}_{i-1}} - 4\right) \\[3mm]
\left[\dfrac{\Delta\hat{x}_i\Delta\hat{x}_{i-1}}{\Delta x_{i+1}\Delta x_i}\left(\phi_{i+2} - \phi_{i+1}\right) - \dfrac{\Delta\hat{x}_{i+2}\Delta\hat{x}_{i-1}\left(\Delta\hat{x}_i\Delta x_i + \Delta\hat{x}_i\Delta x_{i+1} + \Delta\hat{x}_{i+1}\Delta x_{i+1}\right)}{\Delta\hat{x}_{i+1}\Delta x_{i+1}\Delta x_i\Delta x_i}\left(\phi_{i+1} - \phi_i\right)\right. \\[3mm]
\left. +\dfrac{\Delta\hat{x}_{i+2}\Delta\hat{x}_{i-1}\left(\Delta\hat{x}_i\Delta x_{i-1} + \Delta\hat{x}_{i+1}\Delta x_{i-1} + \Delta\hat{x}_{i+1}\Delta x_i\right)}{\Delta\hat{x}_i\Delta x_i\Delta x_i\Delta x_{i-1}}\left(\phi_i - \phi_{i-1}\right) \right. \\[3mm]
\left. -\dfrac{\Delta\hat{x}_{i+2}\Delta\hat{x}_{i+1}}{\Delta x_i\Delta x_{i-1}}\left(\phi_{i-1} - \phi_{i-2}\right)\right]
\end{cases}
\quad . \quad \text{(B15)}
$$

We followed the one-dimensional advection test of Leonard et al. (1995). The domain width is 150, and there are 150 discrete points with the periodic boundary. The initial scalar profile consists of five different shapes: rectangular box, sine-squared, semi-ellipse, triangle, and Gaussian. The initial profile is specified as

$$\phi_i(x_i) = \begin{cases} 0 & \text{for } 0 \le x_i \le 5 \\ 1 & \text{for } 5 < x_i \le 25 \quad \text{(rectangular box)} \\ 0 & \text{for } 25 < x_i \le 35 \\ \sin^2\left[\dfrac{\pi}{20}(x_i - 35)\right] & \text{for } 35 < x_i \le 55 \quad \text{(sine-squared)} \\ 0 & \text{for } 55 < x_i \le 65 \\ \sqrt{1 - \left[0.1(x_i - 75)\right]^2} & \text{for } 65 < x_i \le 85 \quad \text{(semi-ellipse)} \\ 0 & \text{for } 85 < x_i \le 95 \\ 0.1(x_i - 95) & \text{for } 95 < x_i \le 105 \quad \text{(triangle)} \\ 1 - 0.1(x_i - 105) & \text{for } 105 < x_i \le 115 \\ \exp\left[-\dfrac{1}{2\sigma^2}(x_i - 135)^2\right] & \text{for } 115 < x_i \le 150 \quad \text{(Gaussian)} \end{cases} . \quad \text{(B16)}$$

The standard deviation for the Gaussian profile is specified as $\sigma = 2.5$.

The result for the fifth-order formula for uniform grid with 0.6 constant Courant number is shown in Figure 2.1.

A comparison study between formulas for non-uniform and uniform grids was performed. First, a non-uniform grid was constructed as follows. The space between scalar points is defined as

$$\Delta \hat{x}_i = \begin{cases} 1 & \text{for } 1 \le i \le 10 \\ 1 + 0.9\sin\left[\dfrac{2\pi}{130}(i - 10)\right] & \text{for } 11 \le i \le 140 \\ 1 & \text{for } 141 \le i \le 150 \end{cases} . \quad \text{(B17)}$$

With $x_1 = 0.5$, the scalar points are obtained by $x_i = x_{i-1} + \Delta \hat{x}_{i-1}$. The space between the face points is defined as

$$\Delta x_i \equiv 0.5\left(x_{i+1} - x_{i-1}\right), \tag{B18}$$

so that the face point is the mid point of scalar points. The face points are set with $\hat{x}_1 = 0$. The Courant number for the smallest grid spacing was set at 0.6, and the Courant number for the other face points were scaled so that $u\Delta t$ was constant. The same $u\Delta t$ was used for the uniform grid case for comparison.

The result after one rotation for the fifth-order formula for non-uniform and uniform grids is shown in Figure B1. The non-uniform grid formula suffers for the Gaussian shape and sharp peaks so that numerical diffusion is large at these places. The result of the non-uniform grid formula resembles the result of the third-order uniform grid formula (not shown).
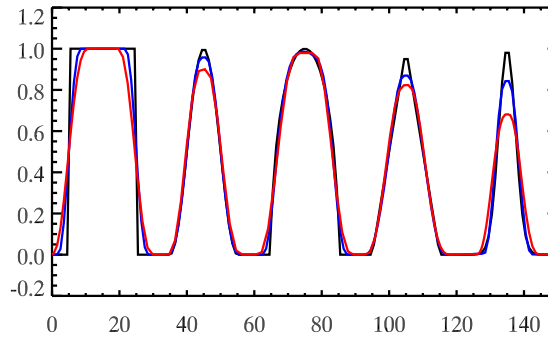
Figure B1   The result of the one-dimensional advection test for the fifth-order formula for non-uniform (red) and uniform (blue) grid. The initial profile is shown as black line.

Appendix C.   Diagnostic Method for Determining the Entrainment Rate

YR08 formulated an entrainment rate based on the relaxed form of the inversion-layer budget equations of the mixed layer theory (Lilly 1968). The mixed layer theory assumes zero storage and zero fluxes above the inversion layer. The relaxed form of the inversion-layer budget equations for the liquid water static energy, s_l, and total water mixing ratio, r, is written as

$$\begin{cases} E\Delta s_l - \Delta F_{s_l} - \Delta R = \varepsilon_{s_l} \\[2mm] E\Delta r - \Delta F_r = \dfrac{\varepsilon_r}{L} \end{cases} , \tag{C1}$$

where E is the entrainment rate, F is the flux, R is the radiative flux, ε is the storage. By defining the total storage as

$$\varepsilon^2 = \varepsilon_{s_l}^2 + \varepsilon_r^2, \tag{C2}$$

one can derive the entrainment rate with the minimum ε^2 as

$$E = \frac{\Delta s_l \left(\Delta F_{s_l} + \Delta R \right) + L^2 \Delta r \Delta F_r}{\left(\Delta s_l \right)^2 + \left(L\Delta r \right)^2}. \tag{C3}$$

The entrainment rate with the above formula with reasonable levels B and $B+$ is optimally consistent with the mixed layer theory.

YR08 developed a method to locate z_{B+} and z_B. The level $B+$ is the lowest level where both

$$\left|F_{s_l}\right| < 0.025 \max\left(\left|F_{s_l}\right|\right) \quad \text{and} \quad \left|F_r\right| < 0.025 \max\left(\left|F_r\right|\right) \tag{C4}$$

are satisfied from the domain top. The level B is the level at either first or second minimum of

$$\phi = \frac{\left|\varepsilon_{s_l}\right| + \left|\varepsilon_r\right|}{\left|E\Delta s_l\right| + \left|\Delta F_{s_l}\right| + \left|\Delta R\right| + \left|EL\Delta r\right| + \left|L\Delta F_r\right|}. \tag{C5}$$

from z_{B+}. This method is purely empirical, so that the diagnosed levels are sometimes located on unrealistic heights. This leads to a wrong entrainment rate.

We changed the method to locate z_{B+} and z_B, which uses the variance of the liquid water static energy. The new method locates z_{B+} and z_B at the height of

$$\begin{cases} z_{B+} = z \text{ at } 0.05 \max\left(\overline{s_l'^2}\right) \text{ above } z_{\max} \\ z_B = z \text{ at } 0.05 \max\left(\overline{s_l'^2}\right) \text{ below } z_{\max} \end{cases}, \tag{C6}$$

where

$$z_{\max} = z \text{ at } \max\left(\overline{s_l'^2}\right). \tag{C7}$$

The linear interpolation is used to assign both levels to a non-discrete height level. The entrainment rate is computed with (C3).

The new method is based on the profile of the third moment of the liquid water static energy. The third moment for GCSS DYCOMS-II at four hours is shown in Figure C1a with the diagnosed z_{B+} and z_B. The vertical profile of the third moment is negative in the upper inversion layer and positive in the lower inversion layer. The upper inversion

layer is negatively skewed because only small fractions of the air are as cool as the air in the mixed layer. The lower inversion layer is weakly positively skewed because most of the air is cool. This skewed profile was also confirmed with observational data (S. Krueger 2009, personal communication). Although the minimum and maximum third moments could be used in (C6), a very small positive maximum could prevent from locating z_B. The variance has only one positive peak in the inversion layer, and the third moment is near zero where the variance is near zero. The positive peak also tends to locate around the maximum vertical gradient of s_l and r. Thus, it is a good reference variable to identify z_{B+} and z_B with a reasonable threshold. The diagnosed z_{B+} and z_B are reasonably located in the profile of the liquid water static energy and total water mixing ratio. The diagnosed entrainment rate and the storage of the liquid water static energy shown in Figure C1b are comparable for both methods. The new method is, however, more physically based, less arbitrary, and simpler. This method can be used with other variables such as moist static energy or virtual dry static energy, which have the same property in their second and third moments.
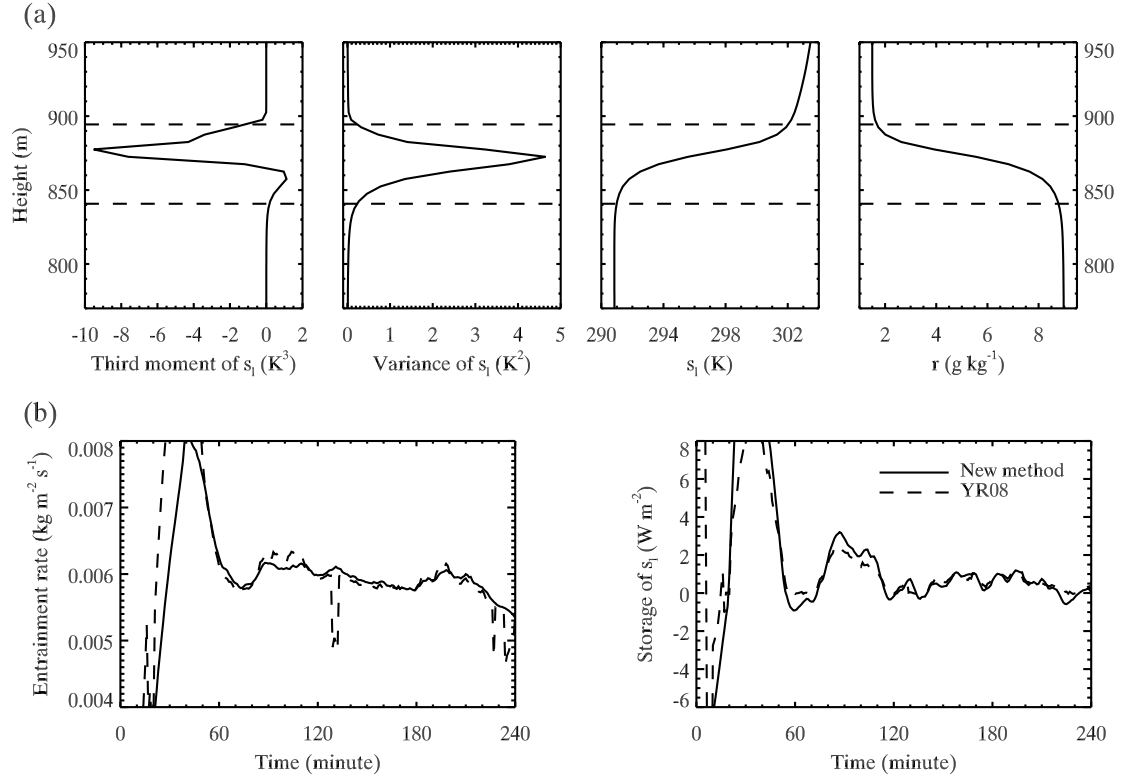
Figure C1   (a) Diagnosed levels *B+* and *B* (dashed lines) with the vertical profile of the first to third
moment of the liquid water static energy, and total water mixing ratio. (b) Time series of
entrainment rate and storage of the liquid water static energy for YR08 and the new method.
The 30-minute running mean profiles were used to obtain smooth time series.

Appendix D. Lagrange Interpolation

The interpolation polynomial in the Lagrange form is a linear combination of

$$f(x) = \sum_{i=i_1}^{i_2} \left[f_i \left(\prod_{j=i_1, j\neq i}^{i_2} \frac{x - x_j}{x_i - x_j} \right) \right], \tag{D1}$$

where $(i_1, i_2) = (-2, 3)$ for the fifth-order interpolation, so that the interpolation point is always between 0 and 1. The order of the interpolation should be an odd order if the interpolated function is continuous between grid 0 and 1.

If the grid is uniform, the fifth-order interpolation becomes

$$\begin{aligned} f(x) = f_0 &+ \frac{3f_{-2} - 30f_{-1} - 20f_0 + 60f_1 - 15f_2 + 2f_3}{60} x \\ &+ \frac{-f_{-2} + 16f_{-1} - 30f_0 + 16f_1 - f_{-2}}{24} x^2 + \frac{-f_{-2} - f_{-1} + 10f_0 - 14f_1 + 7f_2 - f_3}{24} x^3 \\ &+ \frac{f_{-2} - 4f_{-1} + 6f_0 - 4f_{-1} + f_2}{24} x^4 + \frac{-f_{-2} + 5f_{-1} - 10f_0 + 10f_1 - 5f_2 + f_3}{120} x^5. \end{aligned} \tag{D2}$$

A fast and accurate algorithm for a non-uniform grid is available elsewhere.

Sequential application of the one-dimensional interpolation, such that the interpolated value for the current dimension is used as input for the next dimension, is equivalent to the three-dimensional interpolation. Expand $f(x, y, z)$ with three dimensional Taylor series:

$$f = f_0 + f_0^x \delta x + f_0^y \delta y + f_0^z \delta z + \frac{1}{2}\left(f_0^{xx}\delta x^2 + f_0^{yy}\delta y^2 + f_0^{zz}\delta z^2 + 2f_0^{xy}\delta x\delta y + \cdots \right) + \cdots, \tag{D3}$$

where

$$f_0 = f(x_0, y_0, z_0) \quad \delta x = x - x_0, \quad f_0^x = \left.\frac{\partial f}{\partial x}\right|_0 \quad \text{and} \quad f_0^{xx} = \left.\frac{\partial^2 f}{\partial x^2}\right|_0. \tag{D4}$$

The Taylor series expansion for the interpolated functions only for the x direction is written as

$$f_x(x, y_0, z_0) = f_0 + f_0^x \delta x + \frac{1}{2} f_0^{xx} \delta x^2 + \cdots. \tag{D5}$$

The sequential application gives $f_{xy}(x, y, z_0)$ by the y-direction interpolation with $f_x(x, y_j, z_0)$, where $j = [-2, -1, 0, 1, 2, 3]$. The Taylor series of $f_{xy}(x, y, z_0)$ is written as

$$f_{xy}(x, y, z_0) = f_x + f_x^y \delta y + \frac{1}{2} f_x^{yy} \delta y^2 + \cdots. \tag{D6}$$

Note that there are no derivatives in terms of the x direction since $\delta x = 0$. By substituting (D5) into (D6), one can easily show that the sequential application generates necessary cross terms such as $2 f_0^{xy} \delta x \delta y$. The sequential application reduces

$$f(x, y, z) = f_{xyz}(x, y, z). \tag{D7}$$

The three-dimensional second-order Lagrange interpolation is equivalent to the trilinear interpolation. For this case, f can be written as

$$f(x, y, z) = c_0 + c_1 \frac{x - x_0}{\Delta x} + c_2 \frac{y - y_0}{\Delta y} + c_3 \frac{z - z_0}{\Delta z} + c_4 \frac{x - x_0}{\Delta x} \frac{y - y_0}{\Delta y} + c_5 \frac{y - y_0}{\Delta y} \frac{z - z_0}{\Delta z}$$
$$+ c_6 \frac{z - z_0}{\Delta z} \frac{x - x_0}{\Delta x} + c_7 \frac{x - x_0}{\Delta x} \frac{y - y_0}{\Delta y} \frac{z - z_0}{\Delta z}, \tag{D8}$$

where Δx and Δy are horizontal grid sizes, and Δz is a vertical grid size. The coefficients are obtained with the eight closest grid values. Assign f of each grid point based on its location as

$$f_{000} = f(x_0, y_0, z_0), \quad f_{100} = f(x_1, y_0, z_0), \quad f_{010} = f(x_0, y_1, z_0),$$
$$f_{001} = f(x_0, y_0, z_1), \quad f_{110} = f(x_1, y_1, z_0), \quad f_{011} = f(x_0, y_1, z_1), \tag{D9}$$
$$f_{101} = f(x_1, y_0, z_1), \quad f_{111} = f(x_1, y_1, z_1),$$

where $x_1 = x_0 + \Delta x$, $y_1 = y_0 + \Delta y$, and $z_1 = z_0 + \Delta z$. From (D8) and (D9), one easily finds

$$c_0 = f_{000}, \quad c_1 = -f_{000} + f_{100}, \quad c_2 = -f_{000} + f_{010},$$
$$c_3 = -f_{000} + f_{001}, \quad c_4 = f_{000} - f_{100} + f_{010} - f_{110},$$
$$c_5 = f_{000} - f_{010} - f_{001} + f_{011}, \quad c_6 = f_{000} - f_{100} - f_{001} + f_{101}, \tag{D10}$$
$$c_7 = -f_{000} + f_{100} + f_{010} + f_{001} - f_{110} - f_{011} - f_{101} + f_{111}.$$

The interpolated value is always bounded between the minimun and maximum of fs of (D9). The spatial derivative of f can be computed by

$$\begin{cases} \dfrac{\partial f}{\partial x} = \dfrac{1}{\Delta x}\left(c_1 + c_4 \dfrac{y - y_0}{\Delta y} + c_6 \dfrac{z - z_0}{\Delta z} + c_7 \dfrac{y - y_0}{\Delta y}\dfrac{z - z_0}{\Delta z} \right) \\[3mm] \dfrac{\partial f}{\partial y} = \dfrac{1}{\Delta y}\left(c_2 + c_4 \dfrac{x - x_0}{\Delta x} + c_5 \dfrac{z - z_0}{\Delta z} + c_7 \dfrac{x - x_0}{\Delta x}\dfrac{z - z_0}{\Delta z} \right) \\[3mm] \dfrac{\partial f}{\partial z} = \dfrac{1}{\Delta z}\left(c_3 + c_5 \dfrac{y - y_0}{\Delta y} + c_6 \dfrac{x - x_0}{\Delta x} + c_7 \dfrac{x - x_0}{\Delta x}\dfrac{y - y_0}{\Delta y} \right) \end{cases} . \tag{D11}$$

Appendix E.   SGS Velocity Parameterization

Based on the Lagrangian stochastic model of Thomson (1987), W04 parameterized the SGS velocity with the assumption of the locally isotropic and Gaussian but weakly inhomogeneous turbulence. One should refer W04. The formula of W04's SGS velocity parameterization is written as

$$d\left(u_s\right)_i = -\frac{3C_0}{4}\frac{f_s\varepsilon}{e_s}\left(u_s\right)_i dt + \frac{1}{2}\frac{\left(u_s\right)_i}{e_s}\left(\frac{de_s}{dt}\right)dt + \frac{1}{3}\left(\frac{\partial e_s}{\partial x_i}\right)dt + \left(f_s C_0 \varepsilon\right)^{1/2} d\xi_i, \qquad \text{(E1)}$$

where e_s and ε are the SGS TKE and its dissipation rate, respectively; C_0 is an assumed universal constant which W04 suggested 3; f_s is discussed below; the last term on the r.h.s. is a random forcing term, and $d\xi$ is a Gaussian white noise with zero mean and variance of dt.

W04 parameterized f_s as the fraction of the ensemble-mean SGS TKE to the total ensemble-mean TKE, then replaced the ensemble mean with the horizontal mean;

$$f_s = \frac{\overline{e}_s}{\overline{e}_r + \overline{e}_s}, \qquad \text{(E2)}$$

where the overbar denotes the horizontal mean. The fraction is guaranteed to be less than or equal to 1. The use of the horizontal mean is a treatment to represent the ensemble mean. Since the parameter is horizontally constant, the fraction is the same for strongly turbulent air and very weakly turbulent air at the same level.

We modified (E2) to be a local parameter by

$$f_s = \frac{e_s}{e_r + e_s},$$ (E3)

where

$$e_r = \frac{1}{2}\left[\left(u_r\right)_i - \left(\bar{u}_r\right)_i\right]^2.$$ (E4)

This is the simplest form of the local f_s. One could use the limited area mean, so that

$$f_s = \frac{\tilde{e}_s}{\tilde{e}_r + \tilde{e}_s},$$ (E5)

where the tilda represents limited area average.

We express the finite difference form of (E1) as

$$\frac{\left(u_s\right)_i^{t+1} - \left(u_s\right)_i^t}{\Delta t} = -\frac{3C_0}{4}\left(\frac{f_s \varepsilon}{e_s}\right)^t \left(u_s\right)_i^{t+1} + \left(\frac{e_s^{t+1} - e_s^t}{\Delta t}\right)\frac{\left(u_s\right)_i^t}{2e_s^t} + \frac{1}{3}\left(\frac{\partial e_s}{\partial x_i}\right)^t$$
$$+ \left[\left(C_0 f_s \varepsilon\right)^{1/2}\right]^t \frac{d\xi_i}{\Delta t}.$$ (E6)

The backward implicit scheme is used for the first term, which represents dissipation, for stability. The forward scheme is used for the other terms. The compact form of (E6) is

$$\left(u_s\right)_i^{t+1} = \left[\frac{1}{1 + \frac{3C_0}{4}\left(\frac{f_s \varepsilon}{e_s}\right)^t \Delta t}\right]\left[\frac{1}{2}\left(\frac{e_s^{t+1}}{e_s^t} + 1\right)\left(u_s\right)_i^t + \frac{1}{3}\left(\frac{\partial e_s}{\partial x_i}\right)^t \Delta t + \left[\left(C_0 f_s \varepsilon\right)^{1/2}\right]^t d\xi_i\right].$$ (E7)

It should be noted that the SGS velocity has to be computed for the parcel, not for the grid point, since the second term on the r.h.s. of (E6) involves the Lagrangian time derivative of the SGS TKE. The SGS velocity calculation is activated if e_s^t for the closest

109

eight points is larger than 10^{-2} m^2 s^{-2} in order to avoid dividing by near zero e_s^t, and to

avoid possible instability caused at $\dfrac{e_s^{t+1}}{e_s^t}$ for large e_s^{t+1} and small e_s^t. This threshold is

equivalent to the velocity scale of 10 cm s^{-1}. If this criterion is not satisfied then the SGS

velocity is set to 0 m s^{-1}. The estimated position only with the resolved scale velocity is

used to obtain e_s^{t+1} with spatial interpolation. The coefficients, $\dfrac{f_s\varepsilon}{e_s}$ and $\left(C_0 f_s\varepsilon\right)^{1/2}$, are

computed on each grid point then diagnosed to the parcel position. The spatial derivative

form of the trilinear interpolation, (D11), is used to obtain the spatial derivatives of the

SGS TKE in the third term on the r.h.s. of (E6). The value of the Gaussian white noise,

$d\xi$, is limited within two standard deviations, which cover about 95% of the distribution.

The sensitivity test for the W04's non-local, and our local f_s was checked. We used

the turbulence of the DYCOMS-II simulation described in Chapter 3. LPTM ran for 600

steps for both non-local and local f_s. The PDFs of the SGS velocity computed for both

cases at 600 steps are presented in Figure E1. The local f_s case has slightly more

variability than the non-local case. The variability becomes larger with smaller SGS TKE

threshold (not shown). Both cases maintain their magnitude within $O(0.1$ m s$^{-1})$. In these

PDFs, only 0.46 % of total number of parcel, i.e., about 2100 parcels, have non-zero SGS

velocity, and they are mainly around the inversion and cloud top (Figure E2). Apart from

the inversion, most of the grid points do not satisfy the SGS TKE threshold, and this is

reasonable for DYCOMS-II simulated with the grid size used (see the vertical profile of

the SGS TKE in Figure 3.2).
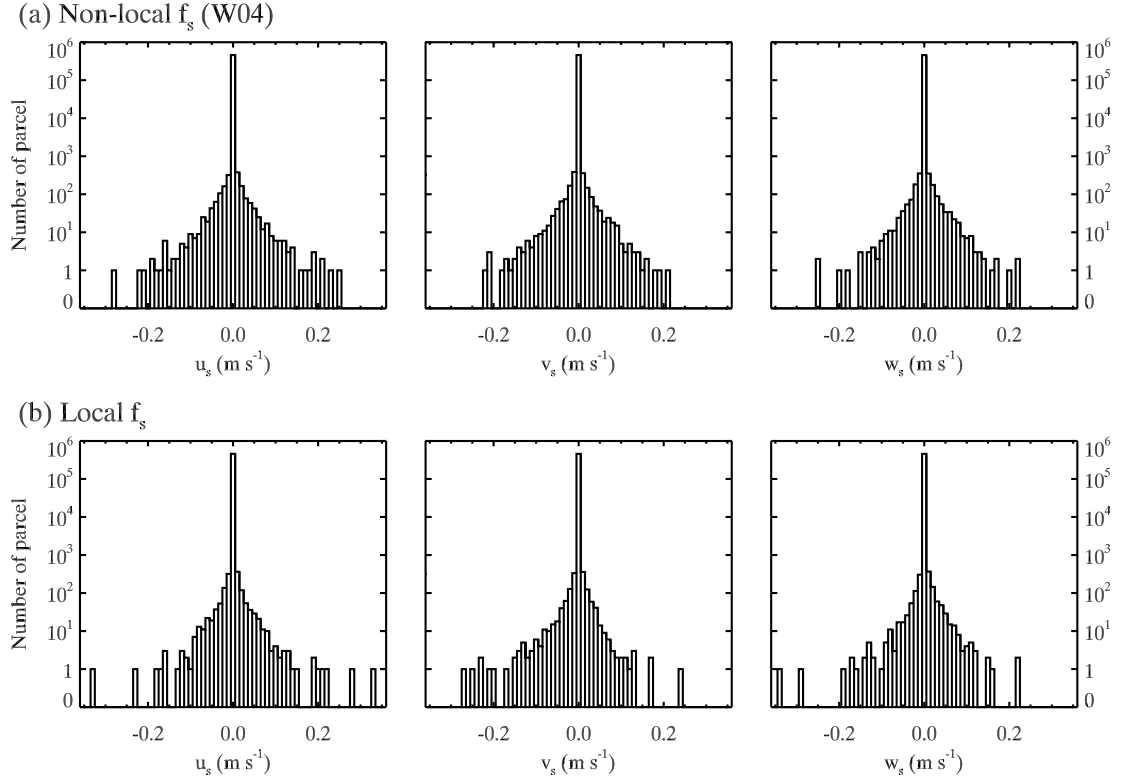
Figure E1   PDF of the SGS velocity parameterized with non-local and local f_s. The bin size is 0.01 m s^{-1}.
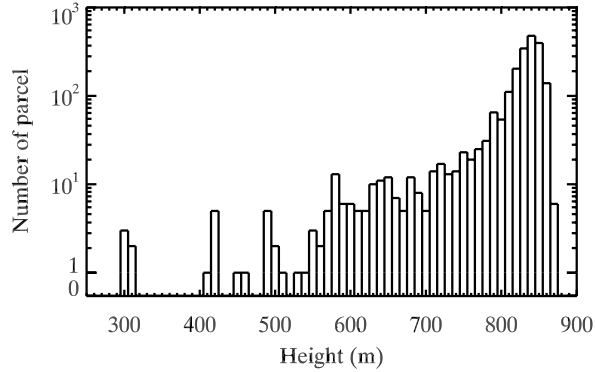

Figure E2   PDF of parcel height for parcels with non-zero SGS vertical velocity for local f_s case. The bin size is 10 m. The non-local f_s case showed the similar PDF.

References

Ackerman, A. S., and Coauthors, 2009: Large-eddy simulations of a drizzling, stratocumulus-topped marine boundary layer. *Mon. Wea. Rev.*, **137,** 1083-1110.

Albrecht, B. A., R. S. Penc, and W. H. Schubert, 1985: An observational study of cloud-topped mixed layers. *J. Atmos. Sci.*, **42,** 800-822.

Blossey, P. N., and D. R. Durran, 2008: Selective monotonicity preservation in scalar advection. *J. Comput. Phys.*, **227,** 5160-5183.

Bretherton, C. S., and Coauthors, 1999: An intercomparison of radiatively driven entrainment and turbulence in a smoke cloud, as simulated by different numerical models. *Quart. J. Roy. Meteor. Soc.*, **125,** 391-423.

Bryan, G. H., J. C. Wyngaard, and J. M. Fritsch, 2003: Resolution requirements for the simulation of deep moist convection. *Mon. Wea. Rev.*, **131,** 2394-2416.

Caldwell, P., and C. S. Bretherton, 2009: Large eddy simulation of the diurnal cycle in southeast Pacific stratocumulus. *J. Atmos. Sci.*, **66,** 432-449.

Cheng, A., and K.-M. Xu, 2009: A PDF-based microphysics parameterization for simulation of drizzling boundary layer clouds. *J. Atmos. Sci.*, **66,** 2317-2334.

Deardorff, J. W., 1980: Cloud top entrainment instability. *J. Atmos. Sci.*, **37,** 131-147.

Gerber, H., G. Frick, S. P. Malinowski, J. L. Brenguier, and F. Burnet, 2005: Holes and entrainment in stratocumulus. *J. Atmos. Sci.*, **62,** 443-459.

Grabowski, W. W., 2007: Representation of turbulent mixing and buoyancy reversal in bulk cloud models. *J. Atmos. Sci.*, **64,** 3666-3680.

Heus, T., G. van Dijk, H. J. J. Jonker, and H. E. A. Van den Akker, 2008: Mixing in shallow cumulus clouds studied by Lagrangian particle tracking. *J. Atmos. Sci.*, **65,** 2581-2597.

Hill, A. A., G. Feingold, and H. Jiang, 2009: The influence of entrainment and mixing assumption on aerosol-cloud interactions in marine stratocumulus. *J. Atmos. Sci.*, **66,** 1450-1464.

Khairoutdinov, M. F., and D. A. Randall, 2003: Cloud resolving modeling of the ARM summer 1997 IOP: Model formulation, results, uncertainties, and sensitivities. *J. Atmos. Sci.*, **60,** 607-625.

Krueger, S. K., G. T. McLean, and Q. Fu, 1995: Numerical simulation of the stratus-to-cumulus transition in the subtropical marine boundary layer. Part II: Boundary-layer circulation. *J. Atmos. Sci.*, **52,** 2851-2868.

Kuo, H.-C., and W. H. Schubert, 1988: Stability of cloud-topped boundary layers. *Quart. J. Roy. Meteor. Soc.*, **114,** 887-916.

Leonard, B. P., 1991: The ULTIMATE conservative difference scheme applied to unsteady one-dimensional advection. *Comput. Methods Appl. Mech. Eng.*, **88,** 17-74.

Leonard, B. P., A. P. Lock, and M. K. MacVean, 1995: The NIRVANA scheme applied to one-dimensional advection. *Int. J. Numer. Methods Heat Fluid Flow*, **5,** 341-377.

——, 1996: Conservative explicit unrestricted-time-step multidimensional constancy-preserving advection schemes. *Mon. Wea. Rev.*, **124,** 2588-2606.

Leonard, B. P., M. K. MacVean, and A. P. Lock, 1993: Positivity-preserving numerical schemes for multidimensional advection, NASA TM 106055, ICOMP-93-05, Lewis Research Center, Cleveland, OH**,** 62 pp.

Lilly, D. K., 1968: Models of cloud-topped mixed layers under a strong inversion. *Quart. J. Roy. Meteor. Soc.*, **94,** 292-309.

Lin, C., and A. Arakawa, 1997: The Macroscopic Entrainment Processes of Simulated Cumulus Ensemble. Part I: Entrainment Sources. *J. Atmos. Sci.*, **54,** 1027-1043.

Lock, A. P., 2009: Factors influencing cloud area at the capping inversion for shallow cumulus clouds. *Quart. J. Roy. Meteor. Soc.*, **135,** 941-952.

Mlawer, E. J., S. J. Taubman, P. D. Brown, M. J. Iacono, and S. A. Clough, 1997: Radiative transfer for inhomogeneous atmospheres: RRTM, a validated correlated-k model for the longwave. *J. Geophys. Res.*, **102(D14),** 16663-16682.

Moeng, C.-H., 2000: Entrainment rate, cloud fraction, and liquid water path of PBL stratocumulus clouds. *J. Atmos. Sci.*, **57,** 3627-3643.

Moeng, C.-H., M. A. LeMone, M. F. Khairoutdinov, S. K. Krueger, P. A. Bogenschutz, and D. A. Randall, 2009: The tropical marine boundary layer under a deep convection system: a large-eddy simulation study. *J. Adv. Model. Earth Syst.*, **1,** 13 pp.

Moeng, C.-H., D. H. Lenschow, and D. A. Randall, 1995: Numerical investigations of the roles of radiative and evaporative feedbacks in stratocumulus entrainment and breakup. *J. Atmos. Sci.*, **52,** 2869-2883.

Moeng, C. H., and Coauthors, 1996: Simulation of a stratocumulus-topped planetary boundary layer: Intercomparison among different numerical codes. *Bull. Amer. Meteor. Soc.*, **77,** 261-278.

Monin, A. S., and A. M. Obukhov, 1954: Basic laws of turbulent mixing in the atmosphere near the ground. *Tr. Geofiz. Inst., Akad. Nauk SSSR*, **24,** 163-187.

Randall, D. A., 1976: The interaction of the planetary boundary layer with large-scale circulations. Ph.D Dissertation, UCLA, 247 pp.

Randall, D. A., 1980: Conditional instability of the first kind upside-down. *J. Atmos. Sci.*, **37,** 125-130.

Savic-Jovcic, V., and B. Stevens, 2008: The structure and mesoscale organization of precipitating stratocumulus. *J. Atmos. Sci.*, **65,** 1587-1605.

Schubert, W. H., J. S. Wakefield, E. J. Steiner, and S. K. Cox, 1979: Marine stratocumulus convection. Part I: Governing equations and horizontally homogeneous solutions. *J. Atmos. Sci.*, **36,** 1286-1307.

Shao, Q., D. A. Randall, C. H. Moeng, and R. E. Dickinson, 1997: A method to determine the amounts of cloud-top radiative and evaporative cooling in a stratocumulus-topped boundary layer. *Quart. J. Roy. Meteor. Soc.*, **123,** 2187-2213.

Siebesma, A. P., and Coauthors, 2003: A large eddy simulation intercomparison study of shallow cumulus convection. *J. Atmos. Sci.*, **60,** 1201-1219.

Siems, S. T., and C. S. Bretherton, 1992: A numerical investigation of cloud-top entrainment instability and related experiments. *Quart. J. Roy. Meteor. Soc.*, **118,** 787-818.

Siems, S. T., C. S. Bretherton, M. B. Baker, S. Shy, and R. E. Breidenthal, 1990: Buoyancy reversal and cloud-top entrainment instability. *Quart. J. Roy. Meteor. Soc.*, **116,** 705-739.

Smolarkiewicz, P. K., and W. W. Grabowski, 1990: The multidimensional positive definite advection transport algorithm: Nonoscillatory option. *J. Comput. Phys.*, **86,** 355-375.

Stevens, B., and Coauthors, 2005: Evaluation of large-eddy simulations via observations of nocturnal marine stratocumulus. *Mon. Wea. Rev.*, **133,** 1443-1462.

Thomson, D. J., 1987: Criteria for the selection of stochastic models of particle trajectories in turbulence flows. *J. Fluid Mech.*, **180,** 529-556.

Thuburn, J., 1996: Multidimensional flux-limited advection schemes. *J. Comput. Phys.*, **123,** 74-83.

vanZanten, M. C., and P. G. Duynkerke, 2002: Radiative and evaporative cooling in the entrainment zone of stratocumulus – the role of longwave radiative cooling above cloud top. *Bound.-Layer Meteor.*, **102,** 253-280.

Weil, J. C., P. P. Sullivan, and C.-H. Moeng, 2004: The use of large-eddy simulations in Lagrangian particle dispersion models. *J. Atmos. Sci.*, **61,** 2877-2887.

Xu, K.-M., and D. A. Randall, 1995: Impact of Interactive Radiative Transfer on the Macroscopic Behavior of Cumulus Ensembles. Part I: Radiation Parameterization and Sensitivity Tests. *J. Atmos. Sci.*, **52,** 785-799.

Yamaguchi, T., and D. A. Randall, 2008: Large-eddy simulation of evaporatively driven entrainment in cloud-topped mixed layers. *J. Atmos. Sci.*, **65,** 1481-1504.

Zalesak, S. T., 1979: Fully multidimensional flux-corrected transport algorithms for fluids. *J. Comput. Phys.*, **31,** 335-362.